Lattice Boltzmann Simulations of Environmental Flow Problems in Shallow Water Flows

Thesis submitted in accordance with the requirements of the
University of Liverpool for the degree of Doctor in Philosophy

by

Yong Peng (BEng, MSc)

7th November 2012

Abstract

The lattice Boltzmann method (LBM) proposed about decades ago has been developed and applied to simulate various complex fluids. It has become an alternative powerful method for computational fluid dynamics (CFD). Although most research on the LBM focuses on the Navier-Stokes equations, the method has also been developed to solve other flow equations such as the shallow water equations. In this thesis, the lattice Boltzmann models for the shallow water equations and solute transport equation have been improved and applied to different flows and environmental problems, including solute transport and morphological evolution. In this work, both the single-relaxation-time and multiple-relaxation-time models are used for shallow water equations (named LABSWE and LABSWE^{MRT}, respectively), and the large eddy simulation is incorporated into the LABSWE (named LABSWE^{TM}) for turbulent flow.

The capability of the LABSWE^{TM} was firstly tested by applying it to simulate free surface flows in rectangular basins with different length -width ratios, in which the characteristics of the asymmetrical flows were studied in details. The LABSWE^{MRT} was then used to simulate the one- and two-dimensional shallow water flows over discontinuous beds. The weighted centred scheme for force term, together with the bed height for a bed slope, was incorporated into the model to improve the simulation of water flows over a discontinuous bed. The resistance stress was also included to investigate the effect of the local head loss caused by flows over a step. Thirdly, the LABSWE^{MRT} was extended to simulate a moving body in shallow water. In order to deal with the moving boundaries, three different schemes with second-order accuracy were tested and compared for treating curved boundaries. An additional momentum term was added to reflect the interaction between the following fluid and the solid, and a refilled method was proposed to treat the wetted nodes moving out from the solid nodes. Fourthly, both LABSWE and LABSWE^{MRT} were used to investigate solute transport in shallow water. The flows are solved using LABSWE and LABSWE^{MRT}, and the advection-diffusion equation for solute transport was solved with a LBM-BGK model based on the D2Q5 lattice. Three cases: open channel flow with a side discharge, shallow recirculation flow and flow in a harbour, were simulated to verify the methods. In addition, the performance of LABSWE^{MRT} and LABSWE were compared, and the results showed that the LABSW^{MRT}

has better stability and can be used for flow with high Reynolds number. Finally, the lattice Boltzmann method was used with the Euler-WENO scheme to simulate morphological evolution in shallow water. The flow fields were solved by the LABSWE^{MRT} with the improved scheme for the force term, and the fifth order Euler-WENO scheme was used to solve the morphological equation to predict the morphological evolution caused by the bed-load transport.

Acknowledgement

First and foremost, I would like to express my gratitude to my supervisor, Dr Jian Guo Zhou for his guidance, support and encouragement throughout my study at the University of Liverpool. Numerous meetings with him are the origins of the research ideas and the directions of the way going forward. His attitude for the research will lead me further in my future career. Without him, this thesis would not be possible. I also would like to thank my second supervisor, Professor Richard Burrows, for his invaluable comments on the papers and this thesis.

I also appreciate my previous supervisor, Professor Jian Min Zhang at Sichuan University in China during my study for the Master of Engineering from 2005 to 2008. His knowledge and virtue are always worthy of my respect.

I appreciate the University of Liverpool very much for providing me the financial support through the Overseas Research Students Awards Scheme (ORSAS, UK) and Teaching Assistant Position. Furthemore, I also appreciate China Scholarship Council (CSC, P. R. China) for the financial support.

In addition, I am grateful to Mr. Hu Xiao Yu , Li Shuai, Cui Rui, and Bai Rui Di who carried out the experiments in chapter 6 at Sichuan university.

I am also grateful to all my colleagues and the staff of the Department of Engineering for their generous help and support and my special thanks goes to associate professor Haifei Liu in the school of Environment at Beijing Normal University for his help in life and work.

Last but not least, I would like to express the gratitude from my heart to my parents, my old sister and her husband, who have been giving me the unconditional love in my life.

Publications

1. Y. Peng, J.G. Zhou and R. Burrows (2011). Modelling the free surface flow in rectangular shallow basins by lattice Boltzmann method. *Journal of Hydraulic Engineering ASCE*, vol. 137, issue 12, pp: 1680-1685.

2. Y. Peng, J.G. Zhou and R. Burrows (2011). Modelling solute transport in shallow water with the lattice Boltzmann method. *Computers and Fluids*, vol. 50, issue 1, pp: 181-188.

3. Y. Peng, J.G. Zhou, J.M. Zhang, and R. Burrows. Modeling moving boundary in shallow water by LBM. *International Journal of Morden Physics C*. (Accepted).

4. Y. Peng, J.G. Zhou and J.M. Zhang. Mixed numerical method for bed evolution. *Proceedings of the ICE - Water Management*. (Under review).

5. Y. Peng, J.G. Zhou, J.M. Zhang, H. Liu. Lattice Boltzmann Modelling of Shallow Water Flows over Discontinuous Beds. *International Journal for Numerical Methods in Fluids*. (Under review).

6. J.G. Zhou, H. Liu, S. Shafiai, Y. Peng, R. Burrows (2010). Lattice Boltzmann Method for Open Channel Flows. *Proceedings of ICE: Engineering and Computational Mechanics*, vol.163, issue 4, pp: 243-249.

7. H. Liu, J.G. Zhou, R. Burrows and Y. Peng (2009). A Lattice Boltzmann Model for Dam Break Flows. *Proceedings of World Environmental and Water Resources Congress. ASCE*, Missouri, pp: 3351-3359.

Contents

Abstract I

Acknowledgement III

Publications IV

List of Figures IX

List of Tables XIII

List of Abbreviations and Symbols XIV

Chapter 1: Introduction 1

1.1 Research Background 1

1.2 Traditional Method for Shallow Water Equations 1

1.3 Lattice Boltzmann Method for Shallow Water Flows 3

1.4 Lattice Gas Automata 4

1.5 Lattice Boltzmann Method 5

1.5.1 Lattice Boltzmann Equation 5

1.5.2 Entropic Lattice Boltzmann Method 6

1.5.3 Two-Relaxation-Time lattice Boltzmann Method 7

1.5.4 Multiple-Relaxation-Time Lattice Boltzmann Method 7

1.5.5 Grid Refinement 8

1.5.6 Parallel Computation 9

1.5.7 Moving Boundary 10

1.6 Objectives 10

1.7 Outline of the Thesis 12

Chapter 2: Governing Equations for Shallow Water Flows 14

2.1 Introduction 14

2.2 The Navier-Stokes Equations 14

2.3 The Shallow Water Equations 16

2.4 The Advection-diffusion Equation 23

2.5 Numerical Methods for Turbulent Flow 23

2.6 Subgrid-Scale Stress Model 24

Chapter 3: Lattice Boltzmann Method 26

3.1 Introduction 26

3.2 Derivation of the Lattice Boltzmann Equation 26

3.3 Lattice Boltzmann Equation........27
3.4 Lattice Pattern........29
3.5 Local Equilibrium Distribution Function........30
3.6 Macroscopic Properties........33
3.7 Recovery of the Shallow Water Equations........34
3.8 Stability Conditions........36
3.9 Force Terms........37
  3.9.1 Centred Scheme........37
  3.9.2 Improved Force Term treatment method and New Treatment of Bed Slope....39
  3.9.3 Discussion........40
3.10 Turbulence Modelling........40
  3.10.1 LABSWE^{TM}........40
  3.10.2 Recovery of LABSWE^{TM}........42
3.11 Multiple-Relaxation Time........44
  3.11.1 LABSWE^{MRT}........44
  3.11.2 Recovery of the LABSWE^{MRT}........45
3.12 Solute Transport Equation........48
  3.12.1 Lattice Boltzmann Model for Solute Transport Equation........48
  3.12.2 Recovery of the Advection-diffusion Equation........49
Chapter 4: Initial and Boundary Conditions........52
4.1 Introduction........52
4.2 Solid Boundary Condition........52
  4.2.1 No-slip Boundary Condition........52
  4.2.2 Slip Boundary Condition........53
  4.2.3 Semi-slip Boundary Condition........53
4.3 Inflow and Outflow Condition........54
4.4 Periodic Boundary Condition........56
4.5 Initial Condition........56
4.6 Solution Procedure........57
Chapter 5: Applications of LABSWE^{TM} and LABSWE^{MRT} for the Free Surface Flows..58
5.1 The Flows in Rectangular Shallow Basins........58
  5.1.1 Introduction........58
  5.1.2 Background........58

5.1.3 Boundary Conditions 59
5.1.4 Numerical Simulation 59
5.1.5 Comparisons of Results 62
5.1.6 Sensitivity Analysis 64
5.1.7 Conclusions 67
5.2 Shallow Water Flows over Discontinuous Beds 68
5.2.1 Introduction 68
5.2.2 Background 68
5.2.3 Numerical Case Studies 69
5.2.4 Conclusions 75
Chapter 6: Application of LABSWE^{MRT} for Simulating the Moving Body 76
6.1 Introduction 76
6.2 Background 76
6.3 Boundary Conditions 77
6.4 Simulation for Stationary Cylinder 80
6.5 Numerical Simulation for a Moving Cylinder 85
6.6 Conclusions 89
Chapter 7 Application of LABSWE and LABSWE^{MRT} to Environmental Flows 90
7.1 Introduction 90
7.2 Background 90
7.3 Boundary Conditions 90
7.4 Numerical Case Studies 90
Case 1: Side Discharge 90
Case 2: Flow in a Harbour 96
Case 3: Shallow Recirculation Flow 98
7.5 Conclusions 100
Chapter 8: Coupling LABSWE^{MRT} and Euler-WENO Scheme for Morphological Evolution 102
8.1 Introduction 102
8.2 Background 102
8.3 Governing Equations 103
8.4 Solution of the Morphological Evolution Equation 103
8.5 Boundary Conditions 106

8.6 Numerical Results 106
Test 1: Change of 1D Gaussian Dune 107
Test 2: Bed Change of a 1D Trapezoidal Dune 107
Test 3: Morphological Evolution of 2D Sand Dune 110
8.7 Conclusions 113
Chapter 9: Conclusions and Recommendations 114
9.1 Preamble 114
9.2 Conclusions 114
9.2.1 Multiple-Relaxation-Time Lattice Boltzmann Method with Improved Force 114
9.2.2 Modelling the Flow over Discontinuous Beds Using LABSWE^{MRT} 115
9.2.3 Moving Boundary in Shallow Water Flows 115
9.2.4 Solute Transport in Shallow Water Flows 115
9.2.5 Mixed Numerical Method for Bed Evolution 115
9.2.6 Numerical simulation for free surface flows in rectangular shallow basins 116
9.3 Recommendations 116
9.3.1 Simulating the Moving Body with Variable Velocity 116
9.3.2 Incorporation of the Suspended Sediment Transport 116
9.3.3 Supercritical Flow Simulation 117
9.3.4 Parallel Computation for LBM 117
References 118

List of Figures

2.1 Cartesian coordinate system …………………………………………….……….……… 15

2.2 Shallow water flow sketch ………………………………………….…..…………17

3.1 9-speed square lattice (D2Q9) in the horizontal plane……………………………….29

3.2 7-speed square lattice (D2Q7) in the horizontal plane……………………………….29

3.3 5-speed square (D2Q5) lattice in horizontal plane…………………….…………..49

4.1 Layout of wall boundary and lattice nodes…………………………….……….……53

4.2 Inlet and outlet boundary conditions…………………………………………..…..55

5.1 Sketch of the channel…………………………………………..…………….61

5.2 Experimental (left) and simulated (right) flow vectors in the basin of 4m wide and 4m long…………………………………………….…………………………………61

5.3 Experimental (left) and simulated (right) flow vectors in the basin of 4m wide and 6 m long……………………………………….………………………………61

5.4 Bifurcation for different aspect ratio (L/B) and expansion ratio (B/b) ………………61

5.5 Relative error of Lr against grid size Δx……………………………………………..62

5.6 Comparisons of intensities asymmetry………………………………………………63

5.7 Comparisons of streamwise velocities at x =1.5m, 2m, 3m, and 4.5 m……………...63

5.8 Asymmetrical moment distribution with different Froude numbers…………………64

5.9 Reattachment length for different Froude numbers…………………………………64

5.10 Normalized streamwise velocity u/u_{max} profiles at x=2 m…………………………65

5.11 Asymmetrical moment distribution for different parameter S_t (S_t = $C_b b/(2h)$)...…..66

5.12 Reattachment length for different parameter *S*……………………………………...66

5.13 Velocity at *T*=10800s…………………………...…………………….……….70

5.14 Water depth at *T*=10800s………………………...……………………….………..70

5.15 Water velocity at *T*=8s……………………...…………………….……….......71

5.16 Water surface at *T*=8s……………………………………………….……………71

5.17 Comparison of water surface profiles with and without head loss for 1D case…….73

5.18 Bottom profile for 2D case (Side view) ……………………………………………73

5.19 Water surface for static flow……………………..…………………………..……..73

5.20 Discharge for static flow……………………..……………………………….…74

5.21 Discharge for 2D steady flow……………………………………………….……74

5.22 Predicted water surface by MRT-LBM……………………………………………..74

5.23 Comparison of centerline water surface profiles between 1D and 2D……………...75

6.1 Layout of curved boundary and lattice nodes………………………………………..78

6.2 Layout of the channel and equipment in the experiments……………………………81

6.3 Convergence of the three schemes…………………………………………………...83

6.4 Water depth along the centreline for Case 1………………..………………………..84

6.5 Water depth along the centreline for Case 2………………..………………………..84

6.6 Water depth along the centreline for Case 3……………………...…………………84

6.7 Velocity vector for case 1 with FH's scheme………………………………………...85

6.8 Water depths at *t*=12s for moving cylinder for Case 4………..……………………87

6.9 Water depths at *t*=2s for moving cylinder for Case 5…………..…………………...87

6.10 Water depths at different time for case 4 with FH's scheme (*t*=4s (a), 8s (b), and 12s (c)) ………………………………….……………………………………………88

6.11 Water depths at centerline with u_w= 0, 0.1 and 0.5 m/s with MMP's scheme at same position……………………………………..……………………………………..89

7.1 Predicted streamlines for M_1=0.105 by LABSWE$^{\mathrm{MRT}}$……………………………......92

7.2 Predicted velocity vectors for M_1=0.105 by LABSWE$^{\mathrm{MRT}}$……………………..…...93

7.3 Recirculation eddy length…………………………………………………….…………94

7.4 Recirculation eddy height…………………………………………………….…………94

7.5 Recirculation shape factor…………………………………………………….………...94

7.6 Jet centerline trajectory…………………………………………………….…………...95

7.7 Temperature dilution along the jet centreline………………………………………...95

7.8 Plan view of harbour layout……………………………………………….………....97

7.9 Streamlines in harbour by MRT-LBM………………………………………………….97

7.10 Velocity vectors in harbour by MRT-LBM……………………………………...97

7.11 Dimensionless average concentration C/C_0 against time in harbour……………….97

7.12 Dimensionless average concentration C/C_0 against time at x=0, y=0.35m (Centre point of harbour) ………………………………………….………………………...98

7.13 Plot of flow pattern and predicted streamlines for shallow recirculating flow (plan view) …………………………..……………………………………………………99

7.14 Concentration contours……………………………………..…….……………100

7.15 Comparisons of normalized concentration profiles at different cross sections (x = 0.5L, L, 1.5L, 2L)…………………………...…………...……….………………100

8.1 Comparisons of profiles of the dune evolution between analytical solutions and predictions……………………………………….…………………………...107

8.2 Layout of the experiments and the sand dune (Side view) on the channel floor…...108

8.3 Comparisons of profiles of the dune evolution between experiments and predictions. (*t*=0.5, 1.0, 1.5, 2.0 hours from top to bottom) ……………………………………………109

8.4 The initial bed configuration (a), steady velocity components *u* (b) and *v* (c), and water surface for flow over fixed bed (d) ………………………………………………111

8.5 Snapshots of the bed evolution of 2D sand dune at *t* = 25 (a), 50 (b), 75 (c), and 100 hours (d) ……………………………………..……………………………………….112

List of Tables

Table 6.1 Hydraulic parameters in the experiments……………….…………………..81

Table 6.2 The relative error E_r for three schemes……………………………………..82

Table 7.1 Channel and flow parameters for side discharge flow...………………………92

List of Abbreviations and Symbols

Abbreviations

1D	One dimensional
2D	Two dimensional
3D	Three dimensional
BGK	Bhatnagar-Gross-Krook model
BGK-LBM	Lattice Boltzmann method using BGK scheme
CFD	Computational fluid dynamics
D2Q5	5-speed square lattice
D2Q7	7-speed square lattice
D2Q9	9-speed square lattice
DNS	Direct numerical simulation
ELBM	Entropic lattice Boltzmann method
ENO	Essentially Non-Oscillatory
Euler-WENO	A mixed method with Euler and WENO schemes
FDM	Finite difference methods
FEM	Finite element methods
FH	Method proposed by Filippova and Hanel
FHP model	Model designed by Frisch, Hasslacher and Pomeau
FVM	Finite volume methods
Guo	Method proposed by Guo Zhao Li
HPP model	Model designed by Hardy, de Pazzis and Pomeau
LABSWE	The lattice Boltzmann model for shallow water equations
LABSWE^{TM}	The lattice Boltzmann model for shallow water equations with turbulence

	modelling
$\text{LABSWE}^{\text{MRT}}$	The lattice Boltzmann model for shallow water equations with multiple-relaxation-time
LBM	Lattice Boltzmann method
LES	Large-eddy simulation
LGA	Lattice gas automaton
LGCA	Lattice gas cellular automata
MRT-LBM	Lattice Boltzmann method with multiple-relaxation-time
MMP	Method proposed by Bouzidi, M., M. Firdaouss, and P. Lallemand
N-S	Navier-Stokes
NOCS	Non-oscillating centred scheme
RANS	Reynolds-averaged Navier–Stokes
SGS	Subgrid-Scale Stress
SIMPLE	Semi-Implicit Method for Pressure-Linked Equations
SMM	Lagrangian second-moment method
SRT-LBM	Lattice Boltzmann method with single-relaxation-time
TRT-LBM	Lattice Boltzmann method with two-relaxation-time
WENO	Weighted Essentially Non-Oscillatory scheme

Symbols

b	Inlet channel width	m
b_1	Outlet channel width	m
B	Width of the channel	m
c_x, c_y	Empirical factor for the local head loss in x and y	

	directions respectively	
C	Depth-averaged concentration	
C_b	Bed friction coefficient	
C_f	Friction factor at the wall	
C_0	Integration constant	
C_s	Smagorinsky constant	
C_w	Resistance coefficient of the water-air interface	
C_{wall}	Side wall friction coefficient	
c_x	Bed-form propagation phase speeds in the *x* direction	
C_z	Chezy coefficient	
d_{50}	Median diameter of the sediment particles	m
D	Spatial dimension	
D_i	Dispersion coefficient in direction *i*	
DT	Maximum excess temperature over river temperature	℃
DT_0	Discharge excess temperature	℃
e	Particle velocity	m/s
e_α	Velocity vector of a particle in the α link in LBM for shallow water equations	m/s
e_x, e_y	Particle velocity in the *x* and *y* directions respectively	m/s
e_{ai}	Particle velocity of direction *i* in link *a*	m/s
$e_{1\alpha}$	Velocity vector of a particle in link α in LBM for the advection-diffusion equation	m/s
e_{-n}	Particle velocity in in-normal direction	m/s
$E1$	Relative error parameter	

E_i	Coriolis term	
E_r	Relative error	
f_α	Distribution function of particle in α direction	*m*
$f_{\bar{\alpha}}$	Distribution function in opposite direction of α in MMP's scheme	*m*
f^{eq}	Maxwell-Boltzmann equilibrium distribution function	*m*
f_α^{eq}	Local equilibrium distribution function in α direction	*m*
$f_\alpha^{(*)}$	Fictitious equilibrium distribution function in α direction in FH's scheme	*m*
$\tilde{f}_\alpha$	Distribution function in α direction in FH's scheme	*m*
f_c	Coriolis parameter	
f_i	Body force per unit mass acting on fluid in *i* direction	*N*
f_i^{eq}	Local equilibrium distribution function	*m*
f_x, f_y, and f_z	Body forces per unit mass in the corresponding direction	*N/kg*
F_i	Component of the force in *i* direction	*N*
Fr	Froude number	
g	Acceleration owing to gravity	m/s^2
g_α	Distribution function of particles in LBM for the advection-diffusion equation	
g_α^{eq}	Local equilibrium distribution function in LBM for the advection-diffusion equation	
G	A spatial filter function	
h	Water depth	*m*

$\bar{h}$	Average water depth	m
h_0	Water depth at the outlet channel	m
h_b	Water depth at node b	m
h_{ex}	Experimental water depth	m
h_f	Water depth at node f	m
h_{f_1}	Water depth at node f_1	m
h_{f_2}	Water depth at node f_2	m
h_{ff}	Water depth at node ff	m
h_{pr}	Calculated water depth by LBM	m
i , j	Subscripts are space direction indices	
K	Number of directions of the particle velocities at each node	
K_s	Nikuradse equivalent sand roughness	
l_s	Characteristic length scale	
L	Length of the channel	m
Lr	Relative error	
m	Moments	
m^{eq}	Equilibrium values of moments	
M	Asymmetric moment	
M_1	Momentum flux ratio	
n	Out-normal direction	
n_α	Boolean variable	
n_b	Manning coefficient for bed roughness	

n_f	Manning’s coefficient	
N	Global moment	
N_α	A constant determined by the lattice pattern	
N_x	Number of lattice used in x direction	
p	Pressure	Pa
p_a	Atmospheric pressure	Pa
po	Bed porosity	
q	Unit discharge at inlet	m^2/s
q_{bj}	Bed-load transport rate in j direction	
Q_0	Specified discharge	m^3/s
Q_{in}	Calculated discharge	m^3/s
R	Ideal gas constant	℃
Re	Reynolds number	
s	Specific gravity of the particle	
s_0- s_8	Relaxation parameter in different direction	
$\boldsymbol{S}$	Relaxation matrix	
S_c	Depth-averaged source term	
S_{ij}	Magnitude of the large scale strain-rate tensor	
S_t	A parameter chosen to quantify the stabilizing effect of the bed-friction	
t	Time	s
T	Time	s
T_c	Temperature	℃
$\boldsymbol{T_r}$	Transform matrix	

u, v, and w	Velocity components in *i*, *j*, *k* direction respectively	*m*/*s*
u	Flow velocity in *x* direction	*m*/*s*
$\bar{u}$	Depth-average velocity in shallow water flow	*m*/*s*
u_{1wi}	Component of the wind velocity in *i* direction	*m*/*s*
u_α	Velocity component in α direction	*m*/*s*
u_b	Flow velocity at node *b* in *x* direction	*m*/*s*
u_{bi}	Flow velocity at node *b* in *i* direction	*m*/*s*
u_f	Flow velocity at node *f* in *x* direction	*m*/*s*
u_{ff}	Flow velocity at node *ff* in *x* direction	*m*/*s*
u_{fi}	Flow velocity at node *f* in *i* direction	*m*/*s*
u_i	Velocity component in *i* direction	*m*/*s*
$\tilde{u}_i$	Depth-averaged space-filtered velocity component	*m*/*s*
u_{max}	Maximum velocity	*m*/*s*
u_w	Velocity of moving body	*m*/*s*
u_{wi}	Velocity of moving body in *i* direction	*m*/*s*
u_{wx}	Velocity of moving body in *x* direction	*m*/*s*
u_{wy}	Velocity of moving body in *y* direction	*m*/*s*
U	Velocity in the main channel	*m*/*s*
U_s	Sound speed	*m*/*s*
v	Flow velocity in *y* direction	*m*/*s*
v_b	Flow velocity at node *b* in *y* direction	*m*/*s*
v_f	Flow velocity at node *f* in *y* direction	*m*/*s*

v_{ff}	Flow velocity at node *ff* in *y* direction	*m/s*
$\boldsymbol{V}$	Fluid velocity	*m/s*
w_α	Weighting factor in α direction in distribution function	
w_b , w_s	Vertical velocities at channel bed and the free surface respectively	*m/s*
w_i	Weighting coefficient	
x, y, z	Cartesian coordinate	*m*
x_i	Stands for either *x* or *y* in direction *i* or *j*	
z_b	Bed elevation above datum	*m*
α	Represent 9 different directions	
$\beta,\ \mu$	Lagrange multipliers	
λ	Relaxation time parameter	
$\delta_{\alpha\beta}$	Kronecker delta function,	
ϕ	Earth's latitude at the site	*Degre*e
θ	Shields parameter	
$\theta_1, \theta_2\ \theta_3$	Momentum correction factors	
θ_{cr}	Critical Shields parameter	
∇	Gradient operator	
$\langle n_\alpha \rangle$	Ensemble average of n_α	
$\mathit{\Omega}_\alpha$	Collision operator	
$\mathit{\Delta}$	Fraction between fluid part and solid part	
ΔE	Relative error	
ΔE_r	A predefined tolerance	

Δt	Time step	s
Δx	Lattice size	m
ρ	Fluid density	kg/m^3
ρ_a	Density of air	kg/m^3
ρ_s	Sediment density	kg/m^3
τ	Single dimensionless relaxation time in LBM for shallow water equations	
τ_1	Single relaxation time in LBM for the advection-diffusion equation	
τ_b	Bed shear stress	N/m^2
τ_{bi}	Bed shear stress in *i* direction	N/m^2
τ_e	Eddy relaxation time	
τ_{fi}	Wall shear stress	N/m^2
τ_{ij}	Depth-averaged subgrid-scale stress	N/m^2
τ_{sx} , τ_{sy}	Resistance stresses	N/m^2
τ_t	Total relaxation time	
ν	Kinematic viscosity	m^2/s
ν_e	Eddy viscosity	m^2/s
ν_t	Total viscosity	m^2/s
ω	Earth's rotation	Rad/s
ω_n	Weighting factor in out-normal direction in distribution function	
$\omega_{x1}, \omega_{x2}, \omega_{x3}, \widetilde{\omega}_{x1}, \widetilde{\omega}_{x2}, \widetilde{\omega}_{x3}$	Weights	
χ	Weighting factor in FH's scheme	

Chapter 1: Introduction

1.1 Research Background

The shallow water equations have been applied widely in ocean, rivers and coasts [1-5]. For example, it can be used to describe the tidal flows, tsunami, hydraulic jump, and open channel flows. Furthermore, coupled with the solute transport equation, the shallow water equations can be used to predict the solute transport such as distribution of pollution concentration and transport of suspended sediments [6-11]. Prediction of the flows and related transport is important in environmental engineering.

Moreover, another important application of the shallow water equations is to study the bed-load sediment transport, which plays a key role in the morphological evolution occurring in coastal areas, rivers, and estuaries, where the water flow is dominated horizontally and can be described by the shallow water equations [12-15]. Studies on morphological changes have attracted increasing interest in the fields of water resource exploitation and environment protection [16-18] .

1.2 Traditional Method for Shallow Water Equations

Many different numerical methods have been developed and applied to solve shallow water equations in the past years. They include the finite difference methods (FDM), finite element methods (FEM) and finite volume methods (FVM). Each method has its own features. For example, as indicated by Chen [19], compared with FEM, FDM has two advantages: the first one is that it is generally faster than the FEM for a similar case, which is more obvious for three-dimensional calculations [20]; the second one is that it generally does not suffer from the local mass conservation problem, which is often observed in a finite element model. On the other hand, The FEM adopts the unstructured grids which can fit complex and irregular geometries more easily than the FDM. Therefore, the FEM can reduce the number of grids significantly with the similar accuracy for flows in complicated geometries.

Casulli and Cheng [21] presented a semi-implicit finite difference method for two- and three-dimensional shallow water flows with hydrostatic pressure assumption. Casulli and Cattani [22] also studied the stability, accuracy and efficiency of a semi-implicit FDM method for the three-dimensional water flows. In recent years, the Weighted Essentially Non-Oscillatory scheme (WENO) has been used to solve the shallow water equations for solution with higher order accuracy by a finite difference method [22, 23]. For example, Lu and Li [23] studied a series of multilevel high order time discretization procedures for WENO scheme to solve the one-dimensional and two-dimensional shallow water equations with a source term and indicated that it performs better than the WENO scheme with Runge-Kutta time discretization in term of accuracy and cost. Stelling and Zijlema [24] developed an accurate and efficient finite difference algorithm for static free-surface flow with non-hydrostatics assumption and applied it to predict wave propagation.

On the other hand, Sheu and Fang [25] presented the Taylor-Galerkin finite-element model to simulate the shallow water equations for wave propagation in two dimensions. Dawson and Proft [26] coupled the continuous and discontinuous Galerkin methods to solve the two-dimensional shallow water equations. The software TELEMAC is used to simulate the shallow water flows, which is developed by the finite element method and has been used widely [27]. Since then, Comblen [28] et al. developed a finite element method for solving the shallow water equations on the sphere. Liang et al. [29] used the least-squares finite-element method to solve the shallow-water equations.

The FVM is also popular for solving the shallow water equations. The application of FVM to solve the shallow water equations can be divided into three categories according to the type of flows [30] as follows:

The first kind of model is used to simulate the discontinuities supercritical flows such as dam-break flow [31-35]. In these models, the upwind schemes which include flux splitting, approximate Riemann solvers, Godunov schemes and flux limiters are adopted.
The second kind of model is similar to the previous models except that they can also simulate wind waves, wave setup, and low frequency waves [36-38]. In [36] breakers were used to represent as abrupt discontinuities in the shallow water equations. In [37, 38], an upwind FVM was adopted with an approximate Riemann solver. Wei et al. [38] presented a model based on a Godunov-type scheme with Riemann solver to simulate

shock waves and solitary waves. The third model is applied to tidal flow and wind-induced current in river and estuaries [39-43]. The SIMPLE algorithm is used to couple the water elevation and velocity component in these models [37].

1.3 Lattice Boltzmann Method for Shallow Water Flows

On the other hand, developed from lattice gas automata, the lattice Boltzmann method (LBM) has become a very successful alternative numerical method for computational fluid dynamics.

Unlike traditional computational fluid dynamics (CFD), the LBM is a microscopic method. The fundamental idea behind LBM is to establish a simplified kinetic model to obey the corresponding macroscopic equations, i.e. N-S equations or shallow water equations. By Chapman-Enskog expansion, the lattice Boltzmann equation can recover the corresponding macroscopic equations. The LBM is based on statistical physics and can be regards as a kind of kinetic method.

Born about twenty years ago, the LBM has been applied successfully to simulate complex flow, especially for flows which involve complex boundary conditions and interfaces between different fluids [44, 45]. For example, Zhang' research group [46-50] applied successfully the LBM to non-equilibrium gas dynamics and microfluid. Their study demonstrated the advantage of LBM in simulating multi-scale and multi-physical flows. The development and application of LBM during the last two decades has been well reviewed [44, 45]. As a relative new method of simulating the fluid, the LBM is still under development and it has many attractive properties. The main characteristics of the LBM have been summarised and reviewed by several researchers [3, 44, 45, 51, 52]. Firstly, its algorithm is simple and efficient as only one single variable needs to be calculated. This distinguishes it from the conventional numerical methods like the finite difference and finite volume methods, which solve the nonlinear partial differential equations with the aid of a special treatment for either pressure or advection terms. Secondly, the LBM has an inherent feature for parallel computation with little extra coding, which is ideal and necessary to simulate a large-scale real life flow problems. Thirdly, it is easy to implement different boundary conditions, resulting in a very efficient model for flows in complex geometries with variation in boundary such as porous media, which still challenge the conventional numerical method.

The lattice Boltzmann method has been developed and used to solve the shallow water equations successfully [3, 53-60]. Salmon [53] developed a lattice Boltzmann model for ocean circulation. Zhou [3] derived the lattice Boltzmann method for shallow waters and discussed the force term representation in which a centred scheme is proposed, and proposed the elastic collision scheme for irregular boundary condition. Furthermore, he [3] developed the lattice Boltzmann model including the turbulence. Liu et al. developed a second order boundary for curved boundary [56] and a multi-block scheme for LBM for shallow water flows [61]. Li and Huang [55] studied the advection and anisotropic dispersion problem using LBM for shallow water flows. Tubbs [62] proposed a lattice Boltzmann method for multilayer shallow water equations by parallel computation.

1.4 Lattice Gas Automata

Lattice gas automaton (LGA) is a special kind of cellular automata. It is a simple model with discrete space, time, and particle velocities in which fictitious particles reside on a regular lattice.

The first discrete model for fluid on a square lattice (HPP model) was proposed by Hardy et al. [63] in 1976 which is the most simple LGA model for two-dimensional flows. However, the N-S equations cannot be recovered from the HPP because of insufficient symmetry of lattice [64]. In 1986, the correct lattice gas automaton (FHP model) was proposed firstly by Frisch et al. [65] which can recover the N-S equations.

The LGA consists of two sequential steps: streaming and collision. In streaming, each particle moves to the nearest node along the direction of its velocity; then, collision happens when particles arriving at one node and change their velocity directions according to the assumed rules. If the exclusion principle: (i.e. no more than one particle being allowed at a given time and node with a given velocity) is adopted for memory efficiency and it will result in a Fermi-Dirac local equilibrium distribution [66]. The LGA equation is

$$n_\alpha(x + e_\alpha, t + 1) = n_\alpha(x, t) + \Omega_\alpha[n(x, t)], \alpha = 0,1, \dots, K, \tag{1.1}$$

where n_α is a Boolean variable that is used as an indication of the presence or absence of a particle, t is the time, e_α is the local constant particle velocity, Ω_α is the collision operator, and K is the number of directions of the particle velocities at each node.

The physical variables, density and velocities are defined by

$$\rho = \sum_{\alpha=0}^{M} \langle n_\alpha \rangle, \qquad (1.2) \qquad\qquad u_i = \frac{1}{\rho} \sum_{\alpha=0}^{M} \langle n_\alpha \rangle e_{\alpha i}, \qquad (1.3)$$

in which $\langle n_\alpha \rangle$ denotes the ensemble average of n_α in statistical physics.

The LGA has two main disadvantages: the first is statistical noise like any particle method, and the second one is computational complexity which is serious for three-dimensional cases. In order to overcome these disadvantages, the lattice Boltzmann method has been developed [51].

1.5 Lattice Boltzmann Method

1.5.1 Lattice Boltzmann Equation

As stated before, the lattice Boltzmann method originated from the lattice gas automaton (LGA) to overcome its shortcoming. The main difference between LBM and LGA is to replace the Boolean variable with single-particle distribution functions, i.e. $\langle n_\alpha \rangle = f_\alpha$ $(f_\alpha \geq 0)$in LBM. Meanwhile, individual particle motion and particle-particle correlations in the kinetic equations are neglected. Equation (1.1) can be rewritten as the following lattice Boltzmann equation [67],

$$f_\alpha(x + e_\alpha, t + 1) = f_\alpha(x, t) + \Omega_\alpha[f(x, t)], \quad \alpha = 0,1, \dots, M. \qquad (1.4)$$

This procedure eliminates the statistical noise in a LGA and retains all the advantages of locality in the LGA which is essential for parallel computing [44].

The lattice Boltzmann method was introduced first as an independent numerical method by McNamara and Zanetti [67] in 1988. Higuera and Jiménez [68] made an important simplification for the collision operator and they linearized the collision term by assuming the distribution is close to its local equilibrium state. A particular simple linearized form for the collision operator is to use a single time relaxation towards the local equilibrium, which is known as Bhatngar-Gross-Krook [69] collision operator, is proposed by some researchers [70, 71]. This scheme makes the LBM become a very efficient method for simulating fluid flows. Up to now, the lattice Boltzmann equation with the BGK collision operator is still the most popular lattice Boltzmann method. Over the past years, the lattice Boltzmann methods for fluid flows has attracted much attention and been improved and extended greatly [44, 45]. The development of LBM will be reviewed briefly in the following sections.

1.5.2 Entropic Lattice Boltzmann Method

It is found that when the LBM with BGK is applied to high Reynolds number flows, it will become unstable [45]. The study indicates that an multiple-relaxation-time (MRT) can improve it, but it cannot remove this problem and the fundamental reason of this is that for a given lattice, the velocity or its spatial gradient is too large which leads to the negative values of distribution function. As the BGK-LBM abandoned the *H* theorem, no constraint is imposed on the evolution of distribution functions to ensure their non-negative behaviour at every grid point at all times. In order to overcome this shortcoming, Entropic LBM (ELBM) is proposed [72-76]. Normally, there are two kinds of ELBM and Keating et al. [77] reconciled them and showed some similarities. With Gauss-Hermite quadratures, the discrete form of the standard continuum *H* function can be written to

$$H(f_i) = \sum_{i=1}^{Q} f_i \ln\left(\frac{f_i}{w_i}\right), \tag{1.5}$$

where $\sum_{i=1}^{Q} w_i = 1$.

In the ELBM, the collision term is determined in order to extreme *H* and to keep balance on a constant entropy surface,

$$H(f_1', \dots, f_Q') = H(f_1, \dots, f_Q). \tag{1.6}$$

To make sure that *H* never reduces, extreme value of the functional δH_f is given by (Here $\mu(r,t)$ and $\beta(r,t)$ are Lagrange multipliers)

$$\delta H_f = \delta \sum_{i=1}^{Q} [b_i(f_i) - \mu f_i - \beta_\alpha f_i e_{i\alpha}] = 0, \tag{1.7}$$

where $b_i(f_i) = f_i \ln(f_i/w_i)$.

Due to the requirement of the mass and momentum conservation, the f_i^{eq} is the exponential form. The Lagrange multipliers can be obtained according to the first and second moments, ρ and ρu_α. As shown in references [72-74, 78-80], for the D3Q27 model the f_i^{eq} can be expressed by

$$f_i^{eq} = \rho w_i \prod_{\alpha=1}^{3} (2 - B) \left(\frac{2u_\alpha + B_1}{1 - u_\alpha}\right)^{e_{i\alpha}} \quad i=1,\dots,27, \tag{1.8}$$

with $B_1 = \sqrt{1+3u_\alpha^2}$, and the detail including weights w_i can be found in [45]. The expression for f_i^{eq} in the above equation is also valid for lattice models D3Q15 and D3Q19 [77]. Furthermore, reducing the number of discrete velocities leads to minor difference as indicated by Keating et al. [77]. However, Luo et al. [81] compared LBM with multiple-relaxation-time (MRT-LBM), LBM with two-relaxation-time (TRT-LBM), LBM with single-relaxation-time (SRT-LBM), ELBE for the N-S equations. In his study, it is indicated that ELBE seems do not improve the numerical stability of SRT-LBM, and both of MRT-LBM and TRT-LBM are better than ELBE and SRT-LBM in terms of accuracy, stability, and computational efficiency. Therefore, it needs further study on the performance of the ELBE.

1.5.3 Two-Relaxation-Time lattice Boltzmann Method

As an improved model on the LBGK, the two-relaxation-time lattice Boltzmann model is proposed by Ginzburg et al. [82] and applied to the advection and anisotropic-dispersion equations, demonstrating its advantage. When the two relaxation times take the same values, the TRT-LBM is reduced to SRT-LBM. On the other hand, TRT-LBM can be connected with the MRT-LBM with relaxation times which will be described in the next section.

1.5.4 Multiple-Relaxation-Time Lattice Boltzmann Method

The multiple-relaxation-time lattice Boltzmann equation is developed by d'Humieres [83], which overcomes the disadvantage of LBM with BGK (BGK-LBM) as indicated in [84]. Lallemand and Luo [85] studied the stability of MRT-LBM and showed that the MRT-LBM is much more stable than BGK-LBM because of the use of different relaxation times which can be tuned for optimal stability. In recent years, the MRT-LBM becomes increasingly popular. The MRT-LBM is briefly introduced as follows:

If the D2Q9 model is adopted, the evolution equation for the MRT-LBM without external force term is [83, 85]

$$f_\alpha(\boldsymbol{x} + \boldsymbol{e}_\alpha \Delta t, t + \Delta t) - f_\alpha(x,t) = -(\boldsymbol{T_r}^{-1}\boldsymbol{S})_{\alpha i}\left(m_i(x,t) - m_i^{eq}(x,t)\right) \quad (1.9)$$

where $m = \boldsymbol{T_r} f$, $f = \boldsymbol{T_r}^{-1} m$ and $\boldsymbol{S}$ is the relaxation matrix, $\boldsymbol{S}$=diag (s_0, s_1, s_2, s_3, s_4, s_5, s_6, s_7, s_8), $\boldsymbol{T_r}$ is the transform matrix defined in [85], f_a is the distribution function of particle. The equilibrium values of moments m^{eq} is

$$m^{eq}_{(1\ldots9)} = (\rho, -2\rho + 3\left(j_x^2 + j_y^2\right), \rho - 3\left(j_x^2 + j_y^2\right)/\rho, j_x, -j_x, j_y, -j_y, \frac{\left(j_x^2 - j_y^2\right)}{\rho}, \frac{j_x j_y}{\rho})^T \tag{1.10}$$

Using the Chapman-Engkog procedure, the N-S equations (2.5) and (2.6) can be recovered with the kinematic viscosity

$$\nu = \Delta te^2 \left(\frac{1}{s_7} - \frac{1}{2}\right)/6 = \Delta te^2 \left(\frac{1}{s_8} - \frac{1}{2}\right)/6. \tag{1.11}$$

The other relaxation parameters can be chosen freely in the range of 0~2 in order to achieve most stable LBM [85].

1.5.5 Grid Refinement

In the LBM, the Cartesian coordinate is employed which means that a regular grids have been used in computation. There are two challenges of using the uniform grids: the first one is difficulty in providing the results with high resolution near the solid boundary; the other one is that it uses too much or less uniform grids in an unnecessary or necessary flow regions, which results in waste of calculation power or inaccurate solution [86]. One way to resolve the problems is to divide the computation domain into different blocks and use different grid sizes in each block such as that used in the conventional CFD. Although the rectangular lattice Boltzmann method proposed by Zhou [87, 88] and Lallemand et al. [89] can reduce computational effort for flows with dominant flow feature in one direction, the grid refinement is desirable for most cases and some progress has been made in recent years.

The first grid refinement method for LBM is proposed by Filippova and Hanel [90] in 1998, which is a second-order scheme. Lin and Lai [91] proposed a grid structure which consists of a coarse base grid and one or several fine grids. The coarse grids cover the whole computational domain but the fine grids are only placed at parts where local grid refinement is needed. The simulation is first carried out on the coarse grid level, so that large-scale flow features can be obtained. Later, fine grid variables are initiated. The information between two level grids can be exchanged on the grid interface.

Based on multiple nested lattices with increasing resolution, Kandhai et al.[92] described a Finite-Difference Lattice Boltzmann method with BGK on nested grids. The calculation is carried out on each sub-lattice and interpolation is used to couple the sub-grids between the interfaces. On the other hand, in the method proposed by Yu et al. [86], the blocks with different grid sizes are not overlapped each other, and blocks are only connected through the interface. Liu applied the non-overlapped multi-block grid to LABSWE and improve its accuracy and efficiency [93]. Other progress on grid refinement can be found in reference [94].

1.5.6 Parallel Computation

For practical projects, a huge number of grids are needed and it requires high computational power. Therefore, parallel computation is desirable for all kinds of numerical methods. One of the most attractive features of the LBM is that it is easy to implement the parallel computation. In the LBM, the current value of the distribution function depends only on the previous conditions and the collision step is local.

Parallel computation of the LBM can further be enhanced by using the CPU-based computing systems, which has attracted many researchers' attention [95-97]. The parallel computation of LBM on CPU-based architectures can be achieved on both distributed and shared memory systems. For example, Desplat et al. [98] presented a parallel LBM code named LUDWIG, in which implementing message passing interface (MPI) is used to achieve full portability and good efficiency on both massively parallel processors (MPP) and symmetric multiprocessing (SMP) systems.

Recently, the LBM has been implemented on hardware accelerated systems using Graphics Processing Units (GPU) and has been accelerated on a single GPU [99-101] or a GPU cluster [102] with MPI. Furthermore, the LBM for the two dimensional Navier-Stokes equations was carried out using the Compute Unified Device Architecture (CUDA^{TM}) interface developed by NVIDIA^{R}.

The parallel computation of LBM for shallow water basing on CPU and GPU was studied by Tubbs [103] and showed attractive performance.

1.5.7 Moving Boundary

The moving body boundary is a time dependent problem involves the solid-fluid interaction, moving solid and moving boundary. In order to solve this problem, two kinds of method have been proposed: the Lagrangian methods and Eulerian methods [104].

In the Lagrangian methods, a mesh is moving as the moving solid in which the solid-fluid interface can be captured accurately. But, the mesh regeneration is needed at every time step in this method, which is time consuming, which reduces the efficiency.

On the other hand, the Eulerian method use a fixed mesh in which the exact location of interface is unknown and this results in the difficulty in improving the accuracy when the solid shape is irregular .

For the lattice Boltzmann method, because it is local for calculation and use the fixed Cartesian grid, it seem that it is easy to implement the moving boundary as shown in the later chapter. Based on the curved boundary conditions, the moving boundary for Navier-Stokes equations using the lattice Boltzmann method has been studied by Lallemand and Luo [105] and Kao and Yang [106]. Lallemand and Luo [105] extended Bouzidi’s method [107] and studied the moving boundary systematically. Kao and Yang [106] summarized various approaches for a curved boundary and proposed a new method for curved boundary and moving boundaries with the interpolation-free treatment.

1.6 Objectives

Although developed quickly over the past two decades, the lattice Boltzmann method is still a relative new method compared to the traditional CFD methods. It has some drawbacks and needs further improvement. Furthermore, in spite of the fact that the lattice Boltzmann method for the shallow water equations has demonstrated its potential and attractive capabilities in simulating shallow water flows, it still needs to be improved and tested for more flow problems. Therefore, the applications and improvement on the LBM for shallow water flows is the current aim. The detailed objectives of this thesis can be summarized as follows:

1. To study and apply the LBM to the shallow water equations and solute transport equation in environmental problems. The multiple-relaxation-time and single-relaxation-time are adopted in the LBM for shallow water equations and the large eddy simulation is incorporated into the LABSWE.

2. To predict the asymmetric flows in rectangular basins by LABSWE^{TM} and test the feasibility and accuracy of LABSWE^{TM} for free surface flows.

3. To investigate the performance of LABSWE with MRT (LABSWE^{MRT}) and the LBM with SRT collision operator (LABSWE and LABSWE^{TM}). The purpose of adopting the MRT is to improve the stability and accuracy of the simulations.

4. To improve the LBM for simulating the two-dimensional shallow water flows over discontinuous beds. The flows are simulated by LABSWE^{MRT} in which the weighted centred scheme for force term together with the bed height for a bed slope was used to improve simulation of flows over discontinuous bed. Furthermore, the resistance stress is added to include the flow head loss caused by a step.

5. To extend to LABSWE^{MRT} to simulate a moving body in shallow waters. In order to deal with the moving boundaries, three different schemes for a curved boundary condition at second order accuracy are used and compared. Furthermore, certain momentum is added to reflect interaction between the fluid and the solid and a refill method for new wetted nodes moving out from solid nodes has been proposed.

6. To investigate the solute transport in shallow water flows by the LBM. The flows are solved using LABSWE and LABSWE^{MRT}, and the advection-diffusion equation is also solved with a BGK-LBM on a D2Q5 lattice. Three cases: open channel flow with side discharge, shallow recirculation flow and flow in a harbour are simulated to verify the described methods.

7. To develop a coupled model for simulation of the morphological evolution under shallow water flows. The flow fields are solved by LABSWE^{MRT} with the improved

scheme for the force term. The fifth order Euler-WENO scheme is used to solve the morphological equation for the bed evolution caused by bed-load sediment transport.

1.7 Outline of the Thesis

This thesis consists of nigh chapters.

The chapter 1 introduces the research background and the history of the lattice Boltzmann method, reviews the development and application of LBM in recent years briefly and outlines the objectives of this thesis.

Chapter 2 briefly describes the N-S equations and the shallow water equations without turbulence and with turbulence by Subgrid-Scale Stress (SGS) model, in which the shallow water equations are derived from the N-S equations in detail.

Chapter 3 presents the lattice Boltzmann method for shallow water flows, including LABSWE, LABSWE^{TM}, and LABSWE^{MRT}. With these three kinds of lattice Boltzmann methods, the corresponding shallow water equations are recovered. A new form of force term is introduced in LABAWE^{MRT} which can improve the predicted results as shown in chapter 6.

Chapter 4 discusses the initial and boundary conditions used in the lattice Boltzmann method. In this chapter, the no-slip, semi-slip and slip boundary conditions are presented.

Chapter 5 applies LABSWE^{TM} to study free surface flows in rectangular shallow basins and simulates the flow over a discontinuous bed in which water head loss caused by a step has been considered.

Chapter 6 studies the application of the LBM for solute transport in which the advection-diffusion equation has been coupled with the shallow water equations. Furthermore, the performance of LABSWE and LABSWE^{MRT} are compared in detail.

Chapter 7 uses LABSWE^{MRT} to simulate a moving body and compares the predicted results with corresponding experimental results, in which three different kinds of curved boundary conditions have been investigated in detail.

Chapter 8 applies the LABSWE^{MRT} to predict morphological evolution which is dominated by bed-load transport.

Chapter 9 summarises the conclusions and recommends future work.

Chapter 2: Governing Equations for Shallow Water Flows

2.1 Introduction

In physics and engineering, the basic laws are conservation of mass, momentum and energy. But for isothermal flow, the law of energy is not included. In this chapter, the Navier-Stokes (N-S) equations which are the governing equations for the motion of fluid are introduced, followed by the introduction of its simplified version, the shallow water equations. Furthermore, the shallow water equations are derived in detail from the N-S equations and it can be used to describe the flow in which the horizontal scale is much larger than the vertical scale. Numerical methods for turbulent flow are described, in which the large eddy simulation is emphasized. Last, the shallow water equations including SGS model are presented.

2.2 The Navier-Stokes Equations

The governing equations for general incompressible flows are the three-dimensional continuity and Navier-Stokes (N-S) equations that are derived from Newton’s second law of motion and the mass conservation. If Cartesian coordinate is adopted, the N-S equations can be shown as follows:

$$\frac{\partial u}{\partial x}+\frac{\partial v}{\partial y}+\frac{\partial w}{\partial z}=0 \tag{2.1}$$

$$\frac{\partial u}{\partial t}+\frac{\partial (uu)}{\partial x}+\frac{\partial (uv)}{\partial y}+\frac{\partial (uw)}{\partial z}=\nu\left(\frac{\partial^2 u}{\partial x^2}+\frac{\partial^2 u}{\partial y^2}+\frac{\partial^2 u}{\partial z^2}\right)-\frac{1}{\rho}\frac{\partial p}{\partial x}+f_x \tag{2.2}$$

$$\frac{\partial v}{\partial t}+\frac{\partial (vu)}{\partial x}+\frac{\partial (vv)}{\partial y}+\frac{\partial (vw)}{\partial z}=\nu\left(\frac{\partial^2 v}{\partial x^2}+\frac{\partial^2 v}{\partial y^2}+\frac{\partial^2 v}{\partial z^2}\right)-\frac{1}{\rho}\frac{\partial p}{\partial y}+f_y \tag{2.3}$$

$$\frac{\partial w}{\partial t}+\frac{\partial (wu)}{\partial x}+\frac{\partial (wv)}{\partial y}+\frac{\partial (ww)}{\partial z}=\nu\left(\frac{\partial^2 w}{\partial x^2}+\frac{\partial^2 w}{\partial y^2}+\frac{\partial^2 w}{\partial z^2}\right)-\frac{1}{\rho}\frac{\partial p}{\partial z}+f_z \tag{2.4}$$

in which *x*, *y*, *z* are the Cartesian coordinate (see Fig. 2.1); *u*, *v*, and *w* are the corresponding velocity components, respectively; f_x, f_y, and f_z are the body forces per unit mass in the corresponding direction; ν is the kinematic viscosity; p is the pressure; ρ is the fluid density; and *t* is the time.

The equations (2.1-2.4) can also be written in tensor form as

$$\frac{\partial u_j}{\partial x_j} = 0 \tag{2.5}$$

$$\frac{\partial u_i}{\partial t} + \frac{\partial (u_i u_j)}{\partial x_j} = f_i - \frac{1}{\rho}\frac{\partial p}{\partial x_i} + \nu \frac{\partial^2 u_i}{\partial x_j x_j}, \tag{2.6}$$

where the subscripts i and j are space direction indices; f_i is the body force per unit mass acting on fluid in the i direction; and the Einstein summation convention is used.

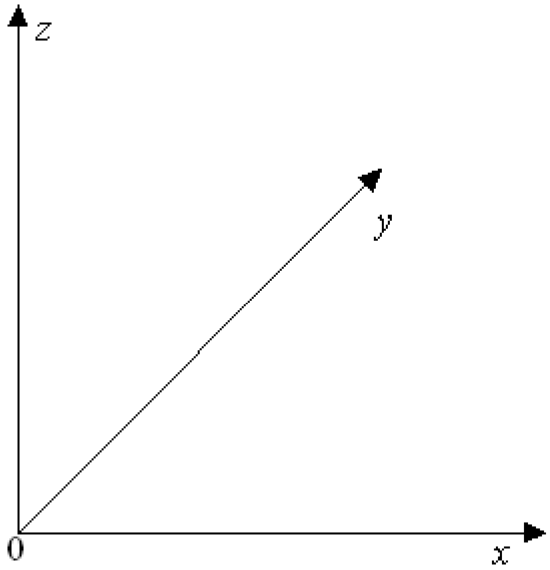

Figure 2.1 Cartesian coordinate system.

Physical interpretations can be given for all the terms in the N-S equations. The terms on the left-hand side of Eq. (2.6) is an inertia term in which the first and the second terms are called unsteady term and convective term respectively. The three terms on the right hand side of equation (2.6) are the body force term, the pressure term and the viscous term, respectively. Normally, there is no analytical solution to the N-S equations except for some simple situations. However, as computer power increases, it is feasible to obtain numerical solutions for the equations. Thus, numerical methods play an increasingly important role in solving flow problems in engineering.

2.3 The Shallow Water Equations

The flows in rivers, estuaries, and coastal areas can be described by the shallow water equations because the water depth is much smaller than the horizontal scale, in which the assumption of the hydrostatic pressure is adopted and hence the vertical acceleration is ignored. Stansby and Zhou [108] shows that both 2D and 3D shallow water equations cannot predict the vertical velocity accurately. Furthermore, the 2D shallow water equation is more efficient than the 3D. Therefore, the 2D shallow water equations are used in this thesis.

The shallow water equations are derived from depth-integrating the Navier–Stokes equations (2.1) - (2.4) with assumption implying that the vertical velocity of the fluid is small with hydrostatic pressure and constant velocities over the water depth [3]. The shallow water equations are thus derived in the following section.

The body forces for the flows can be divided into two categories: gravity and Coriolis acceleration because of the earth's rotation [109]. With the Cartesian coordinate system, the body force can be described by

$$f_x = f_c v, f_y = -f_c u,\ f_z = -g, \tag{2.7}$$

in which, g =9.81m/s^2 is the gravitational acceleration; $f_c = 2\omega sin\phi$ is the Coriolis parameter with $\omega \approx 7.3\ \times 10^{-5}\ rad/s$ which is the earth's rotation and ϕ is the earth's latitude at the corresponding site.

Firstly, the continuity equation for shallow water equations is derived by integrating Eq. (2.1) over depth,

$$\int_{z_b}^{h+z_b} \left(\frac{\partial u}{\partial x} + \frac{\partial v}{\partial y} + \frac{\partial w}{\partial z}\right) dz = 0, \tag{2.8}$$

which results in

$$\int_{z_b}^{h+z_b} \frac{\partial u}{\partial x} dz + \int_{z_b}^{h+z_b} \frac{\partial v}{\partial y} dz + w_s - w_b = 0 \tag{2.9}$$

where w_b and w_s are the vertical velocities at channel bottom and the free surface, respectively; and z_b is the bed elevation above a datum (see Fig. 2.2).

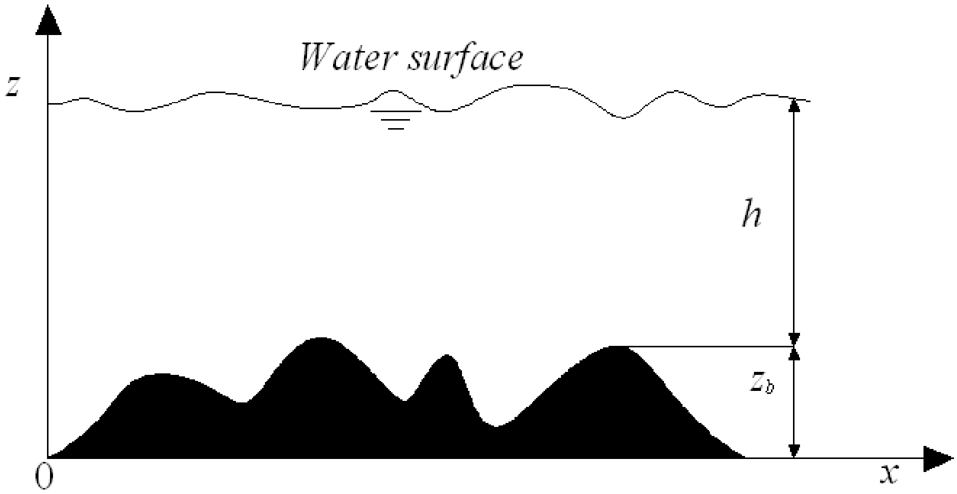

Figure 2.2 Shallow water flow sketch.

The Leibnitz rule can be expressed [110],

$$\int_a^b \frac{\partial f(x,y)}{\partial y} dx = \frac{\partial}{\partial y}\int_a^b f(x,y)dx - f(b,y)\frac{\partial b}{\partial y} + f(a,y)\frac{\partial a}{\partial y}, \tag{2.10}$$

The first and second terms on the left hand side of Eq. (2.9) can be written as

$$\int_{z_b}^{h+z_b} \frac{\partial u}{\partial x} dz = \frac{\partial}{\partial x}\int_{z_b}^{h+z_b} u dz - u_s\frac{\partial}{\partial x}(h+z_b) + u_b\frac{\partial z_b}{\partial x}, \tag{2.11}$$

$$\int_{z_b}^{h+z_b} \frac{\partial v}{\partial y} dz = \frac{\partial}{\partial y}\int_{z_b}^{h+z_b} v dz - v_s\frac{\partial}{\partial y}(h+z_b) + u_b\frac{\partial z_b}{\partial y}, \tag{2.12}$$

Substituting Eqs. (2.11) and (2.12) into (2.9) leading to

$$\frac{\partial}{\partial x}\int_{z_b}^{h+z_b} udz + \frac{\partial}{\partial y}\int_{z_b}^{h+z_b} vdz + \left[w_s - u_s\frac{\partial}{\partial x}(h+z_b) - v_s\frac{\partial}{\partial y}(h+z_b)\right] - \left[w_b - u_b\frac{\partial z_b}{\partial x} - v_b\frac{\partial z_b}{\partial y}\right] = 0 \tag{2.13}$$

The kinematic conditions at the free surface and channel bottom are,

$$w_s = \frac{\partial}{\partial t}(h+z_b) + u_s\frac{\partial}{\partial x}(h+z_b) + v_s\frac{\partial}{\partial y}(h+z_b), \tag{2.14}$$

$$w_b = \frac{\partial z_b}{\partial t} + u_b\frac{\partial z_b}{\partial x} + v_b\frac{\partial z_b}{\partial y}. \tag{2.15}$$

Substituting Eqs. (2.14) and (2.15) into Eq. (2.13) results in

$$\frac{\partial h}{\partial t} + \frac{\partial(h\bar{u})}{\partial x} + \frac{\partial(h\bar{v})}{\partial y} = 0, \tag{2.16}$$

which is just the continuity equation for the shallow water equations and $\bar{u}$ and $\bar{v}$ are depth-averaged velocity components and defined as

$$\bar{u} = \frac{1}{h}\int_{z_b}^{h+z_b} u dz \quad (2.17), \qquad \bar{v} = \frac{1}{h}\int_{z_b}^{h+z_b} v dz. \quad (2.18)$$

Next, the momentum equation for shallow water flow will be derived. Eq. (2.2) is integrated over water depth and the following expression can be obtained:

$$\int_{z_b}^{h+z_b}\left[\frac{\partial u}{\partial t}+\frac{\partial(uu)}{\partial x}+\frac{\partial(uv)}{\partial y}+\frac{\partial(uw)}{\partial z}\right]dz = \int_{z_b}^{h+z_b} f_c v dz + \int_{z_b}^{h+z_b}\left[-\frac{1}{\rho}\frac{\partial p}{\partial x}+\nu\left(\frac{\partial^2 u}{\partial x^2}+\frac{\partial^2 u}{\partial y^2}+\frac{\partial^2 u}{\partial z^2}\right)\right]dz \quad (2.19)$$

Once again, the Leibnitz rule (2.10) is used for the first three terms on the left-hand side of the Eq. (2.19) leads to

$$\int_{z_b}^{h+z_b}\frac{\partial u}{\partial t}dz = \frac{\partial}{\partial t}\int_{z_b}^{h+z_b} u dz - u_s\frac{\partial}{\partial t}(h+z_b) + u_b\frac{\partial z_b}{\partial t}, \quad (2.20)$$

$$\int_{z_b}^{h+z_b}\frac{\partial(uu)}{\partial x}dz = \frac{\partial}{\partial x}\int_{z_b}^{h+z_b} uu dz - u_s u_s\frac{\partial}{\partial x}(h+z_b) + u_b u_b\frac{\partial z_b}{\partial x}, \quad (2.21)$$

$$\int_{z_b}^{h+z_b}\frac{\partial(vu)}{\partial y}dz = \frac{\partial}{\partial y}\int_{z_b}^{h+z_b} vu dz - v_s u_s\frac{\partial}{\partial y}(h+z_b) + v_b u_b\frac{\partial z_b}{\partial y}. \quad (2.22)$$

The last term on the left hand side of Eq. (2.19) can be integrated, leading to

$$\int_{z_b}^{h+z_b}\frac{\partial(wu)}{\partial z}dz = w_s u_s - w_b u_b . \quad (2.23)$$

Combining it with Eqs. (2.20) - (2.23) and rewriting the results yields the following equation

$$\begin{aligned}\int_{z_b}^{h+z_b}\left[\frac{\partial u}{\partial t}+\frac{\partial(uu)}{\partial x}+\frac{\partial(uv)}{\partial y}+\frac{\partial(uw)}{\partial z}\right]dz &= \frac{\partial}{\partial t}\int_{z_b}^{h+z_b} u dz + \frac{\partial}{\partial x}\int_{z_b}^{h+z_b} uu dz + \frac{\partial}{\partial y}\int_{z_b}^{h+z_b} vu dz \\ &+ u_s\left[w_s - \frac{\partial}{\partial t}(h+z_b) - u_s\frac{\partial}{\partial x}(h+z_b) - v_s\frac{\partial}{\partial y}(h+z_b)\right] - u_b\left(w_b - \frac{\partial z_b}{\partial t} - u_b\frac{\partial z_b}{\partial x} - v_b\frac{\partial z_b}{\partial y}\right)\end{aligned} \quad (2.24)$$

Refer to the kinematic conditions (2.14) and (2.15). Combined with the Eqs. (2.17) and (2.18), Eq. (2.24) can be rewritten as

$$\int_{z_b}^{h+z_b}\left[\frac{\partial u}{\partial t}+\frac{\partial(uu)}{\partial x}+\frac{\partial(uv)}{\partial y}+\frac{\partial(uw)}{\partial z}\right]dz = \frac{\partial(\bar{u}h)}{\partial t} + \frac{\partial}{\partial x}\int_{z_b}^{h+z_b} uu dz + \frac{\partial}{\partial y}\int_{z_b}^{h+z_b} vu dz \quad (2.25)$$

With the second mean value theorem for integrals[111],

$$\int_a^b f(x)g(x)dx = f(\zeta)\int_a^b g(x)dx \,, \tag{2.26}$$

The second term on the right-hand side of Eq. (2.25) can be expressed as

$$\int_{z_b}^{h+z_b} uudz = \breve{u}_1 \int_{z_b}^{h+z_b} udz = \breve{u}_1 h\bar{u} \,, \tag{2.27}$$

And the last term on the right-hand side of Eq. (2.25) can be expressed as

$$\int_{z_b}^{h+z_b} vudz = \breve{u}_2 \int_{z_b}^{h+z_b} udz = \breve{u}_2 h\bar{v} \,, \tag{2.28}$$

Assuming $\breve{u}_1 = \theta_1\bar{u}$ and $\breve{u}_2 = \theta_2\bar{u}$ and substituting Eqs. (2.27) and (2.28) into Eq. (2.25) leads to

$$\int_{z_b}^{h+z_b}\left[\frac{\partial u}{\partial t}+\frac{\partial(uu)}{\partial x}+\frac{\partial(uv)}{\partial y}+\frac{\partial(uw)}{\partial z}\right]dz = \frac{\partial(\bar{u}h)}{\partial t}+\frac{\partial(\theta_1 h\bar{u}\bar{u})}{\partial x}+\frac{\partial(\theta_2 h\bar{v}\bar{u})}{\partial y}\,, \tag{2.29}$$

where $\theta_1$and θ_2 are momentum correction factors and are determined by Eqs. (2.27) and (2.28) as

$$\theta_1 = \frac{1}{h\bar{u}\bar{u}}\int_{z_b}^{h+z_b} uudz, \quad (2.30) \qquad\qquad \theta_2 = \frac{1}{h\bar{v}\bar{u}}\int_{z_b}^{h+z_b} vudz. \quad (2.31)$$

Similarly, the following expression for the terms on the left hand side of equation (2.3) can be obtained.

$$\int_{z_b}^{h+z_b}\left[\frac{\partial v}{\partial t}+\frac{\partial(uv)}{\partial x}+\frac{\partial(vv)}{\partial y}+\frac{\partial(wv)}{\partial z}\right]dz = \frac{\partial(\bar{v}h)}{\partial t}+\frac{\partial(\theta_2 h\bar{u}\bar{v})}{\partial x}+\frac{\partial(\theta_3 h\bar{v}\bar{v})}{\partial y}\,, \tag{2.32}$$

in which, an additional momentum correction factor θ_3 is defined by

$$\theta_3 = \frac{1}{h\bar{v}v}\int_{z_b}^{h+z_b} vvdz \,. \tag{2.33}$$

The first term on the right hand side of Eq. (2.19) is integrated as

$$\int_{z_b}^{h+z_b} f_c vdz = f_c h\bar{v} \,. \tag{2.34}$$

Since the vertical acceleration can be ignored in comparison with the horizontal effect in shallow water flows, the momentum equation (2.6) in the z direction is reduced with $\omega \approx 0$ to

$$\frac{\partial p}{\partial z} = -\rho g, \tag{2.35}$$

which is integrated and the following expression can be obtained

$$p = -\rho g z + C_0, \tag{2.36}$$

where C_0 is an integration constant.

The pressure at the free surface is the atmospheric pressure p_a, for example: $p = p_a$ at $z = h + z_b$, in above equation, C_0 can be calculated by

$$C_0 = \rho g(h + z_b) + p_a. \tag{2.37}$$

Substituting Eq. (2.37) into Eq. (2.36) results in

$$p = \rho g(h + z_b - z) + p_a. \tag{2.38}$$

Normally, $p_a$is almost constant in the corresponding area and often assumed to be zero, i.e. $p_a = 0$. Because the difference in atmospheric pressure at water surface is usually small in most shallow water flows [112], Eq. (2.38) reads

$$p = \rho g(h + z_b - z)\ . \tag{2.39}$$

The Equation (2.39) is often referred to as the hydrostatic pressure approximation in shallow water flows and differentiating it to *x* gives

$$\frac{\partial p}{\partial x} = \rho g \frac{\partial}{\partial x}(h + z_b). \tag{2.40}$$

Because both of water depth h and the bed height $z_b$are functions of the horizontal coordinates *x* and *y* only, the following expression can be obtained:

$$\int_{z_b}^{h+z_b} \frac{1}{\rho}\frac{\partial p}{\partial x} dz = \frac{h}{\rho}\frac{\partial p}{\partial x}. \tag{2.41}$$

Combining Eq. (2.40) with Eq. (2.41) can give

$$\int_{z_b}^{h+z_b} \frac{1}{\rho}\frac{\partial p}{\partial x} dz = gh\frac{\partial}{\partial x}(h + z_b). \tag{2.42}$$

The following approximations are given for the third and fourth terms on the right hand side of Eq. (2.19).

$$\int_{z_b}^{h+z_b} \nu \frac{\partial^2 u}{\partial x^2} dz \approx \nu \frac{\partial^2 (h\bar{u})}{\partial x \partial x}\ , \tag{2.43}$$

$$\int_{z_b}^{h+z_b} \nu \frac{\partial^2 u}{\partial y^2} dz \approx \nu \frac{\partial^2 (h\bar{u})}{\partial y \partial y}\ . \tag{2.44}$$

The last term on the right hand side of Eq. (2.19) is calculated as

$$\int_{z_b}^{h+z_b} \nu \frac{\partial^2 u}{\partial z^2} dz = \left(\nu \frac{\partial u}{\partial z}\right)_s - \left(\nu \frac{\partial u}{\partial z}\right)_b, \tag{2.45}$$

Normally, the terms on the right hand side of Eq. (2.45) can be approximated with the surface wind shear stress and the bed shear stress in the *x* direction, respectively,

$$\left(\nu \frac{\partial u}{\partial z}\right)_s = \frac{\tau_{wx}}{\rho}, \tag{2.46}$$

$$\left(\nu \frac{\partial u}{\partial z}\right)_b = \frac{\tau_{bx}}{\rho}. \tag{2.47}$$

Therefore, Eq. (2.45) can be written as

$$\int_{z_b}^{h+z_b} \nu \frac{\partial^2 u}{\partial x^2} dz = \frac{\tau_{wx}}{\rho} - \frac{\tau_{bx}}{\rho}. \tag{2.48}$$

Combining Eqs. (2.29), (2.34), (2.42)-(2.44), and (2.48) with Eq. (2.19) leads to

$$\frac{\partial(h\bar{u})}{\partial t} + \frac{\partial(\theta_1 h\bar{u}\,\bar{u})}{\partial x} + \frac{\partial(\theta_2 h\bar{v}\,\bar{u})}{\partial y} = -g\frac{\partial}{\partial x}\left(\frac{h^2}{2}\right) + \nu\frac{\partial^2(h\bar{u})}{\partial x\partial x} + \nu\frac{\partial^2(h\bar{u})}{\partial y\partial y} - gh\frac{\partial z_b}{\partial x} + f_c h\bar{v} + \frac{\tau_{wx}}{\rho} - \frac{\tau_{bx}}{\rho}. \tag{2.49}$$

The above equation is the momentum equation for shallow water flows in the *x* direction. The momentum equation in the *y* direction for shallow water flows can be derived similarly as

$$\frac{\partial(h\bar{v})}{\partial t} + \frac{\partial(\theta_1 h\bar{u}\,\bar{v})}{\partial x} + \frac{\partial(\theta_3 h\bar{v}\,\bar{v})}{\partial y} = -g\frac{\partial}{\partial y}\left(\frac{h^2}{2}\right) + \nu\frac{\partial^2(h\bar{v})}{\partial x\partial x} + \nu\frac{\partial^2(h\bar{v})}{\partial y\partial y} - gh\frac{\partial z_b}{\partial y} - f_c h\bar{u} + \frac{\tau_{wy}}{\rho} - \frac{\tau_{by}}{\rho}. \tag{2.50}$$

Theoretically, if the velocity profiles for *u* and *v* are known, the momentum correction factors θ_1, θ_2 and θ_3 can be calculated from Eqs. (2.30), (2.31) and (2.33). However, normally it is not easy to calculate these momentum correction factors θ_1, θ_2 and θ_3 because there are no universal velocity distribution which are valid for all flows. On the other hand, $\theta_1 = 1$, $\theta_2 = 1$ and $\theta_3 = 1$ are used widely in numerical simulation for shallow water flows and these study shows that this assumption can give good results for most shallow water flows [113-116].

Therefore, when $\theta_1 = 1$, $\theta_2 = 1$ and $\theta_3 = 1$ are adopted, Eqs. (2.49) and (2.50) become

$$\frac{\partial(h\bar{u})}{\partial t}+\frac{\partial(h\bar{u}\bar{u})}{\partial x}+\frac{\partial(h\bar{v}\bar{u})}{\partial y}=-g\frac{\partial}{\partial x}\left(\frac{h^2}{2}\right)+\nu\frac{\partial^2(h\bar{u})}{\partial x\partial x}+\nu\frac{\partial^2(h\bar{u})}{\partial y\partial y}-gh\frac{\partial z_b}{\partial x}+f_c h\bar{v}+\frac{\tau_{wx}}{\rho}-\frac{\tau_{bx}}{\rho}, \tag{2.51}$$

$$\frac{\partial(h\bar{v})}{\partial t}+\frac{\partial(h\bar{u}\bar{v})}{\partial x}+\frac{\partial(h\bar{v}\bar{v})}{\partial y}=-g\frac{\partial}{\partial y}\left(\frac{h^2}{2}\right)+\nu\frac{\partial^2(h\bar{v})}{\partial x\partial x}+\nu\frac{\partial^2(h\bar{v})}{\partial y\partial y}-gh\frac{\partial z_b}{\partial y}-f_c h\bar{u}+\frac{\tau_{wy}}{\rho}-\frac{\tau_{by}}{\rho}, \tag{2.52}$$

After the overbars are dropped for convenience, the continuity equation (2.16) and the momentum equations (2.51) and (2.52) can be expressed in a tensor form concisely as

$$\frac{\partial h}{\partial t}+\frac{\partial(hu_j)}{\partial x_j}=0, \tag{2.53}$$

$$\frac{\partial(hu_i)}{\partial t}+\frac{\partial(hu_iu_j)}{\partial x_j}=-g\frac{\partial}{\partial x_i}\left(\frac{h^2}{2}\right)+\nu\frac{\partial^2(hu_i)}{\partial x_j\partial x_j}+F_i\ , \tag{2.54}$$

in which, the force term F_i is defined as

$$F_i==-gh\frac{\partial z_b}{\partial x_i}+\frac{\tau_{wi}}{\rho}-\frac{\tau_{bi}}{\rho}+E_i\ , \tag{2.55}$$

where the Coriolis term E_i can be calculated by

$$E_i=\begin{cases} f_c hv, & i=x, \\ -f_c hu, & i=y. \end{cases} \tag{2.56}$$

The bed shear stress τ_{bi} in the *i* direction can be calculated by the depth-averaged velocities,

$$\tau_{bi}=\rho C_b u_i\sqrt{u_ju_j}, \tag{2.57}$$

where, C_b is the bed friction coefficient, estimated from $C_b=g/C_z^2$, where C_z is the Chezy coefficient calculated by either Manning equation (2.58), or the Colebrook-White equation (2.59) [117],

$$C_b=h^{\frac{1}{6}}/n_b\ , \tag{2.58}$$

in which, n_b is the Manning's coefficient at the bed,

$$C_z=-\sqrt{32g}\log_{10}\left(\frac{K_s}{14.8h}+\frac{1.255\nu C_z}{4\sqrt{2g}hu}\right), \tag{2.59}$$

in which K_s is the Nikuradse equivalent sand roughness and measured by experiments.

Furthermore, the wind shear stress can be obtained by

$$\tau_{wi}=\rho_a C_w u_{1wi}\sqrt{u_{1wj}u_{1wj}}\ , \tag{2.60}$$

in which, ρ_a is the density of air, u_{1wi} is the component of the relative wind velocity in the *i* direction, and C_w is the resistance coefficient of the water-air interface.

It should be pointed that the use of the second mean value theorem (2.26) implies that the horizontal velocities $u(x, y, z, t)$ and $v(x, y, z, t)$ do not change their directions along the water depth. It indicates that $u(x, y, z, t) \geq 0$ or $u(x, y, z, t) \leq 0$ from channel bed to free surface at location (x,y) and so is $v(x, y, z, t)$. This is the reason why a model based on 2D shallow water equations cannot predict flow separations in vertical direction accurately. In this section, the shallow water equations are derived briefly from the N-S equations and more details can be found in [3].

2.4 The Advection-diffusion Equation

The water depth-averaged advection-diffusion equation can be expressed as:

$$\frac{\partial(hC)}{\partial t} + \frac{\partial(u_i hc)}{\partial x_i} = \frac{\partial}{\partial x_i}\left(D_i \frac{\partial(hc)}{\partial x_i}\right) + S_c \qquad (2.61)$$

where the subscripts i and j are space direction indices and the Einstein summation convention is used, t is time, C is the depth-averaged concentration, D_i is the dispersion coefficient in direction i, S_c is the depth-averaged source term, h is water depth, u_i is velocity, x_i stands for either x or y in direction i or j. This equation is used for isotropic flow.

2.5 Numerical Methods for Turbulent Flow

Most fluid flows encountered in nature and engineering applications are turbulent. Numerical simulation of turbulent flows is important for researchers and engineers. Even though turbulent flow can be observed easily, it is difficult to describe it accurately. However, the following features are expected to exhibit for turbulent flows according to [118]:

(a) They are disorganized and chaotic.
(b) There is nonrepeatability.
(c) They have extremely large range of length and time scales but even the smallest scales are still large enough to satisfy the continuum hypothesis.
(d) It is three dimensional, time dependent and rotational.
(e) It is intermittent in both space and time.

In general, there are three kinds of numerical methods to simulate turbulent flow: Direct Numerical Simulation (DNS), Large Eddy Simulation (LES) and Reynolds-Averaged Navier–Stokes (RANS). McDonough [118] compared these three methods and summarized results as follows:

Firstly, although the DNS requires modelling, it demands resolution at all scales. This leads to total arithmetic scaling at least as Re^3 (Re is the Reynolds number), or worse. It is clear that it is unacceptable for engineering flows because the Re can be up to 10^4 or larger in engineering flows. This requirement has beyond the power of present computation.

For LES, the amount of required modelling is dependent on the amount of resolution, but it is unlikely that total arithmetic will scale worse than Re^2. LES has been incorporated into CFD software for practical engineering applications. Furthermore, it has been shown that LES procedures generally converge to DNS as discretization step size and filter widths are refined.

Finally, the RANS requires modelling of everything of all scales. As a consequence, total arithmetic is a weak function of Re at most. In which, the $k-\varepsilon$ model is most widely used.

In the present study, the LES is used to describe turbulent flow. In LES, the oldest, but yet still used widely, the Smagorinsky model [119] is used in this thesis because of its simplicity and easy implementation in the lattice Boltzmann method.

2.6 Subgrid-Scale Stress Model

The governing flow equations with the LES for turbulent flows can be derived by including a space-filtered quantity in the continuity equation (2.5) and the momentum equation (2.6). The space-filtered governing equations can be expressed as

$$\frac{\partial \tilde{u}_j}{\partial x_j} = 0 \tag{2.62}$$

$$\frac{\partial \tilde{u}_i}{\partial t} + \frac{\partial(\tilde{u}_i \tilde{u}_j)}{\partial x_j} = f_i - \frac{1}{\rho}\frac{\partial p}{\partial x_i} + \nu \frac{\partial^2 \tilde{u}_i}{\partial x_j \partial x_j} - \frac{\partial \tau_{ij}}{\partial x_j}, \tag{2.63}$$

in which $\tilde{u}_i$ is the space-filtered velocity component in the *i* direction and is defined by

$$\tilde{u}_i(z,y,z,t) = \iiint_{\Delta x\Delta y\Delta z} u(x,y,z,t)G(x,y,z,x',y',z')dx'dy'dz' \tag{2.64}$$

where G is a spatial filter function. τ_{ij} is the subgrid-scale stress (SGS) that reflects the effect of the unresolved scales with the resolved scales and determined by

$$\tau_{ij} = \widetilde{u_i u_j} - \tilde{u}_i\tilde{u}_j. \tag{2.65}$$

With the Bussinesq assumption for turbulent stresses, the subgrid-scale stress can be expressed using an SGS eddy viscosity ν_e as

$$\tau_{ij} = -\nu_e\left(\frac{\partial\tilde{u}_i}{\partial x_j} + \frac{\partial\tilde{u}_j}{\partial x_i}\right). \tag{2.66}$$

Substituting Eq. (2.66) into Eq. (2.63) gives the momentum equation,

$$\frac{\partial\tilde{u}_i}{\partial t} + \frac{\partial(\tilde{u}_i\tilde{u}_j)}{\partial x_j} = f_i - \frac{1}{\rho}\frac{\partial p}{\partial x_i} + (\nu + \nu_e)\frac{\partial^2\tilde{u}_i}{\partial x_j\partial x_j}. \tag{2.67}$$

If the standard Smagorinsky SGS model [119] is adopted and the eddy viscosity ν_e can be expressed by

$$\nu_e = (C_s l_s)^2\sqrt{S_{ij}S_{ij}}\ , \tag{2.68}$$

where l_s is the characteristic length scale, C_s is Smagorinsky constant and S_{ij} is the magnitude of the large scale strain-rate tensor and determined by

$$S_{ij} = \frac{1}{2}\left(\frac{\partial\tilde{u}_i}{\partial x_j} + \frac{\partial\tilde{u}_j}{\partial x_i}\right). \tag{2.69}$$

The equations (2.62) and (2.67) are the modified continuity and N-S equations used as the LES for turbulent flows. The finer the grid size, the less the unresolved scale eddies.

Similarly, the shallow water equations including the SGS model [3] can be derived as

$$\frac{\partial h}{\partial t} + \frac{\partial(h\tilde{u}_j)}{\partial x_j} = 0 \tag{2.70}$$

$$\frac{\partial(h\tilde{u}_i)}{\partial t} + \frac{\partial(h\tilde{u}_i\tilde{u}_j)}{\partial x_j} = -g\frac{\partial}{\partial x_i}\left(\frac{h^2}{2}\right) + (\nu + \nu_e)\frac{\partial^2(h\tilde{u}_i)}{\partial x_j\partial x_j} + F_i. \tag{2.71}$$

where $\tilde{u}_i$ is the depth-averaged space-filtered velocity component, τ_{ij} is the depth-averaged subgrid-scale stress with eddy viscosity and is expressed by

$$\tau_{ij} = -\nu_e\left(\frac{\partial(h\tilde{u}_i)}{\partial x_j} + \frac{\partial(h\tilde{u}_j)}{\partial x_i}\right), \tag{2.72}$$

The eddy viscosity ν_e takes the same form as Eq. (2.68), but the S_{ij} is represented by

$$S_{ij} = \frac{1}{2h}\left(\frac{\partial(h\tilde{u}_i)}{\partial x_j} + \frac{\partial(h\tilde{u}_j)}{\partial x_i}\right). \tag{2.73}$$

Chapter 3: Lattice Boltzmann Method

3.1 Introduction

Lattice Boltzmann method is a modern method evolving from the lattice gas cellular automata (LGCA) which was developed more than twenty years ago. It has become a popular method in various areas. The lattice Boltzmann method consists of two steps: collision and advection. It avoids the disadvantage of LGCA such as the lack of Galilean invariance (Galilean invariance means that the fundamental laws of physics are the same in all inertial frame), and statistical noise.

3.2 Derivation of the Lattice Boltzmann Equation

The lattice Boltzmann equation is not only evolved from the lattice gas automata, but can also be derived from the continuum Boltzmann equation [120, 121] as shown in the following.

The Boltzmann equation with BGK collision operator reads [69],

$$\frac{\partial f}{\partial t} + \boldsymbol{e}.\nabla f = -\frac{1}{\lambda}(f - f^{eq}) \tag{3.1}$$

in which, $f = f(\boldsymbol{x}, \boldsymbol{e}, t)$ is the single-particle distribution in continuum phase space, $\boldsymbol{e}$ is the particle velocity, λ is a relaxation time, $\nabla = i\frac{\partial}{\partial x} + j\frac{\partial}{\partial y}$ is the gradient operator and f^{eq} is the Maxwell-Boltzmann equilibrium distribution function expressed as

$$f^{eq} = \frac{\rho}{(2\pi/3)^{D/2}} exp\left[-\frac{3}{2}(\boldsymbol{e} - \boldsymbol{V})^2\right] \tag{3.2}$$

where D is the spatial dimension, $\boldsymbol{e}$ is particle velocity and $\boldsymbol{V}$ is fluid velocity; $\boldsymbol{e}$ and $\boldsymbol{V}$ are normalised by $\sqrt{3RT_c}$ (R is the ideal gas constant and T_c is the temperature), which leads to a sound speed of $U_s = 1/\sqrt{3}$ [44]. The fluid density and velocity are computed as follows:

$$\rho = \int f d\boldsymbol{e}, \qquad \rho V = \int \boldsymbol{e} f d\boldsymbol{e} \tag{3.3}$$

If the fluid velocity $\boldsymbol{V}$ is relative small compared with the sound speed, the equilibrium distribution function defined by Eq. (3.2) can be expanded up to the second-order accuracy [122] as follows:

$$f^{eq} = \frac{\rho}{(2\pi/3)^{D/2}} exp\left(-\frac{3}{2}e^2\right)\left[1 + 3(e.V) + \frac{9}{2}(e.V)^2 - \frac{3}{2}V.V\right] \tag{3.4}$$

For the purpose of developing a discrete model, a limited number of particle velocities are adopted $e_\alpha(\alpha = 1, \dots, K)$, and the distribution function including these velocities can be changed to

$$f_\alpha(x,t) = f(x, e_\alpha, t),\ f_\alpha^{eq}(x,t) = f^{eq}(x, e_\alpha, t) \tag{3.5}$$

which satisfies Eq. (3.1),

$$\frac{\partial f_\alpha}{\partial t} + e_\alpha.\nabla f_\alpha = -\frac{1}{\lambda}\left(f_\alpha - f_\alpha^{eq}\right) \tag{3.6}$$

In the limited discrete space and time, the left hand side of Eq. (3.6) is the Lagrangian time derivative and can be discretized as

$$\frac{\partial f_\alpha}{\partial t} + e_\alpha.\nabla f_\alpha = \frac{f_\alpha(x,t+\Delta t) - f_\alpha(x,t)}{\Delta t} + e_{\alpha x}\frac{f_\alpha(x+\Delta x,t+\Delta t) - f_\alpha(x,t+\Delta t)}{\Delta x} \tag{3.7}$$

$$\frac{f_\alpha(x,t+\Delta t) - f_\alpha(x,t)}{\Delta t} + e_{\alpha x}\frac{f_\alpha(x+\Delta x,t+\Delta t) - f_\alpha(x,t+\Delta t)}{\Delta x} = -\frac{1}{\lambda}\left(f_\alpha - f_\alpha^{eq}\right) \tag{3.8}$$

in which $e_{\alpha x}$ can be defined by $e_{\alpha x} = \Delta x/\Delta t$. Combining the above equation with Eq. (3.6) produces the standard lattice Boltzmann equation,

$$f_\alpha(x + e_\alpha\Delta t, t + \Delta t) - f_\alpha(x,t) = -\frac{1}{\tau}\left(f_\alpha - f_\alpha^{eq}\right), \tag{3.9}$$

where $\tau = \lambda/\Delta t$. In fact, τ should be a single dimensionless relaxation time.

3.3 Lattice Boltzmann Equation

The governing equation which is generally valid for fluid flows including the shallow water flows [3] in LBM is as follows:

$$f_\alpha(x + e_\alpha\Delta t, t + \Delta t) = f_\alpha(x,t) + \Omega_\alpha[f(x,t)] + \frac{\Delta t}{N_\alpha e^2}e_{\alpha i}F_i(x,t), \tag{3.10}$$

$N_\alpha$is a constant and is determined by the lattice pattern as

$$N_\alpha = \frac{1}{e^2}\sum_\alpha e_{\alpha i}e_{\alpha i}. \tag{3.11}$$

Ω_α is the collision operator which represents the rate of change of f_α during collision. Theoretically, Ω_α is a complex matrix and is determined by the microscopic dynamics. An idea to linearize the collision operator is given firstly by Higuera and Jimenez [68]. Based on this idea, Ω_α can be expanded about its equilibrium value [123] as follows:

$$\Omega_\alpha(f) = \Omega_\alpha(f^{eq}) + \frac{\partial \Omega_\alpha(f^{eq})}{\partial f_\beta}\left(f_\beta - f_\beta^{eq}\right) + O\left[\left(f_\beta - f_\beta^{eq}\right)^2\right]. \tag{3.12}$$

The solution process of the lattice Boltzmann equation is characterized by $f_\beta \to f_\beta^{eq}$, indicating $\Omega_\alpha(f^{eq}) \approx 0$. Furthermore, if the higher-order terms in Eq. (3.12) are neglected, a linearized collision operator can be obtained,

$$\Omega_\alpha(f) \approx \frac{\partial \Omega_\alpha(f^{eq})}{\partial f_\beta}\left(f_\beta - f_\beta^{eq}\right). \tag{3.13}$$

The Bhatnagar-Gross-Krook (BGK) scheme simplifies the lattice Boltzmann equation greatly and makes the LBM used widely in various sectors. If the local particle distribution is assumed to be relaxed to an equilibrium state at a single rate τ [70, 71],

$$\frac{\partial \Omega_\alpha(f^{eq})}{\partial f_\beta} = -\frac{1}{\tau}\delta_{\alpha\beta}, \tag{3.14}$$

in which $\delta_{\alpha\beta}$ is the Kronecker delta function,

$$\delta_{\alpha\beta} = \begin{cases} 0, \alpha \neq \beta, \\ 1, \alpha = \beta. \end{cases} \tag{3.15}$$

Eq. (3.13) can be rearranged as

$$\Omega_\alpha(f) = -\frac{1}{\tau}\delta_{\alpha\beta}\left(f_\beta - f_\beta^{eq}\right), \tag{3.16}$$

Leading to the lattice BGK collision operator [69],

$$\Omega_\alpha(f) = -\frac{1}{\tau}\left(f_\alpha - f_\alpha^{eq}\right), \tag{3.17}$$

in which τ is named as the single relaxation time. Because the BGK simplifies the lattice Boltzmann equation extremely and increases efficiency; it is widely used in lattice Boltzmann model. Combing the equations (3.10) and (3.17), the following lattice Boltzmann equation can be obtained,

$$f_\alpha(x + e_\alpha \Delta t, t + \Delta t) - f_\alpha(x, t) = \frac{1}{\tau}\left(f_\alpha - f_\alpha^{eq}\right) + \frac{\Delta t}{N_\alpha e^2} e_{\alpha i} F_i(x, t), \tag{3.18}$$

The above equation becomes the most popular form of the lattice Boltzmann equation used today.

3.4 Lattice Pattern

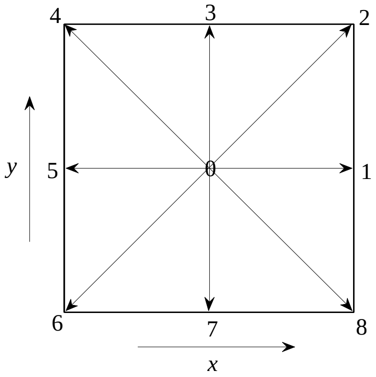

Figure 3.1 9-speed square lattice (D2Q9) in the horizontal plane.

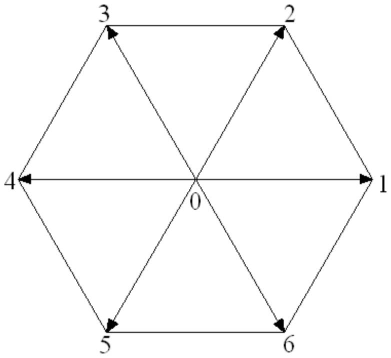

Figure 3.2 7-speed square lattice (D2Q7) in the horizontal plane.

As in traditional methods, a lattice pattern is needed to represent the grid points and discrete computational domain. Furthermore, the lattice pattern has been used to determine particles' motions in the LBM, in which a microscopic model for molecular dynamics has been defined. Besides, the constant N_α in Eq. (3.10) is decided by the lattice pattern.

Generally, there are two kinds of lattice patterns: square lattice and hexagonal lattice for 2D cases which are shown in Figs. 3.1 and 3.2, respectively. The square lattice can have 4-speed, 5-speed, 8-speed, or 9-speed, and the hexagonal lattice can have 6-speed and 7-speed model according to the number of particle speed at lattice node. However, not all of these models can recover the correct flow equations and that requires sufficient lattice symmetry [65]. Studies show that both of 9-speed square lattice and 7-speed hexagonal lattice have such property and can give satisfactory performance in numerical simulations. Therefore, these two kinds of lattice patterns have been used widely in the LBM.

However, the studies indicate that the 9-speed square lattice usually can produce more accurate result than that from the hexagonal lattice [124]. Furthermore, the use of the square lattice leads to an easy way to implement different boundary conditions [125]. Consequently, the 9-speed square lattice is adopted in this thesis.

For the 9-speed square lattice displayed in Fig. 3.1, each particle moves one lattice unit at its velocity along one of the eight links indicated with 1-8 and 0 indicates the rest particle with zero speed. The velocity vector of particles is given by

$$e_\alpha = \begin{cases} (0,0), & \alpha = 0, \\ e\left[cos\frac{(\alpha-1)\pi}{4}, sin\frac{(\alpha-1)\pi}{4}\right], & \alpha = 1,3,5,7, \\ \sqrt{2}e\left[cos\frac{(\alpha-1)\pi}{4}, sin\frac{(\alpha-1)\pi}{4}\right], & \alpha = 2,4,6,8. \end{cases} \tag{3.19}$$

It is not difficult to demonstrate that D2Q9 has the following features,

$$\sum_\alpha e_{\alpha i} = \sum_\alpha e_{\alpha i} e_{\alpha j} e_{\alpha k} = 0, \tag{3.20}$$

$$\sum_\alpha e_{\alpha i} e_{\alpha j} = 6e^2 \delta_{ij}, \tag{3.21}$$

$$\sum_\alpha e_{\alpha i} e_{\alpha j} e_{\alpha k} e_{\alpha l} = 4e^4\left(\delta_{ij}\delta_{kl} + \delta_{ik}\delta_{jl} + \delta_{il}\delta_{jk}\right) - 6e^4 \Delta_{ijkl}, \tag{3.22}$$

where $\Delta_{ijkl} = \begin{cases} 1, & \text{if } i = j = k = l \\ 0, & \text{otherwise'} \end{cases}$

Substituting the Eq. (3.19) into the Eq. (3.11) and the following equation can be obtained:

$$N_\alpha = \frac{1}{e^2}\sum_\alpha e_{\alpha x} e_{\alpha x} = \frac{1}{e^2}\sum_\alpha e_{\alpha y} e_{\alpha y} = 6. \tag{3.23}$$

Combining the equation (3.23) with the equation (3.18), the following equation can be obtained:

$$f_\alpha(x + e_\alpha \Delta t, t + \Delta t) - f_\alpha(x,t) = \frac{1}{\tau}\left(f_\alpha - f_\alpha^{eq}\right) + \frac{\Delta t}{6e^2} e_{\alpha i} F_i(x,t), \tag{3.24}$$

The equation (3.24) is the most common form of a lattice Boltzmann model with D2Q9.

3.5 Local Equilibrium Distribution Function

Deciding a suitable local equilibrium function plays an important role in the lattice Boltzmann method as it decides what flow equations could be solved. In order to apply the equation (3.24) to solve the 2D shallow water equations (2.53) and (2.54), a suitable local equilibrium function f_α^{eq} must be derived.

According to the lattice gas automata, an equilibrium function is the Maxwell-Boltzmann equilibrium distribution function which is often expanded using a Taylor series in macroscopic velocity to its second order [44, 120]. The Navier-Stokes equations can be recovered by using such equilibrium function in the lattice Boltzmann equations [44]. However, the shallow water equations cannot be recovered with this kind of method. On the other hand, an alternative method is to assume that an equilibrium function can be expressed as a power series in macroscopic velocity [126] which has been used successfully in [127, 128] and show its accuracy and suitability [3], and thus it has been adopted here. The equilibrium function can be expressed as

$$f_\alpha^{eq} = A_\alpha + B_\alpha e_{\alpha i} u_i + C_\alpha e_{\alpha i} e_{\alpha j} u_i u_j + D_\alpha u_i u_i. \tag{3.25}$$

Because the equilibrium function has the same symmetry as the lattice shown in Figure 3.1, there are

$$A_1 = A_3 = A_5 = A_7 = \bar{A}\,, A_2 = A_4 = A_6 = A_8 = \tilde{A} \tag{3.26}$$

and the similar expressions for B_α, C_α, and $D_\alpha$are used. Therefore, Eq. (3.25) can be rewritten as,

$$f_\alpha^{eq} = \begin{cases} A_0 + D_0 u_i u_i, & \alpha = 0, \\ \bar{A} + \bar{B} e_{\alpha i} u_i + \bar{C} e_{\alpha i} e_{\alpha j} u_i u_j + \bar{D} u_i u_i, & \alpha = 1,3,5,7, \\ \tilde{A} + \tilde{B} e_{\alpha i} u_i + \tilde{C} e_{\alpha i} e_{\alpha j} u_i u_j + \tilde{D} u_i u_i, & \alpha = 2,4,6,8. \end{cases} \tag{3.27}$$

The coefficients such as A_0, $\bar{A}$ and $\tilde{A}$ can be determined by the constraints on the equilibrium distribution function, for example: mass and momentum conservations. For the shallow water equations, the constraints are the following three conditions:

$$\textstyle\sum_\alpha f_\alpha^{eq}(x,t) = h(x,t), \tag{3.28}$$

$$\textstyle\sum_\alpha e_{\alpha i} f_\alpha^{eq}(x,t) = h(x,t) u_i(x,t)\,, \tag{3.29}$$

$$\textstyle\sum_\alpha e_{\alpha i} e_{\alpha j} f_\alpha^{eq}(x,t) = \frac{1}{2} g h^2(x,t) \delta_{ij} + h(x,t) u_i(x,t) u_j(x,t). \tag{3.30}$$

Basing on the calculated local equilibrium function (3.25) obtained under the above constraints, the 2D shallow water equations (2.53) and (2.54) can be recovered by the lattice Boltzmann equation (3.24) (The proof is shown in section 3.7).

When Eq. (3.27) is substituted into Eq. (3.28), the following equation can be obtained:

$$A_0 + D_0 u_i u_i + 4\bar{A} + \sum_{\alpha=1,3,5,7} \bar{B} e_{\alpha i} u_i + \sum_{\alpha=1,3,5,7} \bar{C}\, e_{\alpha i} e_{\alpha j} u_i u_j + 4\overline{D} u_i u_i + 4\tilde{A} + \sum_{\alpha=2,4,6,8} \tilde{B} e_{\alpha i} u_i + \sum_{\alpha=2,4,6,8} \tilde{C} e_{\alpha i} e_{\alpha j} u_i u_j + 4\widetilde{D} u_i u_i = h. \quad (3.31)$$

Combing the Eq. (3.19) and equating the coefficients of h and $u_i u_i$, respectively, the following equations can be obtained:

$$A_0 + 4\bar{A} + 4\tilde{A} = h, \quad (3.32)$$

$$D_0 + 2e^2\bar{C} + 4e^2\tilde{C} + 4\overline{D} + 4\widetilde{D} = 0. \quad (3.33)$$

Similarly, substituting Eq. (3.27) into Eq. (3.29) results in

$$A_0 e_{\alpha i} + D_0 e_{\alpha i} u_i u_i + \sum_{\alpha=1,3,5,7}\left(\bar{A} e_{\alpha i} + \overline{B} e_{\alpha i} e_{\alpha j} u_j + \bar{C} e_{\alpha i} e_{\alpha j} e_{\alpha k} u_j u_k + \overline{D} e_{\alpha i} u_i u_i\right) + \sum_{\alpha=2,4,6,8}\left(\tilde{A} e_{\alpha i} + \tilde{B} e_{\alpha i} e_{\alpha j} u_j + \tilde{C} e_{\alpha i} e_{\alpha j} e_{\alpha k} u_j u_k + \widetilde{D} e_{\alpha i} u_j u_j\right) = h u_i \quad (3.34)$$

Rearranged the above equation yields

$$2e^2\overline{B} + 4e^2\tilde{B} = h. \quad (3.35)$$

Inserting Eq. (3.27) to Eq. (3.30) leads to

$$A_0 e_{\alpha i} + D_0 e_{\alpha i} u_i u_i + \sum_{\alpha=1,3,5,7}\left(\bar{A} e_{\alpha i} e_{\alpha j} + \bar{B} e_{\alpha i} e_{\alpha j} e_{\alpha k} u_k + \bar{C} e_{\alpha i} e_{\alpha j} e_{\alpha k} e_{\alpha l} u_k u_l + \bar{D} e_{\alpha i} e_{\alpha j} u_k u_k\right) + \sum_{\alpha=2,4,6,8}\left(\tilde{A} e_{\alpha i} e_{\alpha j} + \tilde{B} e_{\alpha i} e_{\alpha j} e_{\alpha k} u_k + \tilde{C} e_{\alpha i} e_{\alpha j} e_{\alpha k} e_{\alpha l} u_k u_l + \tilde{D} e_{\alpha i} e_{\alpha j} u_k u_k\right) = \frac{1}{2} g h^2 \delta_{ij} + h u_i u_j \quad (3.36)$$

Combing Eq. (3.19), the above equation can be expressed by

$$2\bar{A} e^2 \delta_{ij} + 2\bar{C} e^4 u_i u_i + 2\overline{D} e^2 u_i u_i + 4\tilde{A} e^2 \delta_{ij} + 8\tilde{C} e^4 u_i u_j + 4\tilde{C} e^4 u_i u_i + 4\overline{D} e^2 u_i u_i = \frac{1}{2} g h^2 \delta_{ij} + h u_i u_j \quad (3.37)$$

Basing on the above equation, the following four equations can be obtained,

$$2e^2\bar{A} + 4e^2\tilde{A} = \frac{1}{2} g h^2, \quad (3.38)$$

$$8e^4\tilde{C} = h, \quad (3.39)$$

$$2e^4\bar{C} = h\ , \quad (3.40)$$

$$2e^2\overline{D} + 4e^2\widetilde{D} + 4e^4\tilde{C} = 0\ . \quad (3.41)$$

Substituted the Equation (3.39) into the Eq. (3.40), we can get the following equation

$$\bar{C} = 4\tilde{C}. \quad (3.42)$$

Because of the symmetry of lattice and Eq. (3.42), the following relations can be assumed,

$$\bar{A} = 4\tilde{A}\ , \quad (3.43)$$

$$\overline{B} = 4\tilde{B} \quad (3.44)$$

$$\overline{D} = 4\widetilde{D}. \quad (3.45)$$

Combing the Eqs. (3.32), (3.33), (3.35) and (3.38)-(3.45) leads to

$$A_0 = h - \frac{5gh^2}{6e^2}\ , D_0 = -\frac{2h}{3e^2}\ , \quad (3.46)$$

$$\bar{A} = \frac{gh^2}{6e^2}, \bar{B} = \frac{h}{3e^2}, \quad \bar{C} = \frac{h}{2e^4}, \ \bar{D} = -\frac{h}{6e^2} \tag{3.47}$$

$$\tilde{A} = \frac{gh^2}{24e^2}, \ \tilde{B} = \frac{h}{12e^2}, \tilde{C} = \frac{h}{8e^4}, \tilde{D} = -\frac{h}{24e^2} \tag{3.48}$$

Therefore, the local equilibrium function can be expressed by

$$f_\alpha^{eq} = \begin{cases} h - \frac{5gh^2}{6e^2} - \frac{2h}{3e^2} u_i u_i, & \alpha = 0, \\ \frac{gh^2}{6e^2} + \frac{h}{3e^2} e_{\alpha i} u_i + \frac{h}{2e^4} e_{\alpha i} e_{\alpha j} u_i u_j - \frac{h}{6e^2} u_i u_i, & \alpha = 1,3,5,7, \\ \frac{gh^2}{24e^2} + \frac{h}{12e^2} e_{\alpha i} u_i + \frac{h}{8e^4} e_{\alpha i} e_{\alpha j} u_i u_j - \frac{h}{24e^2} u_i u_i, & \alpha = 2,4,6,8. \end{cases} \tag{3.49}$$

With this local equilibrium function, the shallow water equations (2.53) and (2.54) can be recovered correctly as shown in the later section.

3.6 Macroscopic Properties

The above sections have shown the lattice Boltzmann model for shallow water equations proposed by Zhou [129]. In order to recover the shallow water equation, the link between microdynamic variables and macroscopic the physical quantities (such as the water depth h and velocity u_i) will be established in this section. The macroscopic properties of the lattice Boltzmann equation (3.24) has been examined by Zhou [3].

The sum of the zeroth moment of the distribution function in Eq. (3.24) is shown by

$$\sum_\alpha [f_\alpha(x + e_\alpha \Delta t, t + \Delta t) - f_\alpha(x,t)] = -\frac{1}{\tau} \sum_\alpha (f_\alpha - f_\alpha^{eq}) + \frac{\Delta t}{6e^2} \sum_\alpha e_{\alpha i} F_i \tag{3.50}$$

It is easy to demonstrate $\sum_\alpha e_{\alpha i} F_i = 0$, and Eq. (3.50) can be simplified as

$$\sum_\alpha [f_\alpha(x + e_\alpha \Delta t, t + \Delta t) - f_\alpha(x,t)] = -\frac{1}{\tau} \sum_\alpha (f_\alpha - f_\alpha^{eq}). \tag{3.51}$$

The cumulative mass and momentum, are the corresponding summations of the microdynamic mass and momentum which are conserved in lattice Boltzmann method, should also meet the requirement of mass conservation. The continuity equation with microdynamic variables can be expressed by

$$\sum_\alpha f_\alpha(x + e_\alpha \Delta t, t + \Delta t) \equiv \sum_\alpha f_\alpha(x,t) \tag{3.52}$$

Substituting the above equation into Eq. (3.51) results in

$$\sum_\alpha f_\alpha(x,t) = \sum_\alpha f_\alpha^{eq}(x,t) \tag{3.53}$$

Combing Eq. (3.28) with the above expression, the water depth can be obtained as

$$h(x,t) = \sum_\alpha f_\alpha(x,t) \tag{3.54}$$

Next, the velocity will be defined.

Similarly, the sum of the first moment of distribution function in Eq. (3.24) is taken

$$\sum_{\alpha} e_{\alpha i}\left[f_{\alpha}\left(x+e_{\alpha}\Delta t, t+\Delta t\right)-f_{\alpha}\left(x,t\right)\right]=-\frac{1}{\tau}\sum_{\alpha} e_{\alpha i}\left(f_{\alpha}-f_{\alpha}^{eq}\right)+\frac{\Delta t}{6e^{2}}\sum_{\alpha} e_{\alpha i}e_{\alpha j}F_{i}\left(x,t\right) \quad (3.55)$$

Combing with Eq. (3.21), the above equation can be expressed

$$\sum_{\alpha} e_{\alpha i}[f_{\alpha}(x+e_{\alpha}\Delta t, t+\Delta t)-f_{\alpha}(x,t)] = F_i\Delta t - \frac{1}{\tau}\sum_{\alpha} e_{\alpha i}\left(f_{\alpha}-f_{\alpha}^{eq}\right) \quad (3.56)$$

According to the Newton's second law, the momentum equation with microdynamic variables requires

$$\sum_{\alpha} e_{\alpha i}[f_{\alpha}(x+e_{\alpha}\Delta t, t+\Delta t)-f_{\alpha}(x,t)] \equiv F_i\Delta t \quad (3.57)$$

Substituting Eq. (3.57) into Eq. (3.56) leads to

$$\sum_{\alpha} e_{\alpha i}f_{\alpha}(x,t) = \sum_{\alpha} e_{\alpha i}f_{\alpha}^{eq}(x,t). \quad (3.58)$$

Combing Eq. (3.29) with above equation, the velocity u_i can be defined as

$$u_i(x,t) = \frac{1}{h(x,t)}\sum_{\alpha} e_{\alpha i}f_{\alpha}(x,t) \quad (3.59)$$

It should be noted that the distribution function f_{α} relaxes to its local equilibrium function f_{α}^{eq} by the lattice Boltzmann equation (3.24). Besides, the decided water depth and velocity will make sure that both Eqs. (3.53) and (3.58) keep true and the same is true for Eqs. (3.52) and (3.57). Therefore, the lattice Boltzmann method is conservative and accurate.

3.7 Recovery of the Shallow Water Equations

For the purpose of demonstrating that the depth and velocities obtained from Eqs. (3.54) and (3.59) are the solution to the shallow water equations, the lattice Boltzmann equation (3.24) will recover the shallow water equations [3], in which the Chapman-Enskog expansion and Taylor expansion are used.

If Δt is assumed to be small and is equal to ε,

$$\Delta t = \varepsilon \quad (3.60)$$

The equation (3.24) can be expressed by

$$f_{\alpha}(x+e_{\alpha}\varepsilon, t+\varepsilon) - f_{\alpha}(x,t) = \frac{1}{\tau}\left(f_{\alpha}-f_{\alpha}^{eq}\right) + \frac{\varepsilon}{6e^2}e_{\alpha j}F_j \quad (3.61)$$

A Taylor expansion is applied to the first term on the left-hand side of Eq. (3.61) in time and space around point (*x*, *t*) and results in

$$\varepsilon\left(\frac{\partial}{\partial t}+e_{\alpha j}\frac{\partial}{\partial x_j}\right)f_{\alpha} + \frac{1}{2}\varepsilon^2\left(\frac{\partial}{\partial t}+e_{\alpha j}\frac{\partial}{\partial x_j}\right)^2 f_{\alpha} + O(\varepsilon^2) = -\frac{1}{\tau}\left(f_{\alpha}-f_{\alpha}^{(0)}\right) + \frac{\varepsilon}{6e^2}e_{\alpha j}F_j$$

(3.62)

in which $f_\alpha^{(0)} = f_\alpha^{(eq)}$ and f_α can be expanded around $f_\alpha^{(0)}$,

$$f_\alpha = f_\alpha^{(0)} + \varepsilon f_\alpha^{(1)} + \varepsilon^2 f_\alpha^{(2)} + O(\varepsilon^2) \tag{3.63}$$

Inserting Eq. (3.63) into Eq. (3.62) and ignoring the high order term (higher than second order), the equations to order ε and ε^2 can be obtained, respectively,

$$\left(\frac{\partial}{\partial t} + e_{\alpha j}\frac{\partial}{\partial x_j}\right) f_\alpha^{(0)} = -\frac{1}{\tau} f_\alpha^{(1)} + \frac{1}{6e^2} e_{\alpha j} F_j. \tag{3.64}$$

$$\left(\frac{\partial}{\partial t} + e_{\alpha j}\frac{\partial}{\partial x_j}\right) f_\alpha^{(1)} + \frac{1}{2}\left(\frac{\partial}{\partial t} + e_{\alpha j}\frac{\partial}{\partial x_j}\right)^2 f_\alpha^{(0)} = -\frac{1}{\tau} f_\alpha^{(2)}. \tag{3.65}$$

Substituting Eq. (3.64) into Eq. (3.65) and rearranging lead to

$$\left(1 - \frac{1}{2\tau}\right)\left(\frac{\partial}{\partial t} + e_{\alpha j}\frac{\partial}{\partial x_j}\right) f_\alpha^{(1)} = -\frac{1}{\tau} f_\alpha^{(2)} - \frac{1}{2}\left(\frac{\partial}{\partial t} + e_{\alpha j}\frac{\partial}{\partial x_j}\right)\left(\frac{1}{6e^2} e_{\alpha k} F_k\right) \tag{3.66}$$

From $\sum[(3.64) + \varepsilon \times (3.66)])$ about α, the following equation can be derived:

$$\frac{\partial}{\partial t}\left(\sum_\alpha f_\alpha^{(0)}\right) + \frac{\partial}{\partial x_j}\left(\sum_\alpha e_{\alpha j} f_\alpha^0\right) = -\varepsilon \frac{1}{12e^2}\frac{\partial}{\partial x_j}\left(\sum_\alpha e_{\alpha j} e_{\alpha k} F_k\right) \tag{3.67}$$

If the force term with the first-order accuracy is applied, combining Eqs. (3.19) and (3.49) with above equation leads to

$$\frac{\partial h}{\partial t} + \frac{\partial (h u_j)}{\partial x_j} = 0 \tag{3.68}$$

which is just the continuity equation (2.53) for shallow water flow.

Taking $\sum e_{\alpha i}[(3.64) + \varepsilon \times (3.66)]$ about α can result in

$$\frac{\partial}{\partial t}\left(\sum_\alpha e_{\alpha i} f_\alpha^{(0)}\right) + \frac{\partial}{\partial x_j}\left(\sum_\alpha e_{\alpha i} e_{\alpha j} f_\alpha^{(0)}\right) + \varepsilon\left(1 - \frac{1}{2\tau}\right)\frac{\partial}{\partial x_j}\left(\sum_\alpha e_{\alpha i} e_{\alpha j} f_\alpha^{(1)}\right) = F_j \delta_{ij} - \varepsilon \frac{1}{2}\sum_\alpha e_{\alpha i}\left(\frac{\partial}{\partial t} + e_{\alpha j}\frac{\partial}{\partial x_j}\right)\left(\frac{1}{6e^2} e_{\alpha j} F_j\right) \tag{3.69}$$

Similarly, if the force term with the first-order accuracy is used, combining it with Eqs. (3.19) and (3.49), the above equation can be rearranged as:

$$\frac{\partial (h u_i)}{\partial t} + \frac{\partial (h u_i u_j)}{\partial x_j} = -g\frac{\partial}{\partial x_i}\left(\frac{h^2}{2}\right) - \frac{\partial}{\partial x_j}\Lambda_{\mathrm{ij}} + F_i \, , \tag{3.70}$$

in which

$$\Lambda_{ij} = \frac{\varepsilon}{2\tau}(2\tau - 1)\sum_\alpha e_{\alpha i} e_{\alpha j} f_\alpha^{(1)}. \tag{3.71}$$

Combining Eqs. (3.64), (3.19) and (3.49) and making some algebra, the following expression can be obtained:

$$\Lambda_{ij} \approx -\nu\left[\frac{\partial (h u_i)}{\partial x_j} + \frac{\partial (h u_j)}{\partial x_i}\right]. \tag{3.72}$$

Substituting Eq. (3.72) into Eq. (3.70) results in

$$\frac{\partial(hu_i)}{\partial t} + \frac{\partial(hu_iu_j)}{\partial x_j} = -g\frac{\partial}{\partial x_i}\left(\frac{h^2}{2}\right) + \nu\frac{\partial^2(hu_i)}{\partial x_j x_j} + F_i, \tag{3.73}$$

where the kinematic viscosity ν is defined by

$$\nu = \frac{e^2\Delta t}{6}(2\tau - 1) \tag{3.74}$$

And the force term F_i by

$$F_i = -gh\frac{\partial z_b}{\partial x_i} + \frac{\tau_{wi}}{\rho} - \frac{\tau_{bi}}{\rho} + E_i\ . \tag{3.75}$$

Equation (3.73) is the momentum equation for the shallow flows.

Zhou [3] has pointed out that the lattice Boltzmann equation (3.24) is only first-order accurate for the recovered shallow water equations as shown above. However, it has also been proved that Eq. (3.24) can become the second-order accurate if a suitable force term is used (the process will be shown in section 3.9) [3].

3.8 Stability Conditions

The lattice Boltzmann equation can be interpreted as a Lagrangian finite difference method [130]. Therefore, it is not surprising that it may suffer from numerical instability. Sterling and Chen [130] carried out an analysis of the stability for the lattice Boltzmann method using perturbations method. In general, the stability conditions are not available for the method. However, Zhou [3] indicated the LABSWE is stable if some basic requirements are met:

First is the fluid resistance. It indicates that the kinematic viscosity ν should be positive [130]. With Eq. (3.74), the following expression can be obtained:

$$\nu = \frac{e^2\Delta t}{6}(2\tau - 1) > 0. \tag{3.76}$$

Thus, the relaxation time needs to meet:

$$\tau > \frac{1}{2}. \tag{3.77}$$

Secondly, as indicated by Zhou [3] and Liu [93], the Courant number should be smaller than unity. It implies that the magnitude of the resultant macro velocity is smaller than the lattice speed,

$$\frac{u_ju_j}{e^2} < 1, \tag{3.78}$$

and the wave velocity also should be smaller than the lattice speed:

$$\frac{gh}{e^2} < 1, \tag{3.79}$$

Up to now, LABSWE is limited to subcritical shallow water flows, it means:

$$\frac{u_j u_j}{gh} < 1, \tag{3.80}$$

Meanwhile, the Froude number should smaller than unit

$$F_r = \frac{\sqrt{u_j u_j}}{\sqrt{gh}} < 1 \ , \tag{3.81}$$

It should be noted that the first three conditions (3.77)-(3.79) can be easily satisfied by adjusting the relaxation time τ, the lattice size Δx and time step Δt. It has been tested that the lattice Boltzmann method is stable normally, if these four stability conditions can be satisfied [3].

3.9 Force Terms

3.9.1 Centred Scheme

Practical flows always involve internal or external forces, such as a tidal flow, dam-breaking flows, multiphase flows and multicomponent fluids. A suitable expression for force is critical to predict the real flows accurately. Many researchers have pursued this topic. Martys et al. [131] presented a force term with Hermite expansion and the scheme is complicated. Buick and Greated [132] proposed a composite scheme for the gravity. Guo et al. [133] improved the local equilibrium distribution function by including the force term.

Zhou [125, 129] incorporated the force terms into the streaming step directly in the lattice Boltzmann method and obtained accurate results for many flows. After that, Zhou [3] improved the method with a second-order force scheme and showed satisfactory results. This scheme has been adopted in this thesis.

For the centred scheme, the force term is determined at the mid-point between the lattice point and its neighbouring lattice point as

$$F_i = F_i\left(x + \frac{1}{2} e_\alpha \Delta t, t + \frac{1}{2} \Delta t\right) \tag{3.82}$$

In order to be easy for parallel computation, the above equation can be expressed in semi-implicit form:

$$F_i = F_i\left(x + \tfrac{1}{2}e_\alpha \Delta t, t\right), \tag{3.83}$$

Next, the Chapman-Enskog procedure is applied to lattice Boltzmann equation (3.24) to study the accuracy of this scheme. With the centred scheme for the force term, if Δt is assumed to be small and equal to ε, the equation (3.24) can be written as

$$f_\alpha\left(x+e_\alpha\varepsilon, t+\varepsilon\right)-f_\alpha\left(x,t\right)=-\frac{1}{\tau}\left[f_\alpha\left(x,t\right)-f_\alpha^{eq}\left(x,t\right)\right]+\frac{\varepsilon}{6e^2}e_{\alpha i}F_i\left(x+\frac{1}{2}e_\alpha\varepsilon,t+\frac{1}{2}\varepsilon\right) \tag{3.84}$$

A Taylor expansion is applied to the first term on the left-hand side of the above equation in time and space around point (x, t) and the force term on the right-hand side,

$$f_\alpha\left(x+e_\alpha\varepsilon,t+\varepsilon\right)=f_\alpha\left(x,t\right)+\varepsilon\left(\frac{\partial}{\partial t}+e_{\alpha j}\frac{\partial}{\partial x_j}\right)f_\alpha+\frac{1}{2}\varepsilon^2\left(\frac{\partial}{\partial t}+e_{\alpha j}\frac{\partial}{\partial x_j}\right)^2 f_\alpha+O\left(\varepsilon^2\right) \tag{3.85}$$

$$F_i\left(x+\tfrac{1}{2}e_\alpha\varepsilon, t+\varepsilon\right) = F_i(x,t)+\tfrac{1}{2}\varepsilon\left(\frac{\partial}{\partial t}+e_{\alpha j}\frac{\partial}{\partial x_j}\right)F_i(x,t)+O(\varepsilon). \tag{3.86}$$

Substituting Eqs. (3.85) and (3.86) into Eq. (3.84) results in

$$\varepsilon\left(\frac{\partial}{\partial t}+e_{\alpha j}\frac{\partial}{\partial x_j}\right)f_\alpha+\frac{1}{2}\varepsilon^2\left(\frac{\partial}{\partial t}+e_{\alpha j}\frac{\partial}{\partial x_j}\right)^2 f_\alpha = -\frac{1}{\tau}\left(f_\alpha - f_\alpha^{(0)}\right)+\frac{\varepsilon}{6e^2}e_{\alpha i}F_i + \frac{\varepsilon^2}{12e^2}\left(\frac{\partial}{\partial t}+e_{\alpha j}\frac{\partial}{\partial x_j}\right)e_{\alpha i}F_i + O(\varepsilon^2). \tag{3.87}$$

in which, $f_\alpha^{(0)} = f_\alpha^{eq}$ and expanding f_α to $f_\alpha^{(0)}$ gives,

$$f_\alpha = f_\alpha^{(0)}+\varepsilon f_\alpha^{(1)}+\varepsilon^2 f_\alpha^{(2)}+O(\varepsilon^2), \tag{3.88}$$

Taking the equation (3.87) to order ε and ε^2 leads to

$$\left(\frac{\partial}{\partial t}+e_{\alpha j}\frac{\partial}{\partial x_j}\right)f_\alpha^{(0)} = -\frac{1}{\tau}f_\alpha^{(1)}+\frac{1}{6e^2}e_{\alpha i}F_i\,, \tag{3.89}$$

$$\left(\frac{\partial}{\partial t}+e_{\alpha j}\frac{\partial}{\partial x_j}\right)f_\alpha^{(1)}+\frac{1}{2}\left(\frac{\partial}{\partial t}+e_{\alpha j}\frac{\partial}{\partial x_j}\right)^2 f_\alpha^{(0)} = -\frac{1}{\tau}f_\alpha^{(2)}+\frac{1}{12e^2}\left(\frac{\partial}{\partial t}+e_{\alpha j}\frac{\partial}{\partial x_j}\right)e_{\alpha j}F_i \tag{3.90}$$

Substituting Eq. (3.89) into Eq. (3.90) leads to

$$\left(1-\frac{1}{2\tau}\right)\left(\frac{\partial}{\partial t}+e_{\alpha j}\frac{\partial}{\partial x_j}\right)f_\alpha^{(1)} = -\frac{1}{\tau}f_\alpha^{(2)} \tag{3.91}$$

From ($\sum[(3.89)+\varepsilon\times(3.91)]$) about α, the following equation can be derived:

$$\frac{\partial}{\partial t}\left(\sum\nolimits_\alpha f_\alpha^{(0)}\right)+\frac{\partial}{\partial x_j}\left(\sum\nolimits_\alpha e_{\alpha j}f_\alpha^{(0)}\right)=0. \tag{3.92}$$

Combining Eqs. (3.19) and (3.49) with the above equation gives the second-order accurate continuity equation (2.53). It can be noted that the assumption of first-order accuracy for the force term is not necessary as that in Equation (3.67).

Taking $(\sum e_{\alpha i}[(3.89) + \varepsilon \times (3.91)])$ about α results in

$$\frac{\partial}{\partial t}\left(\sum_\alpha e_{\alpha i} f_\alpha^{(0)}\right) + \frac{\partial}{\partial x_j}\left(\sum_\alpha e_{\alpha i} e_{\alpha j} f_\alpha^{(0)}\right) + \varepsilon\left(1 - \frac{1}{2\tau}\right)\frac{\partial}{\partial x_j}\left(\sum_\alpha e_{\alpha i} e_{\alpha j} f_\alpha^{(1)}\right) = F_i. \quad (3.93)$$

Again combining Eqs. (3.19) and (3.49), the above equation can be written as

$$\frac{\partial(hu_i)}{\partial t} + \frac{\partial(hu_i u_j)}{\partial x_j} = -g\frac{\partial}{\partial x_i}\left(\frac{h^2}{2}\right) - \frac{\partial}{\partial x_j}\Lambda_{ij} + F_i, \quad (3.94)$$

in which

$$\Lambda_{ij} = \frac{\varepsilon}{2\tau}(2\tau - 1)\sum_\alpha e_{\alpha i} e_{\alpha j} f_\alpha^{(1)}. \quad (3.95)$$

Combining Eqs. (3.89), (3.19) and (3.49) and making some algebra, the following expression can be obtained:

$$\Lambda_{ij} \approx -\frac{e^2\varepsilon}{6}(2\tau - 1)\left[\frac{\partial(hu_i)}{\partial x_j} + \frac{\partial(hu_j)}{\partial x_i}\right]. \quad (3.96)$$

Substituting Eq. (3.96) into Eq. (3.94) gives the momentum equation (2.54) at second-order accurate.

Similarly, it can be proved that the use of the second-order scheme (3.83) for the force term in Eq. (3.24) also results in second-order accurate macroscopic equations in space. However, using the basic scheme gives only first-order accurate macroscopic equations in time and space as shown in section 3.7.

3.9.2 Improved Force Term treatment method and New Treatment of Bed Slope

In the above method for the force term, it includes the calculation of the first order derivative related to the bed slope, which can be accurately determined by the centred scheme. To improve the efficiency and remove the calculation of the derivatives, Zhou [134] introduced the bed level into the lattice Boltzmann equation. In this new scheme, the lattice Boltzmann equation (3.24) can be rewritten as

$$f_\alpha(x + e_\alpha \Delta t, t + \Delta t) - f_\alpha(x, t) = \frac{1}{\tau}\left(f_\alpha^{eq} - f_\alpha\right) - \frac{g\bar{h}}{6e^2}\left[z_b(x + e_\alpha \Delta t) - z_b(x)\right] + \frac{\Delta t}{6e^2} e_{\alpha j} F_j \quad (3.97)$$

in which $\bar{h} = 0.5[h(\boldsymbol{x} + \boldsymbol{e}_\alpha \Delta t, t) + h(\boldsymbol{x}, t)]$.

In addition, the calculation of the force term can also be improved for more accurate results. The last force term in Eq. (3.24) can be defined by $\Delta t F_\alpha$ where $F_\alpha = \frac{e_{\alpha i} F_i}{6e^2}$ in [3].

In order to include the effect of direction on the distribution function, the force term can be improved by

$$F_\alpha = 3w_\alpha \frac{e_{ai}F_i}{e^2} \tag{3.98}$$

in which w_α are the weights defined as

$$w_a = \begin{cases} 4/9 & a = 0 \\ 1/9, & a = 1,3,5,7 \\ 1/36, & a = 2,4,6,8 \end{cases} \tag{3.99}$$

The force term in Eq. (3.24) can be calculated using Eq. (98) in which F_i is calculated by the following equation

$$F_i = -\frac{g\bar{h}[z_b(\boldsymbol{x}+\boldsymbol{e}_a\Delta t)-z_b(\boldsymbol{x})]}{e_{ai}\Delta t} - \frac{\tau_{bi}}{\rho} \tag{3.100}$$

3.9.3 Discussion

In section 3.9.1, the implicit form of the centred scheme (3.82) was used to show that the scheme is second-order accurate in space and time. Similarly, it can be proved that the semi-implicit form of centred scheme (3.83) is second-order accurate in space but only first-order accurate in time. In practice, a scheme with first-order accuracy in time can still provide accurate solution for most flow problems. In fact, this has been confirmed in the numerical computations. Therefore, Eqs. (3.83), (3.98)-(3.100) are adopted in this thesis.

3.10 Turbulence Modelling

3.10.1 LABSWE^{TM}

In order to simulate flows with relatively higher Reynolds number, LABSWE is extended to the shallow water equations with turbulence modelling (LABSWE^{TM}) which is proposed by Zhou [3] in this section. Comparing the turbulent shallow water equations (2.70) and (2.71) with the equations (2.53) and (2.54) without flow turbulence, it can be noted that the only difference is the viscosity term. LABSWE^{TM} includes the eddy viscosity term which is not present in the LABSWE. Because the kinematic viscosity ν is determined only by the relaxation time via Eq. (3.74) with constant time step and space step, this means that a new relaxation time τ_t can be defined by

$$\tau_t = \tau + \tau_e, \tag{3.101}$$

which yields a total viscosity ν_t,

$$\nu_t = \nu + \nu_e, \tag{3.102}$$

and the Equation (3.24) can be rewritten as

$$f_\alpha(x + e_\alpha \Delta t, t + \Delta t) - f_\alpha(x, t) = -\frac{1}{\tau_t}\left(f_\alpha - f_\alpha^{eq}\right) + \frac{\Delta t}{6e^2} e_{\alpha i} F_i, \tag{3.103}$$

which can produce the solution to the shallow water equations (2.70) and (2.71). This is consistent with the idea of the lattice Boltzmann model with subgrid-scale stress designed by Hou et al. [135]. Therefore, the flow turbulence can be predicted easily by the standard lattice Boltzmann equation (3.103) with the total relaxation time τ_t.

For the purpose of determining the total relaxation time τ_t, the strain-rate tensor S_{ij} needs to be calculated. As S_{ij} defined by Eq. (2.73) involves calculation of derivatives, it is not suitable or efficient to use in practice. To keep consistent with the lattice gas dynamics, S_{ij} is expected to be expressed in terms of the distribution function. Using the Chapman-Enskog expansion, it can be seen that the strain-rate tensor S_{ij} is related to the non-equilibrium momentum flux tensor (see section 3.10.2 for detail) and S_{ij} can be calculated by

$$S_{ij} = -\frac{3}{2e^2 h \tau_t \Delta t} \sum_\alpha e_{\alpha i} e_{\alpha j}\left(f_\alpha - f_\alpha^{eq}\right). \tag{3.104}$$

Assuming ν_t and τ_t satisfy the relation (3.74), the following expression can be obtained:

$$\tau_t = \frac{1}{2} + \frac{3\nu_t}{e^2 \Delta t}. \tag{3.105}$$

Substituting Eqs. (3.101) and (3.102) into the above equation results in

$$\tau_e + \tau = \frac{1}{2} + \frac{3(\nu_e + \nu)}{e^2 \Delta t}. \tag{3.106}$$

Combined with Eq. (3.74) yields

$$\tau_e = \frac{3}{e^2 \Delta t} \nu_e. \tag{3.107}$$

Substituting Eq. (2.68) into the above equation provides

$$\tau_e = \frac{3}{e^2 \Delta t} (C_s l_s)^2 \sqrt{S_{ij} S_{ij}}. \tag{3.108}$$

Combining Eq. (3.104) with the above equation gives

$$\tau_e = \frac{3}{e^2 \Delta t} (C_s l_s)^2 \frac{3}{2e^2 h \tau_t \Delta t} \sqrt{\Pi_{ij} \Pi_{ij}} \tag{3.109}$$

in which

$$\Pi_{ij} = \sum_\alpha e_{\alpha i} e_{\alpha j}\left(f_\alpha - f_\alpha^{eq}\right). \tag{3.110}$$

With Eq. (3.101), if $l_s = \Delta x$ is adopted, Eq. (3.109) can be rewritten as

$$\tau_e = \frac{9}{2} \frac{C_s^2}{e^2 h (\tau_e + \tau)} \sqrt{\Pi_{ij} \Pi_{ij}}. \tag{3.111}$$

Solving the above equation gives:

$$\tau_e = \frac{-\tau+\sqrt{\tau^2+18C_s^2/(e^2h)\sqrt{\Pi_{ij}\Pi_{ij}}}}{2}, \tag{3.112}$$

With Eq. (3.101), the total relaxation time τ_t can be by

$$\tau_t = \frac{\tau+\sqrt{\tau^2+18C_s^2/(e^2h)\sqrt{\Pi_{ij}\Pi_{ij}}}}{2}. \tag{3.113}$$

3.10.2 Recovery of LABSWE$^{\mathrm{TM}}$

With a similar procedure described in section 3.7, the shallow water equations (2.70) and (2.71) can be recovered from the lattice Boltzmann equation (3.103) by the Chapman-Enskog expansion.

Assuming Δt is small and is equal to ε,

$$\Delta t = \varepsilon. \tag{3.114}$$

The equation (3.103) can be written as

$$f_\alpha(x + e_\alpha\varepsilon, t + \varepsilon) - f_\alpha(x,t) = -\frac{1}{\tau_t}\left(f_\alpha - f_\alpha^{eq}\right) + \frac{\varepsilon}{6e^2}e_{\alpha j}F_j. \tag{3.115}$$

If a Taylor expansion is applied to the first term on the left-hand side of the above equation in time and space around point (*x*, *t*), the following equation can be obtained:

$$\varepsilon\left(\frac{\partial}{\partial t} + e_{\alpha j}\frac{\partial}{\partial x_j}\right)f_\alpha + \frac{1}{2}\varepsilon^2\left(\frac{\partial}{\partial t} + e_{\alpha j}\frac{\partial}{\partial x_j}\right)^2 f_\alpha + O(\varepsilon^2) = -\frac{1}{\tau_t}\left(f_\alpha - f_\alpha^{(0)}\right) + \frac{\varepsilon}{6e^2}e_{\alpha j}F_j \tag{3.116}$$

where $f_\alpha^{(0)} = f_\alpha^{eq}$, f_α can be expanded around $f_\alpha^{(0)}$,

$$f_\alpha = f_\alpha^{(0)} + \varepsilon f_\alpha^{(1)} + \varepsilon^2 f_\alpha^{(2)} + O(\varepsilon^2), \tag{3.117}$$

Substituting Eq. (3.117) into Eq. (3.116), we have the following expressions to order ε and ε^2,

$$\left(\frac{\partial}{\partial t} + e_{\alpha j}\frac{\partial}{\partial x_j}\right)f_\alpha^{(0)} = -\frac{1}{\tau_t}f_\alpha^{(1)} + \frac{1}{6e^2}e_{\alpha j}F_j. \tag{3.118}$$

$$\left(\frac{\partial}{\partial t} + e_{\alpha j}\frac{\partial}{\partial x_j}\right)f_\alpha^{(1)} + \frac{1}{2}\left(\frac{\partial}{\partial t} + e_{\alpha j}\frac{\partial}{\partial x_j}\right)^2 f_\alpha^{(0)} = -\frac{1}{\tau_t}f_\alpha^{(2)}. \tag{3.119}$$

Substituting Eq. (3.118) into Eq. (3.119) results in

$$\left(1 - \frac{1}{2\tau_t}\right)\left(\frac{\partial}{\partial t} + e_{\alpha j}\frac{\partial}{\partial x_j}\right)f_\alpha^{(1)} = -\frac{1}{\tau_t}f_\alpha^{(2)} - \frac{1}{2}\left(\frac{\partial}{\partial t} + e_{\alpha j}\frac{\partial}{\partial x_j}\right)\left(\frac{1}{6e^2}e_{\alpha k}F_k\right). \tag{3.120}$$

From $\sum[(3.118) + \varepsilon \times (3.120)]$ about α, the following equation can be derived:

$$\frac{\partial}{\partial t}\left(\sum_\alpha f_\alpha^{(0)}\right) + \frac{\partial}{\partial x_j}\left(\sum_\alpha e_{\alpha j}f_\alpha^{(0)}\right) = -\varepsilon\frac{1}{12e^2}\frac{\partial}{\partial x_j}\left(\sum_\alpha e_{\alpha j}e_{\alpha k}F_k\right). \tag{3.121}$$

If the force term with the first-order accuracy is applied, combining Eqs. (3.19) and (3.49) with the above equation leads to the continuity equaton (2.70).

Taking $\sum e_{\alpha i}[(3.118) + \varepsilon \times (3.120)]$ about α, the following equation can be obtained

$$\frac{\partial}{\partial t}\left(\sum_\alpha e_{\alpha i} f_\alpha^{(0)}\right) + \frac{\partial}{\partial x_j}\left(\sum_\alpha e_{\alpha i} e_{\alpha j} f_\alpha^{(0)}\right) + \varepsilon\left(1 - \frac{1}{2\tau_t}\right)\frac{\partial}{\partial x_j}\left(\sum_\alpha e_{\alpha i} e_{\alpha j} f_\alpha^{(1)}\right) = F_j \delta_{ij} - \varepsilon \frac{1}{2} \sum_\alpha e_{\alpha i}\left(\frac{\partial}{\partial t} + e_{\alpha j}\frac{\partial}{\partial x_j}\right)\left(\frac{1}{6e^2} e_{\alpha j} F_j\right). \tag{3.122}$$

Similarly, using the force term with the first-order accuracy and referring to Eqs. (3.19) and (3.49), the above equation can be written as

$$\frac{\partial(hu_i)}{\partial t} + \frac{\partial(hu_i u_j)}{\partial x_j} = -g\frac{\partial}{\partial x_i}\left(\frac{h^2}{2}\right) - \frac{\partial}{\partial x_j}\Lambda_{\mathrm{ij}} + F_i, \tag{3.123}$$

in which

$$\Lambda_{ij} = \frac{\varepsilon}{2\tau_t}(2\tau_t - 1)\sum_\alpha e_{\alpha i} e_{\alpha j} f_\alpha^{(1)}. \tag{3.124}$$

Combining Eqs. (3.19), (3.49) and (3.118) with the above equation, one can get

$$\Lambda_{ij} \approx -\frac{\varepsilon}{6} e^2 (2\tau_t - 1)\left[\frac{\partial(hu_i)}{\partial x_j} + \frac{\partial(hu_j)}{\partial x_i}\right]. \tag{3.125}$$

Substituting Eq. (3.125) into Eq. (3.123) leads to a momentum equation,

$$\frac{\partial(hu_i)}{\partial t} + \frac{\partial(hu_i u_j)}{\partial x_j} = -g\frac{\partial}{\partial x_i}\left(\frac{h^2}{2}\right) + \nu_t \frac{\partial^2(hu_i)}{\partial x_j \partial x_j} + F_i, \tag{3.126}$$

in which, the total viscosity ν_t is defined by

$$\nu_t = \frac{e^2 \Delta t}{6}(2\tau_t - 1). \tag{3.127}$$

Combining Eqs. (3.74), (3.101), (3.102) and (3.107) with the above equation, the total viscosity can be expressed by

$$\nu_t = \nu_e + \nu, \tag{3.128}$$

and so Eq. (3.126) is just the momentum equation (2.71).

If the force term with the centred scheme described in section 3.9 is used, the shallow water equations with turbulence at second-order accuracy in time and space can be recovered.

The calculation of the strain-rate tensor S_{ij} can be derived from Eqs. (3.124) and (3.125), Combining the Eqs. (3.124) and (3.125) can lead to

$$\frac{1}{2h}\left[\frac{\partial(hu_i)}{\partial x_j} + \frac{\partial(hu_j)}{\partial x_i}\right] = -\frac{3}{2e^2 h\tau_t}\sum_\alpha e_{\alpha i} e_{\alpha j} f_\alpha^{(1)}. \tag{3.129}$$

With Eq. (3.117), the following can be obtained:

$$f_\alpha^{(1)} = \frac{\left(f_\alpha - f_\alpha^{(0)}\right)}{\varepsilon} + O(\varepsilon) \approx \frac{\left(f_\alpha - f_\alpha^{(0)}\right)}{\varepsilon}. \tag{3.130}$$

Considering $f_\alpha^{(0)} = f_\alpha^{eq}$, $\varepsilon = \Delta t$ and Eq. (2.73), substituting Eq. (3.130) into Eq. (3.129) gives Eq. (3.104) which is used to calculate the strain-rate tensor S_{ij}.

3.11 Multiple-Relaxation Time

Compared with the BGK scheme, the multiple-relaxation-time is less used in the lattice Boltzmann model for shallow water flows. In order to improve the stability of the method, the collision operator of multiple-relaxation-time is incorporated into the LABSWE (named LABSWE$^{\mathrm{MRT}}$) in this section. This model will be used in the latter chapter and show its ability. Together with the new force term introduced in section 3.9.2, the shallow water equations are recovered correctly in this section, which is the first derivation to writer's knowledge.

3.11.1 LABSWE$^{\mathrm{MRT}}$

As described in section 1.5.4, the multiple-relaxation-time can improve the stability of computation. It is incorporated into the LABSWE in this thesis (named LABSWE$^{\mathrm{MRT}}$) and the shallow water equations will be recovered by Chapman-Enskog analysis in the next section. If the D2Q9 model is adopted, the lattice Boltzmann equations with the MRT for shallow water equations are as follows:

$$f_\alpha(\boldsymbol{x} + \boldsymbol{e}_\alpha \Delta t, t + \Delta t) - f_\alpha(x, t) = -(\boldsymbol{T_r}^{-1}\boldsymbol{S})_{\alpha i}\left(m_i(x, t) - m_i^{eq}(x, t)\right) + \Delta t F_\alpha \tag{3.131}$$

where $m = \boldsymbol{T_r} f$, $f = \boldsymbol{T_r}^{-1} m$ and $\boldsymbol{S}$ is the relaxation matrix, $\boldsymbol{S}$=diag (s_0, s_1, s_2, s_3, s_4, s_5, s_6, s_7, s_8), $\boldsymbol{T_r}$ is the transform matrix defined in [85],

$$\boldsymbol{T_r} = \begin{bmatrix} 1 & 1 & 1 & 1 & 1 & 1 & 1 & 1 & 1 \\ -4 & -1 & 2 & -1 & 2 & -1 & 2 & -1 & 2 \\ 4 & -2 & 1 & -2 & 1 & -2 & 1 & -2 & 1 \\ 0 & 1 & 1 & 0 & -1 & -1 & -1 & 0 & 1 \\ 0 & -2 & 1 & 0 & -1 & 2 & -1 & 0 & 1 \\ 0 & 0 & 1 & 1 & 1 & 0 & -1 & -1 & -1 \\ 0 & 0 & 1 & -2 & 1 & 0 & -1 & 2 & -1 \\ 0 & 1 & 0 & -1 & 0 & 1 & 0 & -1 & 0 \\ 0 & 0 & 1 & 0 & -1 & 0 & 1 & 0 & -1 \end{bmatrix} \tag{3.132}$$

The relaxation parameters s_7 and s_8 is chosen according to fluid viscosity determined by Equation (1.11), and the other parameters can be chosen freely during the range of 0~2 for maximum stability. In practical application, these free parameters are a little larger than 1 according to [85].

The equilibrium values of moments m^{eq} is

$$m^{eq}_{(1..9)} = (h, -4h + \frac{3gh^2}{e^2} + \frac{3h\left(u^2+v^2\right)}{e^2}, 4h - \frac{9gh^2}{2e^2} - \frac{3h\left(u^2+v^2\right)}{e^2}, \frac{hu}{e}, -\frac{hu}{e}, \frac{hv}{e}, -\frac{hv}{e}, \frac{h\left(u^2-v^2\right)}{e^2}, \frac{huv}{e^2})^T \quad (3.133)$$

3.11.2 Recovery of the LABSWE$^{\mathrm{MRT}}$

The Chapman-Enskog analysis is used to recover the shallow water equations from the proposed MRT- LBM model with improved force term. Assuming Δt is small and $\Delta t = \varepsilon$, equation (3.131) can be expressed as:

$$f_\alpha(\boldsymbol{x} + \boldsymbol{e}_\alpha \varepsilon, t + \varepsilon) - f_\alpha(x, t) = -(\boldsymbol{T_r}^{-1}\boldsymbol{S})_{\alpha i}\left(m_i(x,t) - m_i^{eq}(x,t)\right) + \varepsilon F_\alpha \qquad (3.134)$$

Take a Taylor expansion to the first term on the left hand side of the above equation in time and space around point ($\boldsymbol{x}$, t) leads to

$$\varepsilon\left(\partial_t + e_{\alpha j}\partial_j\right)f_\alpha + \frac{\varepsilon^2}{2}(\partial_t + e_{\alpha j}\partial_j)^2 f_\alpha + O(\varepsilon^2) = -(\boldsymbol{T_r^{-1}S})_{\alpha i}\left(m_i - m_i^{eq}\right) + \varepsilon F_\alpha \qquad (3.135)$$

According to the Chapman-Enskog expansion, f_α can be written in a series of ε

$$f_\alpha = f_\alpha^{(0)} + \varepsilon f_\alpha^{(1)} + \varepsilon^2 f_\alpha^{(2)} + O(\varepsilon^2), \qquad (3.136)$$

which can be expressed in a vector form,

$$\boldsymbol{f} = \boldsymbol{f}^{(0)} + \varepsilon \boldsymbol{f}^{(1)} + \varepsilon^2 \boldsymbol{f}^{(2)} + O(\varepsilon^2), \qquad (3.137)$$

The above equation can be easily converted into an expression in moment space by being multiplied with $\boldsymbol{T}$,

$$\boldsymbol{m} = \boldsymbol{m}^{(0)} + \varepsilon \boldsymbol{m}^{(1)} + \varepsilon^2 \boldsymbol{m}^{(2)} + O(\varepsilon^2), \qquad (3.138)$$

If the centered scheme[3] is used, the expression for F_α can be obtained

$$F_\alpha = F_\alpha\left(\boldsymbol{x} + \frac{1}{2}\boldsymbol{e}_\alpha \varepsilon, t + \frac{1}{2}\varepsilon\right), \qquad (3.82)$$

Making a Taylor expansion to the above yields

$$F_\alpha\left(\boldsymbol{x} + \frac{1}{2}\boldsymbol{e}_\alpha \varepsilon, t + \frac{1}{2}\varepsilon\right) = F_\alpha(\boldsymbol{x}, t) + \frac{\varepsilon}{2}(\partial_t + e_{\alpha j}\partial_{j)} F_\alpha(\boldsymbol{x}, t) + O(\varepsilon^2), \qquad (3.139)$$

Combining Eqs. (3.138), (3.139) and Eq. (3.134), the equations to orders ε^0, ε and ε^2 are

$$m_i^{(0)} = m_i^{(eq)}, \qquad (3.140)$$

$$\left(\partial_t + e_{\alpha j}\partial_j\right) f_\alpha^{(0)} = -(\boldsymbol{T_r^{-1}S})_{\alpha i} m_i^{(1)} + F_\alpha. \qquad (3.141)$$

$$\left(\partial_t + e_{\alpha j}\partial_j\right) f_\alpha^{(1)} + \frac{1}{2}(\partial_t + e_{\alpha j}\partial_j)^2 f_\alpha^{(0)} = -(\boldsymbol{T_r^{-1}S})_{\alpha i} m_i^{(2)} + \frac{1}{2}(\partial_t + e_{\alpha j}\partial_{j)} F_\alpha. \quad (3.142)$$

Eqs. (3.140-3.142) can be written with matrices and vectors,

$$\boldsymbol{m}^{(0)} = \mathrm{m}^{(\mathrm{eq})}, \quad (3.143)$$

$$(\partial_t \boldsymbol{I} + \boldsymbol{E})\boldsymbol{T_r^{-1}}\, \boldsymbol{m}^{(0)} = -\boldsymbol{T_r^{-1}S}\boldsymbol{m}^{(1)} + \boldsymbol{F}, \quad (3.144)$$

$$(\partial_t \boldsymbol{I} + \boldsymbol{E})\boldsymbol{T_r^{-1}}\boldsymbol{m}^{(1)} + \frac{1}{2}\boldsymbol{T_r}(\partial_t \boldsymbol{I} + \boldsymbol{E})^2\boldsymbol{T_r^{-1}}\boldsymbol{m}^{(0)} = -\boldsymbol{T_r^{-1}S}\boldsymbol{m}^{(2)} + \frac{1}{2}(\partial_t \boldsymbol{I} + \boldsymbol{E})\boldsymbol{F}, \quad (3.145)$$

where $\boldsymbol{I}$ is the identity matrix; $\boldsymbol{E}$ is a diagonal matrix as

$$\boldsymbol{E} = diag\left[e_{0j}\partial_j, e_{1j}\partial_j, e_{2j}\partial_j, e_{3j}\partial_j, e_{4j}\partial_j, e_{5j}\partial_j, e_{6j}\partial_j, e_{7j}\partial_j, e_{8j}\partial_j\ \right]; \quad (3.146)$$

$$\boldsymbol{m}^{(1)} = [0, e^{(1)}, e^{2(1)}, 0,\ q_x^{(1)},\ 0,\ q_y^{(1)},\ p_{xx}^{(1)},\ p_{xy}^{(1)}]^T; \quad (3.147)$$

$$\boldsymbol{m}^{(2)} = [0, e^{(2)}, e^{2(2)}, 0,\ q_x^{(2)},\ 0,\ q_y^{(2)},\ p_{xx}^{(2)},\ p_{xy}^{(2)}]^T; \quad (3.148)$$

and

$$\boldsymbol{F} = [0, 3w_1\frac{e_{1i}F_i}{e^2}, 3w_2\frac{e_{2i}F_i}{e^2},\ 3w_3\frac{e_{3i}F_i}{e^2}, 3w_4\frac{e_{4i}F_i}{e^2}, 3w_5\frac{e_{5i}F_i}{e^2}, 3w_6\frac{e_{6i}F_i}{e^2}, 3w_7\frac{e_{7i}F_i}{e^2}, 3w_8\frac{e_{8i}F_i}{e^2}]^T. \quad (3.149)$$

Substituting Eq. (3.144) into Eq.(3.145) leads to

$$(\partial_t \boldsymbol{I} + \boldsymbol{E})\boldsymbol{T_r^{-1}}(\boldsymbol{I} - \frac{1}{2}\boldsymbol{S})\boldsymbol{m}^{(1)} = -\boldsymbol{T_r^{-1}S}\boldsymbol{m}^{(2)}. \quad (3.150)$$

Multiplying Eqs. (3.144) and (3.150) by $\boldsymbol{T_r}$ gives

$$(\partial_t \boldsymbol{I} + \boldsymbol{T_r}\boldsymbol{E}\boldsymbol{T_r^{-1}})\, \boldsymbol{m}^{(0)} = -\boldsymbol{S}\boldsymbol{m}^{(1)} + \boldsymbol{T_r}\boldsymbol{F}. \quad (3.151)$$

$$(\partial_t \boldsymbol{I} + \boldsymbol{T_r}\boldsymbol{E}\boldsymbol{T_r^{-1}})(\boldsymbol{I} - \frac{1}{2}\boldsymbol{S})\boldsymbol{m}^{(1)} = -\boldsymbol{S}\boldsymbol{m}^{(2)}. \quad (3.152)$$

Writing out Eq. (3.151) for $s = 0$, 1, 3, 5, 7, and 8 yields:

$$\partial_t h + \partial_x(hu) + \partial_y(hv) = 0 \quad (3.153)$$

$$\partial_t\left(-4h + \frac{3gh^2}{e^2} + \frac{3h\left(u^2+v^2\right)}{e^2}\right) = -s_1 e^{(1)} \quad (3.154)$$

$$\partial_t\left(\frac{hu}{e}\right) + \partial_x\left(\frac{gh^2}{2e} + \frac{hu^2}{e}\right) + \partial_y\left(\frac{huv}{e}\right) = \frac{F_x}{e} \quad (3.155)$$

$$\partial_t\left(\frac{hv}{e}\right) + \partial_y\left(\frac{gh^2}{2e} + \frac{hv^2}{e}\right) + \partial_x\left(\frac{huv}{e}\right) = \frac{F_y}{e} \quad (3.156)$$

$$\partial_t\left(\frac{h\left(u^2-v^2\right)}{e^2}\right) + \frac{2}{3}\partial_x(hu) - \frac{2}{3}\partial_y(hv) = -s_7 p_{xx}^{(1)} \quad (3.157)$$

$$\partial_t\left(\frac{huv}{e}\right) + \frac{1}{3}\partial_x(hv) + \frac{1}{3}\partial_y(hu) = -s_8 p_{xy}^{(1)} \quad (3.158)$$

Writing out Eq. (3.152) for the conserved moments, $s = 3$ and 5 results in the follow equations:

$$\partial_x\left(\frac{1}{6}\left(1 - \frac{s_1}{2}\right)e^{(1)} + \frac{1}{2}\left(1 - \frac{s_7}{2}\right)p_{xx}^{(1)}\right) + \partial_y\left(\left(1 - \frac{s_8}{2}\right)p_{xy}^{(1)}\right) = 0 \quad (3.159)$$

$$\partial_y[\tfrac{1}{6}\left(1-\tfrac{s_1}{2}\right)e^{(1)} - \tfrac{1}{2}\left(1-\tfrac{s_7}{2}\right)p_{xx}^{(1)}] + \partial_x[\left(1-\tfrac{s_8}{2}\right)p_{xy}^{(1)}] = 0 \tag{3.160}$$

Combining the zeroth-order equations (3.155) and (3.156) with the first-order equations (3.159) and (3.160) respectively, we have

$$\partial_t(hu) + \partial_x\left(\frac{gh^2}{2} + hu^2\right) + \partial_y(huv) = F_x - \varepsilon\frac{e^2}{6}\left(1-\frac{s_1}{2}\right)\partial_x(e^{(1)})$$

$$-\varepsilon\tfrac{e^2}{6}\left(1-\tfrac{s_7}{2}\right)\partial_x(p_{xx}^{(1)}) - \varepsilon e^2\left(1-\tfrac{s_8}{2}\right)\partial_y\left(p_{xy}^{(1)}\right) \tag{3.161}$$

$$\partial_t(hv) + \partial_y\left(\frac{gh^2}{2} + hv^2\right) + \partial_x(huv) = F_y - \varepsilon\frac{e^2}{6}\left(1-\frac{s_1}{2}\right)\partial_y(e^{(1)})$$

$$+\varepsilon\tfrac{e^2}{6}\left(1-\tfrac{s_7}{2}\right)\partial_y(p_{xx}^{(1)}) - \varepsilon e^2\left(1-\tfrac{s_8}{2}\right)\partial_x\left(p_{xy}^{(1)}\right) \tag{3.162}$$

Ignoring the higher order terms, the following expressions from Eqs. (3.154), (3.157) and (3.158) can be obtained

$$e^{(1)} = 0 \tag{3.163}$$

$$p_{xx}^{(1)} = -\tfrac{2}{3s_7}[\partial_x(hu) - \partial_y(hv)] \tag{3.164}$$

$$p_{xy}^{(1)} = -\tfrac{2}{3s_8}[\partial_x(hv) + \partial_y(hu)] \tag{3.165}$$

Substituting Eqs. (3.163)-(3.165) into Eq. (3.161) gives

$$\partial_t(hu) + \partial_x\left(\frac{gh^2}{2} + hu^2\right) + \partial_y(huv) = F_x + \varepsilon\frac{e^2}{3}\left(\frac{1}{s_7} - \frac{1}{2}\right)\partial_x[\partial_x(hu) - \partial_y(hv)]$$

$$+\varepsilon\tfrac{e^2}{3}\left(\tfrac{1}{s_8} - \tfrac{1}{2}\right)\partial_y[\partial_x(hv) + \partial_y(hu)] \tag{3.166}$$

If setting $s_7 = s_8 = 1/\tau$, in which τ is the single relaxation time, and defining the kinematic viscosity $\nu = \varepsilon\frac{e^2}{6}(2\tau - 1)$ the equation (3.166) can be reduced to

$$\partial_t(hu) + \partial_x\left(\tfrac{gh^2}{2} + hu^2\right) + \partial_y(huv) = F_x + \nu[\partial_x^2(hu) + \partial_y^2(hu)] \tag{3.167}$$

Similarly the following equation can be obtained from Eq. (3.162)

$$\partial_t(hv) + \partial_y\left(\tfrac{gh^2}{2} + hv^2\right) + \partial_x(huv) = F_y + \nu[\partial_x^2(hv) + \partial_y^2(hv)] \tag{3.168}$$

Eqs. (3.153) (3.167) and (3.168) are just the shallow water equations. It may be noted that when $s_0 \ldots s_8 = 1/\tau$, the lattice Boltzmann method with a single relaxation τ time is recovered. Now, the shallow water equations are recovered from LABSWE$^{\text{MRT}}$ with improved calculation for a force term and its performance will be tested in chapter 5.

3.12 Solute Transport Equation

3.12.1 Lattice Boltzmann Model for Solute Transport Equation

Several lattice Boltzmann models for solute transport have been developed [46, 55, 136, 137]. Ginzburg [82] developed a lattice Boltzmann model with two-relaxation-time (TRT) collision operator for anisotropic advection dispersion equation. Zhang et al. [46] presented a lattice Boltzmann model for the advection-dispersion equation with BGK collision on rectangular lattice, and discuss its boundary conditions [138]. In this thesis, a D2Q5 lattice Boltzmann model for advection-diffusion developed by Zhou [136] equation is adopted. The most important difference between this model and the others [46, 55, 137] is that the dispersion coefficient is not dependent on the relaxation time, and hence the relaxation time can be chosen freely for better accuracy and stability. However, in the other models, the dispersion coefficient is related to the relaxation time, and if the relaxation time calculated by the dispersion coefficient is very small, the computation will become unstable. Furthermore, the other models applied for solute transport by the lattice Boltzmann method are based on D2Q9, but the model adopted in this paper is based on D2Q5 (see Figure 3.3), which is simpler and saves computational effort. Another advantage of the model applied is that a rectangular lattice and different dispersion coefficients in the *x* and *y* directions can be used without modification [136] with a single relaxation time. The lattice Boltzmann equation based on BGK for the advection-diffusion equation is

$$g_\alpha(x + e_{1\alpha}\Delta t, t + \Delta t) - g_\alpha(x,t) = -\frac{1}{\tau_1}\left(g_\alpha(x,t) - g_\alpha^{eq}(x,t)\right) + \frac{h\Delta t}{5} S_c \qquad (3.169)$$

where, g_α is the distribution function of particles, g_α^{eq} is the local equilibrium distribution function, S_c is the source term, τ_1 is single relaxation time and $e_{1\alpha}$ is the velocity vector of a particle in link α, as follows:

$$e_{1\alpha} = \begin{cases} (0,0), & \alpha = 0 \\ e_x\left[cos\frac{(\alpha-1)\pi}{2}, sin\frac{(\alpha-1)\pi}{2}\right], & \alpha = 1,3 \\ e_y\left[cos\frac{(\alpha-1)\pi}{2}, sin\frac{(\alpha-1)\pi}{2}\right], & \alpha = 2,4 \end{cases} \qquad (3.170)$$

in which, $e_x = \Delta x/\Delta t$, $e_y = \Delta y/\Delta t$, Δx and Δy are the lattice size in the *x* and *y* directions respectively. Δx is equal to Δy for simplicity in this paper.

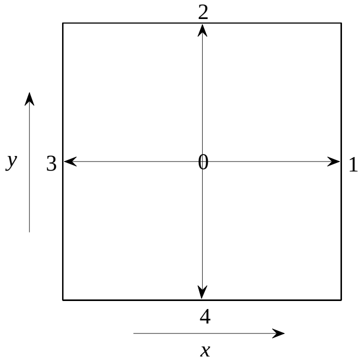

Figure 3.3 5-speed square (D2Q5) lattice in horizontal plane.

The equilibrium distribution function is defined as

$$g_\alpha^{eq} = \begin{cases} \left(1 - \frac{\lambda_y e_x^2 + \lambda_x e_y^2}{e_x e_y}\right) hC, & a = 0 \\ \left(\frac{1}{2}\frac{e_y}{e_x}\lambda_x + \frac{e_{ai}u_i}{2e_x^2}\right) hC, \alpha = 1 \; and \; 3 \\ \left(\frac{1}{2}\frac{e_x}{e_y}\lambda_y + \frac{e_{ai}u_i}{2e_y^2}\right) hC, \alpha = 2 \; and \; 4 \end{cases} \tag{3.171}$$

in which, $\lambda_i = \frac{D_{ij}}{\Delta t(\tau_1 - \frac{1}{2})e_x e_y}$ is non-dimensional, and D_{ij} is dispersion coefficient in the *ij* direction. The concentration can be calculated by

$$C = \left(\sum_\alpha g_\alpha\right)/h \tag{3.172}$$

The advection-diffusion equation (2.61) can be recovered from Eq. (3.169) by using the Chapman-Enskog analysis [136]. In order to simplify the process, the source term is not included in the following derivation.

3.12.2 Recovery of the Advection-diffusion Equation

In order to recover the advection-diffusion equation, the following constraints are introduced:

$$\sum_\alpha g_\alpha^{eq} = hC \tag{3.173}$$

$$\sum_\alpha e_{\alpha i} g_\alpha^{eq} = u_i hC \tag{3.174}$$

Substituting the Equation (3.173) into Equation (3.172) results in

$$\sum_\alpha g_\alpha = \sum_\alpha g_\alpha^{eq} \tag{3.175}$$

The Chapman-Enskog expansion is used recover the advection-diffusion equation (2.61) from Equation (3.169) as follows:

With the purpose of this, Δt is assumed to be small and equal to ε

$$\Delta t = \varepsilon \tag{3.176}$$

Substituting Equation (3.176) into Equation (3.169) and ignoring the source term results in

$$g_\alpha(\boldsymbol{x} + \boldsymbol{e}_\alpha \varepsilon, t + \varepsilon) - g_\alpha(\boldsymbol{x}, t) = -\tfrac{1}{\tau_1}\left(g_\alpha - g_\alpha^{eq}\right) \tag{3.177}$$

Applying a Taylor expansion to the left-hand side of Equation (3.177) in time and space around point ($\boldsymbol{x}$, t), one can have

$$\varepsilon\left(\frac{\partial}{\partial t} + e_{\alpha j}\frac{\partial}{\partial x_j}\right)g_\alpha + \frac{1}{2}\varepsilon^2\left(\frac{\partial}{\partial t} + e_{\alpha j}\frac{\partial}{\partial x_j}\right)^2 g_\alpha + O(\varepsilon^3) = -\tfrac{1}{\tau_1}\left(g_\alpha - g_\alpha^{eq}\right) \tag{3.178}$$

Using the Chapman-Enskog expansion, $g_\alpha$can be expressed as

$$g_\alpha = g_\alpha^{(0)} + \varepsilon g_\alpha^{(1)} + \varepsilon^2 g_\alpha^{(2)} + O(\varepsilon^3) \tag{3.179}$$

Taking the Equation (3.178) to order ε^0, ε, ε^2 and the following equations can be obtained:

$$g_\alpha^{(0)} = g_\alpha^{eq} \tag{3.180}$$

$$\left(\frac{\partial}{\partial t} + e_{\alpha j}\frac{\partial}{\partial x_j}\right)g_\alpha^{(0)} = -\frac{1}{\tau_1}g_\alpha^{(1)} \tag{3.181}$$

$$\left(\frac{\partial}{\partial t} + e_{\alpha j}\frac{\partial}{\partial x_j}\right)g_\alpha^{(1)} + \frac{1}{2}\left(\frac{\partial}{\partial t} + e_{\alpha j}\frac{\partial}{\partial x_j}\right)^2 g_\alpha^{(0)} = -\frac{1}{\tau_1}g_\alpha^{(2)} \tag{3.182}$$

Substituting Equation (3.181) into Equation (3.182) leads to

$$\left(1 - \frac{1}{2\tau_1}\right)\left(\frac{\partial}{\partial t} + e_{\alpha j}\frac{\partial}{\partial x_j}\right)g_\alpha^{(1)} = -\frac{1}{\tau_1}g_\alpha^{(2)} \tag{3.183}$$

Taking [Equation (3.181) + Equation (3.183) ×ε], the following equation can be obtained

$$\left(\frac{\partial}{\partial t} + e_{\alpha j}\frac{\partial}{\partial x_j}\right)g_\alpha^{(0)} + \varepsilon\left(1 - \frac{1}{2\tau_1}\right)\left(\frac{\partial}{\partial t} + e_{\alpha j}\frac{\partial}{\partial x_j}\right)g_\alpha^{(1)} = -\frac{1}{\tau_1}\left(g_\alpha^{(1)} + \varepsilon g_\alpha^{(2)}\right) \tag{3.184}$$

Summing Equation (3.184) and rearranging it with the following equations.

$$\textstyle\sum_\alpha g_\alpha^{(1)} = \sum_\alpha g_\alpha^{(2)} = 0 \tag{3.185}$$

$$\frac{\partial}{\partial t}\textstyle\sum_\alpha g_\alpha^{(1)} = 0 \tag{3.186}$$

According to the conservation condition (3.175), the following equation can be given:

$$\frac{\partial}{\partial t}\textstyle\sum_\alpha g_\alpha^{(0)} + \frac{\partial}{\partial x_j}\sum_\alpha e_{\alpha j}g_\alpha^{(0)} + \varepsilon\left(1 - \frac{1}{2\tau_1}\right)\frac{\partial}{\partial x_j}\sum_\alpha e_{\alpha j}g_\alpha^{(1)} = 0 \tag{3.187}$$

Substituting Equation (3.181) into Equation (3.187) gives

$$\frac{\partial}{\partial t}\sum_{\alpha} g_{\alpha}^{(0)} + \frac{\partial}{\partial x_i}\sum_{\alpha} e_{\alpha i} g_{\alpha}^{(0)} = \varepsilon\left(\tau_1 - \frac{1}{2}\right)\frac{\partial}{\partial x_i}\sum_{\alpha}\left(e_{\alpha i} e_{\alpha j}\frac{\partial g_{\alpha}^{(0)}}{\partial x_j}\right) + \varepsilon\left(\tau_1 - \frac{1}{2}\right)\frac{\partial}{\partial x_i}\sum_{\alpha}\left(e_{\alpha i}\frac{\partial g_{\alpha}^{(0)}}{\partial t}\right) \quad (3.188)$$

According to [46] , comparing with the first term, the last term on the right-hand side of Equation (3.188) is smaller, so it can be ignored and treated as a truncation error. Combining Equations (3.171), (3.173), (3.174) and (3.180) with Equation (3.188) leads to

$$\frac{\partial hC}{\partial t} + \frac{\partial (u_i hC)}{\partial x_i} = \frac{\partial}{\partial x_i}\left[\lambda_i \varepsilon \left(\tau_1 - \frac{1}{2}\right) e_x e_y \frac{\partial hC}{\partial x_i}\right] \quad (3.189)$$

with

$$\lambda_i \varepsilon \left(\tau_1 - \frac{1}{2}\right) e_x e_y = D_i \quad (3.190)$$

Then Equation (3.189) is the advection-diffusion equation (2.61) without source term. Considering $\varepsilon = \Delta t$ in Equation (3.176), rewriting Equation (3.190) can give the expression of λ_i as

$$\lambda_i = \frac{D_i}{\Delta t\left(\tau_1 - \frac{1}{2}\right) e_x e_y} \quad (3.191)$$

Chapter 4: Initial and Boundary Conditions

4.1 Introduction

In this chapter, various boundary conditions and inlet and outlet boundary conditions are described such as no-slip, semi-slip and slip. Study shows that the boundary condition play a critical role on the results of simulation and can affect the simulation's accuracy, efficiency and stability [93]. Some typical work can be found in [123, 139-141]. Boundary conditions and initial conditions are still the fundamental problem of LBM and attract much attention [90, 107, 124, 142]. But this is beyond of this thesis, and we just briefly introduce the common boundary conditions and more detailed work can be referred to [106, 143, 144].

4.2 Solid Boundary Condition

4.2.1 No-slip Boundary Condition

One of the most attractive advantages of LBM is its simple treatment of boundary conditions such as the bounce-back scheme. It can be implemented easily for flows in arbitrary complex geometries. The bounce-back and similar schemes for different boundary conditions, is very simple and efficient for no-slip, semi-slip and slip boundary conditions and is used widely for various flow problems. For example, in the bounce-back scheme as shown in Figure 4.1, the part below AB is a wall and defined as solid; the part above is fluid. The unknown incoming distribution functions f_2, f_3 and f_4 from the solid are simply equal to f_6, f_7 and f_8, respectively. Consequently, the specific location of solid points is not required and the programming is easy, making it the most efficient treatment for a no-slip boundary condition for flows in complex geometry [3, 44, 45, 145].

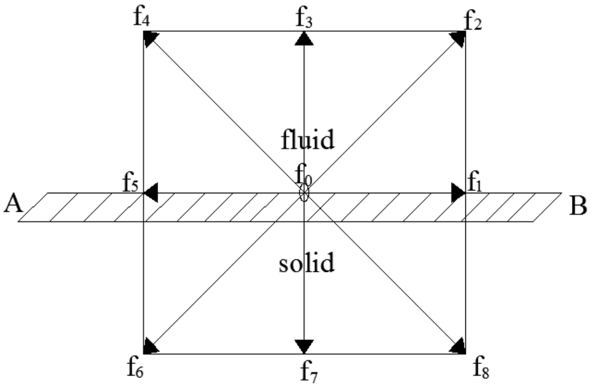

Figure 4.1 Layout of wall boundary and lattice nodes.

4.2.2 Slip Boundary Condition

If the boundary is smooth with little friction, the slip boundary should be used. As Figure 4.1 shows, the unknown distribution functions f_2, f_3, and f_4.

$$f_2 = f_8, \quad f_3 = f_7, \quad f_4 = f_6. \tag{4.1}$$

It means that no momentum is changed in the direction normal to a wall and the velocity along the wall is kept.

4.2.3 Semi-slip Boundary Condition

In practical flows, a large velocity gradient exists near the boundary for turbulent flows due to the effect of wall friction. It cannot be described by slip or no-slip boundary conditions, and hence the semi-slip boundary is described to deal with this case. In order to construct the semi-slip boundary condition, the wall shear stress should be included. According to [3], the wall shear stress τ_{fi} can be expressed by

$$\tau_{fi} = -\rho C_f u_i \sqrt{u_j u_j} \tag{4.2}$$

in which, C_f is the friction factor at the wall and can be constant or determined by $C_f = g\frac{n_f^2}{h^{1/3}}$ with n_f is the Manning's coefficient at the wall. By adding the wall shear stress to the force term, the semi-slip boundary condition is developed together with slip boundary. It should be noted that the distribution function is still dealt with by the slip boundary condition.

4.3 Inflow and Outflow Condition

In order to obtain the correct results, the proper inlet and outlet boundary condition should be specified and it adds a constraint to flow for consistency with surrounding flow. As the LABSWE is only applicable to subcritical flow, the discharge and water depth are specified at inlet and outlet respectively normally. As Figure 4.2 shown, at inlet the distribution function f_1, f_2, f_8 are unknown. If the water depth and velocity are known, these unknown distribution functions can be determined by the following equations as Zou and He [139], Zhou [3] proposed. According to mass and momentum conservation, with the relations (3.54) and (3.59), the following equations can be obtained:

$$f_1 + f_2 + f_3 + f_4 + f_5 + f_6 + f_7 + f_8 + f_9 = h \tag{4.3}$$

$$e(f_1 + f_2 + f_8) - e(f_4 + f_5 + f_6) = hu \tag{4.4}$$

$$e(f_2 + f_3 + f_4) - e(f_6 + f_7 + f_8) = hv \tag{4.5}$$

If *v*=0 is assumed, based on the above equations, f_1, f_2, f_8 can be expressed as

$$f_1 = f_5 + \frac{2hu}{3e}\,, \tag{4.6}$$

$$f_2 = \frac{hu}{6e} + f_6 + \frac{f_7 - f_3}{2}, \tag{4.7}$$

$$f_8 = \frac{hu}{6e} + f_4 + \frac{f_3 - f_7}{2}. \tag{4.8}$$

Similarly, the unknown f_4, f_5, f_6 at outflow boundary can be calculated by

$$f_5 = f_1 - \frac{2hu}{3e}, \tag{4.9}$$

$$f_4 = -\frac{hu}{6e} + f_8 + \frac{f_7 - f_3}{2}, \tag{4.10}$$

$$f_6 = -\frac{hu}{6e} + f_2 + \frac{f_3 - f_7}{2}, \tag{4.11}$$

But, normally the water depth and velocity are unknown at inlet and they can be assumed by the zero gradient method or exploration method.

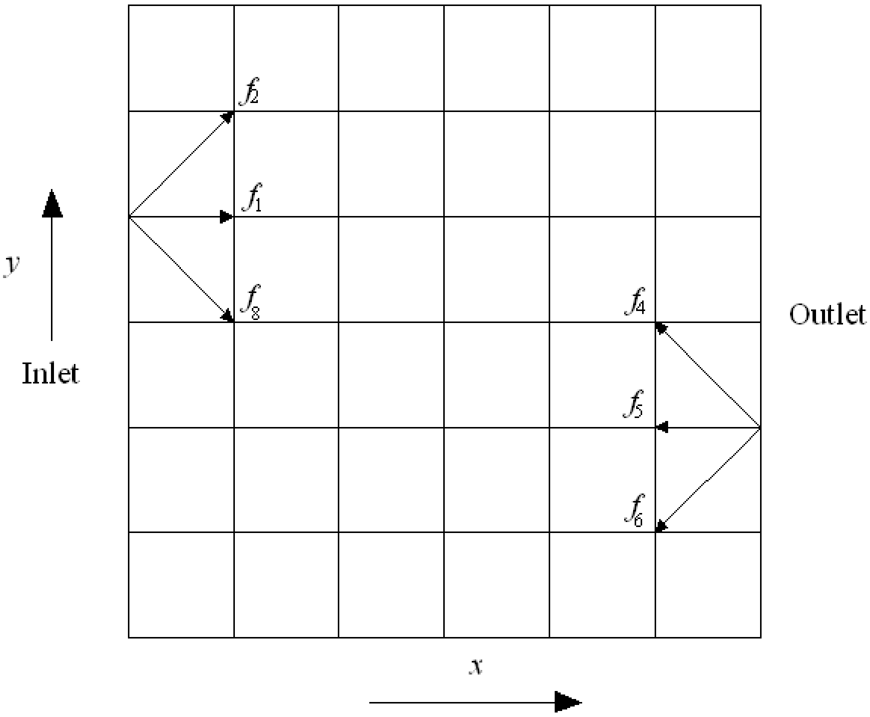

Figure 4.2 Inlet and outlet boundary conditions.

For zero-gradient method:

$$u(1,j) = u(2,j), \tag{4.12}$$

$$v(1,j) = v(2,j), \tag{4.13}$$

$$h(1,j) = h(2,j), \tag{4.14}$$

or exploration:

$$h(1,j) = 2 \times h(2,j) - h(3,j), \tag{4.15}$$

and assuming $v(1,j) = 0$ according to equations (4.3) and (4.4), one has

$$u(1,j) = \left[\frac{f_0+f_3+f_7+2(f_4+f_5+f_6)}{h(1,j)} - 1\right] e \tag{4.16}$$

The water depth and water velocity obtained by zero-gradient method or exploration cannot meet the requirement of constant discharge at inlet, and a revised step is needed as follows:

Q_0 is the specified discharge and Q_{in} is the calculated discharge. The equation (4.4) can be revised by adding the $(Q_0$-$Q_{in})/b$ which is a revised unit discharge.

$$e(f_1+f_2+f_8) - e(f_4+f_5+f_6) = hu + \frac{(Q_0 - Q_{in})}{b} \tag{4.17}$$

So, f_1, f_2, f_8 can be updated as:

$$f_1 = f_5 + \frac{2hu}{3e}, \tag{4.18}$$

$$f_2 = \frac{hu+(Q_0-Q_{in})/b}{6e} + f_6 + \frac{f_7-f_3}{2} + \frac{hv}{2e}, \tag{4.19}$$

$$f_8 = \frac{hu+(Q_0-Q_{in})/b}{6e} + f_4 + \frac{f_3-f_7}{2} - \frac{hv}{2e}. \tag{4.20}$$

For the outlet boundary, the water depth is fixed and velocity can be calculated by

$$u(Lx,j) = \left[\frac{f_0+f_3+f_7+2(f_4+f_5+f_6)}{h_0} - 1\right] e \tag{4.21}$$

$$v(Lx,j) = v(Lx,j)h(Lx,j)/h_0 \tag{4.22}$$

So, the f_4, f_5, f_6 at outlet can be calculated as :

$$f_5 = f_1 + \frac{2hu}{3e}, \tag{4.23}$$

$$f_4 = -\frac{hu}{6e} + f_8 + \frac{f_7-f_3}{2} + \frac{hv}{2e}. \tag{4.24}$$

$$f_6 = -\frac{hu}{6e} + f_2 + \frac{f_3-f_7}{2} - \frac{hv}{2e}, \tag{4.25}$$

If the no-slip boundary condition is used for the wall boundary, the corner point at the inlet needs to be treated carefully. More details are given in [93].

4.4 Periodic Boundary Condition

A periodic boundary condition may be used for some specific cases [3]. For example, if a flow region consists of a tidal flow, a periodic boundary condition can be used. According to the flow feature, a periodic boundary condition in the *x* direction can be achieved by specifying the unknown f_1 , f_2 and f_8 at inflow boundary (see Figure 4.2) with streaming to the corresponding distributions at outflow boundary,

$$f_\alpha(1,j) = f_\alpha(N_x,j), \alpha = 1,2,8, \tag{4.26}$$

and the unknown f_4, f_5 and f_6 at outflow to that at inflow boundary,

$$f_\alpha(N_x,j) = f_\alpha(1,j), \alpha = 4,5,6. \tag{4.27}$$

Similarly, a periodic boundary condition in the *y* direction can be achieved.

4.5 Initial Condition

Before computation, the initial condition for distribution function needs to be specified. Generally, there are two ways to specify the initial condition in the lattice Boltzmann method [3]. One is to specify a random value between 0 and 1 for the distribution function. The other is to assume a flow field with water depth and velocity firstly, then compute the local equilibrium distribution function f_α^{eq} and use it as an initial condition for f_α. Normally, it is easier to specify a macroscopic quantity than a microscopic. So, the second method is better in practical computation, which is used in the present models. It is obvious that there is no difference between results calculated with these two initial conditions for a steady flow problem.

4.6 Solution Procedure

The solution procedures for the LABSWE, LABSWE^{TM} and LABSWE^{MRT} are extremely simple. It involves only explicit calculations and consists of the following steps:

For LABSWE or LABSWE^{TM}

1. Assume initial water depth and velocity,
2. Compute f_α^{eq} from Eq. (3.49),
3. Calculate the f_α from the lattice Boltzmann equation (3.24), or from the Equation (3.103) for turbulent flows together with the total relaxation time τ_t calculated from Eq. (3.113).
4. Renew the water depth *h* and the velocity *u* and *v* by Eqs. (3.54) and (3.59),
5. Go back to step 2 and repeat the above procedure until a solution is obtained.

For LABSWE^{MRT}

1. Assume initial water depth and velocity,
2. Compute the equilibrium values of moments m^{eq} from Eq. (3.133)
3. Calculate the f_α from the lattice Boltzmann equation (3.131),
4. Renew the water depth *h* and the velocity *u* and *v* from Eqs. (3.54) and (3.59),
5. Go back step 2 and repeat the above procedure until a solution is obtained.

Chapter 5: Applications of LABSWE^{TM} and LABSWE^{MRT} for the Free Surface Flows

5.1 The Flows in Rectangular Shallow Basins

5.1.1 Introduction

In order to verify the presented model LABSWE^{TM}, its results are compared with corresponding experiments. Furthermore, the asymmetrical flows occurring in the rectangular basins with different ratios of length to width are simulated. The effects of the Froude number and bed friction on flow asymmetry and reattachment length are investigated. The aim is to test the feasibility and accuracy of the lattice Boltzmann method to study free surface flows in shallow rectangular basins.

5.1.2 Background

Shallow waters in open channels with sudden expansions are often observed in natural rivers and have received much attention. Additionally, the instabilities of flow in a symmetric expanded channel are well known [146-148]. Mullin et al. [147] examined the effect of variable ratios of the inlet to outlet channel widths within a 1:3 expansion experimentally and numerically and concluded that the length of the expanded section played a critical role in evaluating the effect of the ratio on flow instability, in which the flow is closed and limited to low Reynolds number (about 100). Graber [146] developed a mathematical stability criterion for subcritical flows in horizontal channels with rectangular expansions. Babarutsi et al. [149, 150] investigated shallow recirculation flows by experiments and numerical simulation. Both Babarutsi and Graber’s research focused on an expanded channel without contraction. The turbulent flows in shallow basins have also been studied for their important effects on aquaculture [151] and on sedimentation patterns [152, 153]. Dufresne et al. [154] investigated the symmetric and asymmetric flows in rectangular shallow reservoirs with different lateral expansion ratio and dimensionless length by numerical simulation.

Of particular note, Dewals et al. [148] analyzed the free surface turbulent flows in several shallow rectangular basins by experiments and numerical simulation using the $k-\varepsilon$ turbulence model and an algebraic turbulence model for high Reynolds number of 17500. They found that the flow pattern might become asymmetric even if the inflow and outflow boundary conditions and geometry of the basin were symmetric; the numerical simulations were found to reproduce the global experimental flow patterns.

5.1.3 Boundary Conditions

The boundary conditions include inlet, outlet and sidewalls. In the present study, semi-slip boundary condition for sidewalls is used (as applied by Dewals et al. [148]), in which side wall friction coefficient $C_{wall}=4C_b$ and C_b is bed-friction coefficient. The water depth is determined at inlet boundary, $h(1,y)=h(2,y)$; and the velocity is calculated with $u(1,y)=q(y)/h(1,y)$, in which the unit discharge $q(y)$ is linear variation along the streamwise direction y following Dewals et al. [148]. Stochastic treatment is not adopted at inlet. For outlet, the water depth h_0 is specified.

5.1.4 Numerical Simulation

It is known that open shallow flows in rectangular reservoirs can show a bifurcating behaviour under certain conditions [146, 148, 152]. This will be shown in this section. The same channel used by Dewals et al. [148] is adopted and shown in Figure 5.1. It consists of inlet channel with width b= 0.25m, expansion rectangular channel and outlet channel. The expansion rectangular channels with different length and width are considered, among which the channel with 6m long and 4m wide is studied in detail.

The simulated flow vectors for different length and width have been compared with the experiments in Figures 5.2 and 5.3 which indicate that the simulations qualitatively agree with the experiments. Quantitative comparison will be discussed in the following sections. Meanwhile, different aspect ratios (L/B) and expansion ratios (B/b) have been studied for bifurcation phenomenon; here L and B are the length and width of the rectangle, respectively. The global moment N is used to quantify asymmetry of flow fields $N=\frac{1}{L}\int_0^L |M|\,dx$, in which $M=\frac{2}{UB^2}\int_{-B/2}^{B/2} uy\,dy$ where $U = Q/(Bh_0)$ and Q = 0.007m^3/s, with the water depth h_0 at the outlet channel. Figure 5.4 shows that the flow bifurcates when the aspect ratio exceeds 1.25 or expansion ratio exceeds 2.5, which is consistent with that reported by Dewals et al. [148] although there is small difference in the global moment *N*. This demonstrates that the model can predict bifurcating behaviour of free surface flow in shallow rectangular basins.

In order to verify the method further, the numerical results are compared with those from the experiments and conventional numerical method with algebraic model for flow turbulence. The asymmetric flow pattern in this channel has been found by Dewals et al. [148] in experiments. According to Dewals' work, non-uniform specific discharge profile at the entrance to the inlet channel can generate the similar disturbance to flows as those in the experiment. The present numerical simulations confirm that such an approach can successfully produce asymmetric flows; hence it is used in the numerical studies.

In computation, uniform grids are used and Δt =0.01*s*. The single relaxation time is τ =0.53. The discharge is 0.007m^3/s in all cases. For case 1, the rectangular basin is 6m long and 4m wide; the bed friction coefficient $C_b = gn_b^2 / h^{1/3}$ is 0.0017 according to the Manning equation and inlet flow $F_r = u / \sqrt{gh}$ is 0.1. In outlet channel, b_1 is the same as b=0.25m.

In order to obtain the grid independent prediction, four different grid spaces (Δx = 0.0208m, 0.025m, 0.03125m and 0.042m) have been tested and the results are displayed in Figure 5.5. It indicates that the calculated results fluctuates slightly as grid spacing decreases and the Δx = 0.025m is small enough for present studies; therefore Δx = 0.025m is adopted in all the computations. In the test, the reattachment length has been selected here for assessing grid independence of the results. However, the grid spacing might turn out not to be fine enough if other parameter like threshold geometry is chosen for the assessment. Furthermore, the Smagorinsky constant C_s = 0.1, 0.2 and 0.3 were tested. The results showed that the reattachment length is little sensitive to these values and then C_s = 0.3 has been used in the present computation.

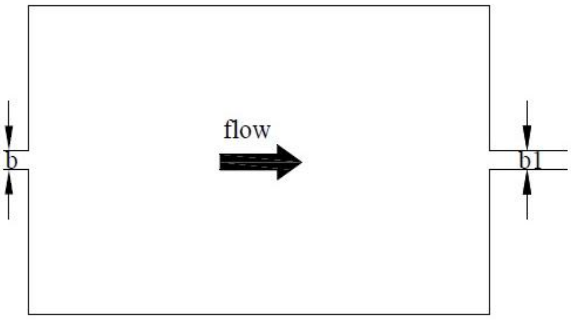

Figure 5.1 Sketch of the channel.

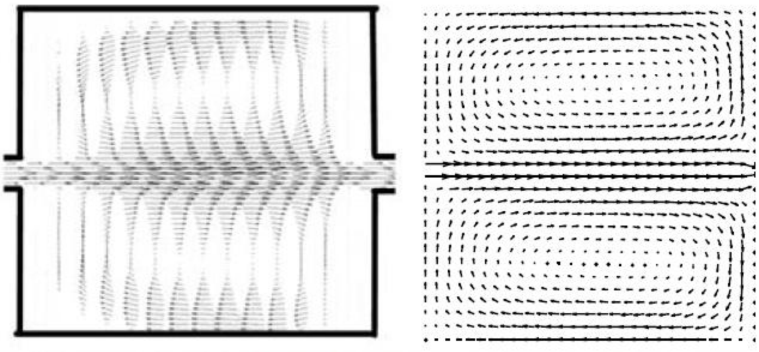

Figure 5.2 Experimental (left) and simulated (right) flow vectors in the basin of 4m wide and 4m long.

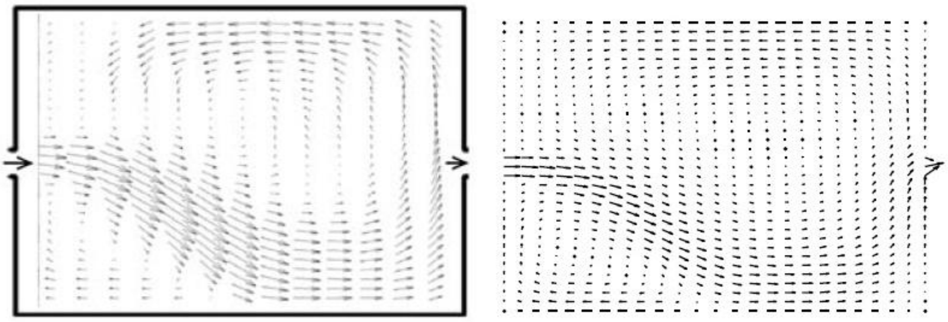

Figure 5.3 Experimental (left) and simulated (right) flow vectors in the basin of 4m wide and 6m long.

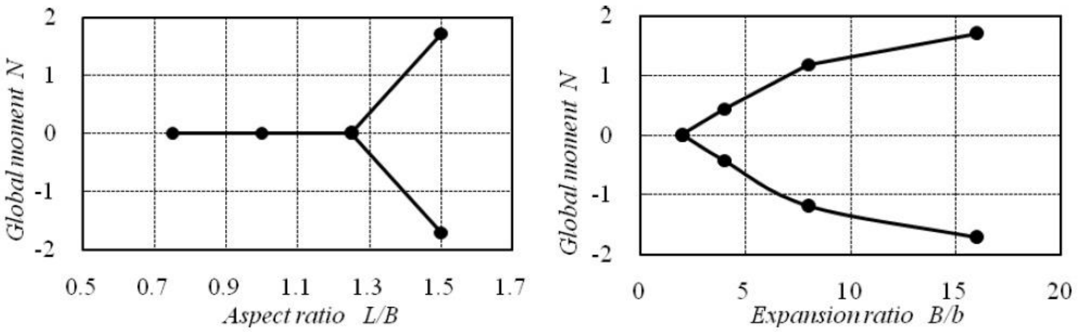

Figure 5.4 Bifurcation for different aspect ratio (*L/B*) and expansion ratio (*B/b*)

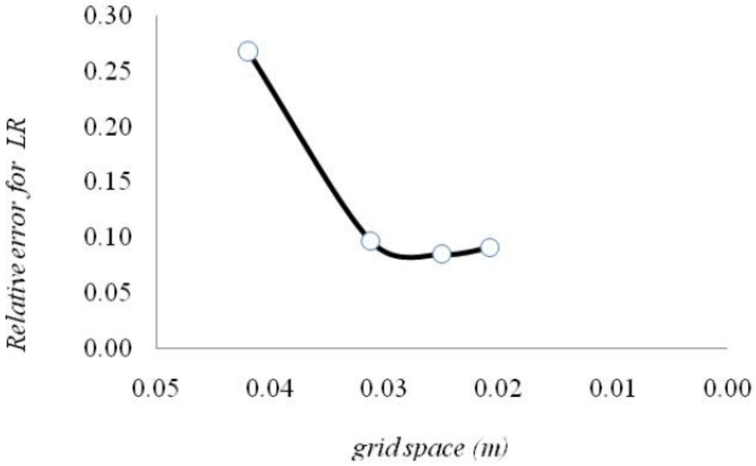

Figure 5.5 Relative error of *Lr* against grid size Δ*x*.

5.1.5 Comparisons of Results

In this section, the computed results for case1 are compared with the experimental results. The asymmetric moment *M* is used to quantify the asymmetry of the flow fields. Figure 5.6 displays the intensities of asymmetry obtained by the lattice Boltzmann model, the standard $k-\varepsilon$ model and the algebraic model as well as the experiments by Dewals et al. [148]. $\Delta E=\dfrac{M_{com}-M_{\exp}}{M_{\exp}}$ is used to evaluate the relative error between the predictions and experiments. In the figure for sections before *x*=1.8m, *M* is small and the differences among $k-\varepsilon$ model, algebraic model and lattice Boltzmann model are negligible compared with that for the other sections; hence the relative error ΔE is calculated for cross sections with $x > 1.8$m: the maximum errors are 0.51, 0.44 and 0.33 for k-ε model, algebraic model and lattice Boltzmann model, respectively. Their average relative errors are 0.29, 0.16 and 0.16, respectively. Thus, the lattice Boltzmann model seems to have equal ability of predicting flow fields to the algebraic model. Furthermore, computed *u* at four representative cross-sections are compared with the experimental data and the algebraic model results. Due to the large difference between the k-ε model results and experimental data, the results by k-ε model are not considered in the subsequent comparisons. From Figure 5.7 it is clear that the lattice Boltzmann model and algebraic model produce very similar results. Overall, the lattice Boltzmann model is found to predict the general flow patterns well in the rectangular basins.

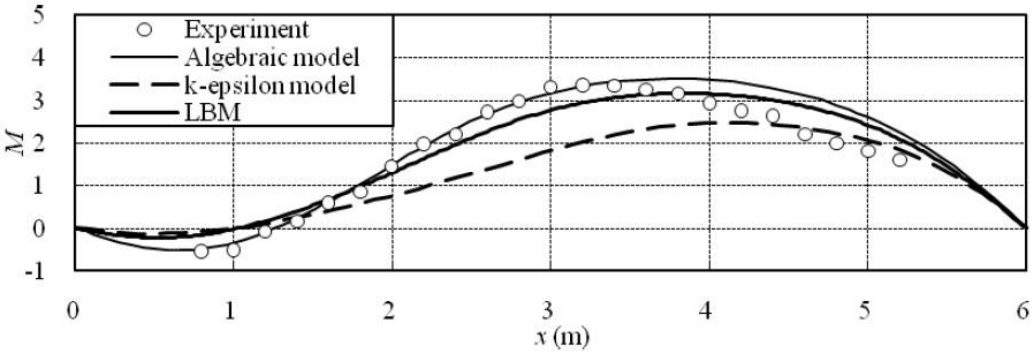

Figure 5.6 Comparisons of intensities of asymmetry.

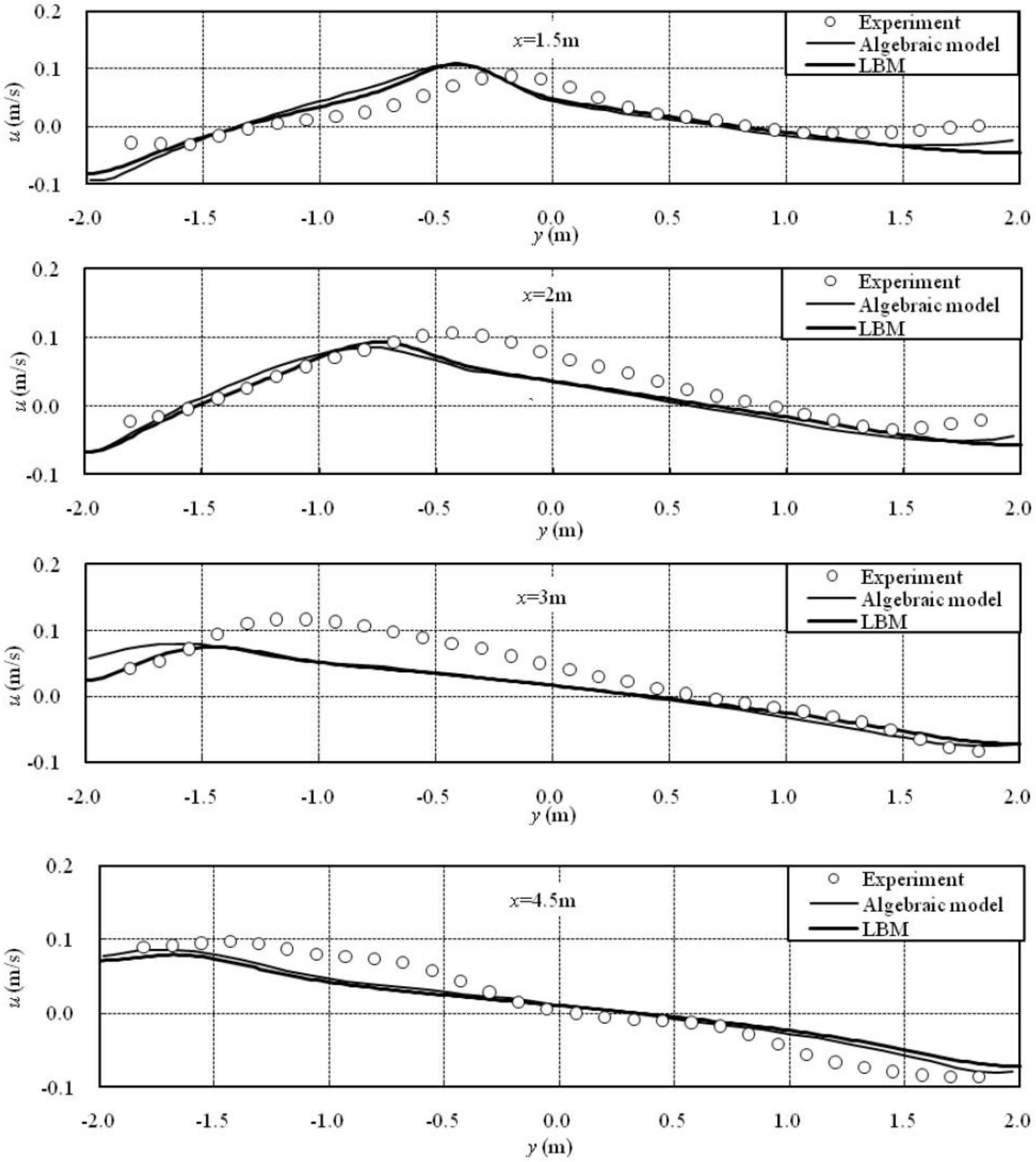

Figure 5.7 Comparisons of streamwise velocities at *x* =1.5m, 2m, 3m, and 4.5m.

5.1.6 Sensitivity Analysis

Four different Froude numbers, *Fr*=0.10, 0.15, 0.28 and 0.44, for Q =0.007m^3/s with variable water depths (h_0=0.2, 0.15, 0.1, and 0.075m) and velocity at the channel inlet are used to assess the influence of the intensity on flow asymmetry. Figure 5.8 illustrates the asymmetrical moment distribution under different Froude numbers. It is apparent that the global flow asymmetry reduces with increase of Froude number. This is confirmed by Dewals' research [148]. Furthermore, Froude number has clearly more influence on flow asymmetry in the range x = 1m and x = 5m compared to that outside this range.

According to Chen and Jirka [155], the parameter S_t=$C_b b/(2h)$ has been chosen to quantify the stabilizing effect of the bed-friction, where C_b is bed-friction coefficient; b is the inlet channel width and h is water depth. As Froude number increases, the water depth reduces, and then S_t becomes larger; hence the flow becomes less asymmetric. However, the above conclusion is only valid for the range Fr = 0.1 to 0.44. Outside this range, the flow regime may be different.

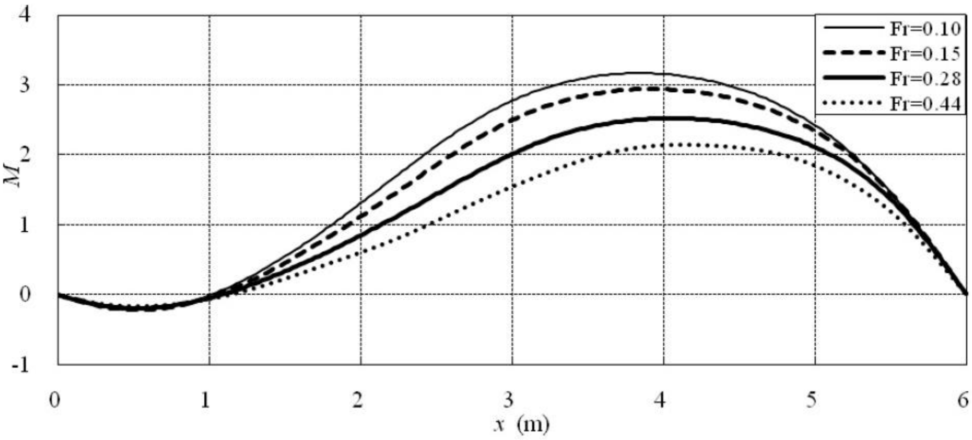

Figure 5.8 Asymmetrical moment distribution with different Froude numbers.

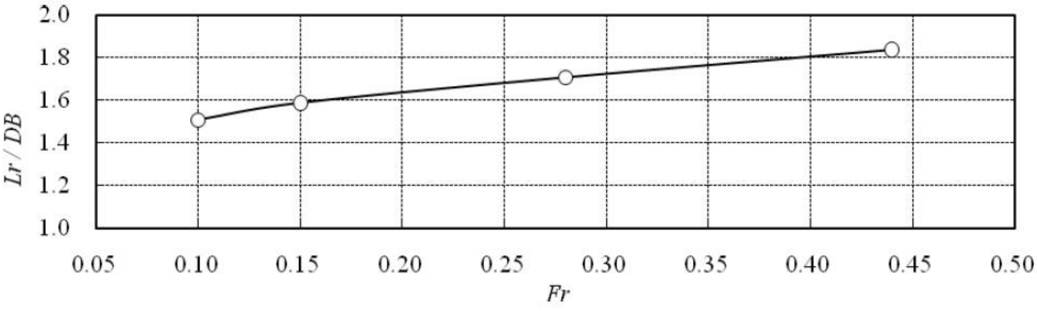

Figure 5.9 Reattachment length for different Froude numbers.

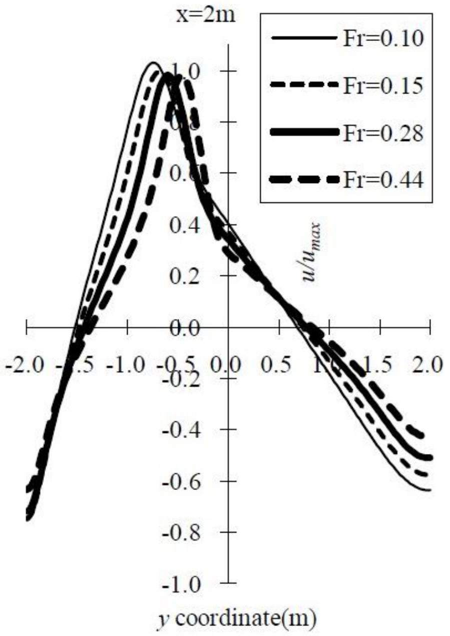

Figure 5.10 Normalized streamwise velocity u/u_{max} profiles at x = 2m.

Figure 5.9 displays the relation between reattachment length (L_r/DB, in which $DB=(B-b)/2$ is the expansion width) and the inlet Froude number. There is no doubt that reattachment length will increase with Froude number; and the recirculation zone will also become larger. However, this conclusion is a little different from those by Dufresne et al [152] for two reasons: firstly, the lateral expansion ratio is different (1.25 in Dufresne's paper but 7.5 in the present study), as well as the dimensionless length (20 in Dufresne's paper but 3.2 in present study); secondly, in Dufresne's research, the Froude number changes with discharge for a constant water depth, while the water depth varies and the discharge is kept constant in the present study.

The normalized streamwise velocity u/u_{max} profiles at cross-section x=2m for different Froude numbers are displayed in Figure 5.10. If the flow is symmetrical, the non-dimensional distribution of u component of the cross velocity should be symmetrical about the y axis, and vice versa. The farther the asymmetry axis deviates from the y axis, the more asymmetric the flow is. It can be seen from Figure 5.10 that the effect of the Froude number is different on both sides of the cross-section and is stronger in the vortex zone on the right hand side.

As mentioned above, three different values of parameter $S_t=C_b b/(2h)$ (bed friction coefficients C_b=0.00084, 0.0017, and 0.0034 with constant water depth) are tested to quantify the stabilizing effect of bed friction. Figure 5.11 reveals the asymmetric moment with different bed frictions. It indicates that the asymmetry in the flow field becomes weaker as the bed friction increases. When the bed friction increases, flow velocity is slower and then the flow pattern becomes less asymmetric. However, the reattachment length becomes longer as the bed friction increases as Figure 5.12 shows. In addition, the effect of bed friction on asymmetry seems not to be strong at least in the range of C_b =0.00084~0.0034 investigated. The asymmetry of flow is disadvantageous in most of engineering applications. Consequently, it seems reasonable that bed roughness adjustment offers an opportunity to reduce such disadvantage associated with the similar structure in hydraulic engineering.

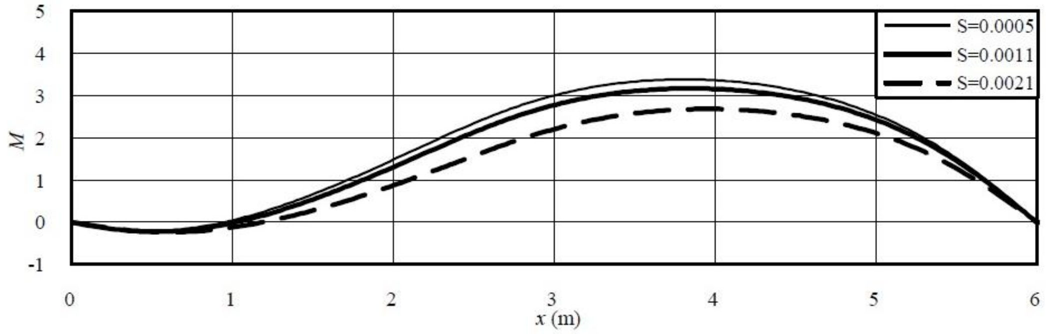

Figure 5.11 Asymmetrical moment distribution for different parameter S_t ($S_t = C_b b/(2h)$).

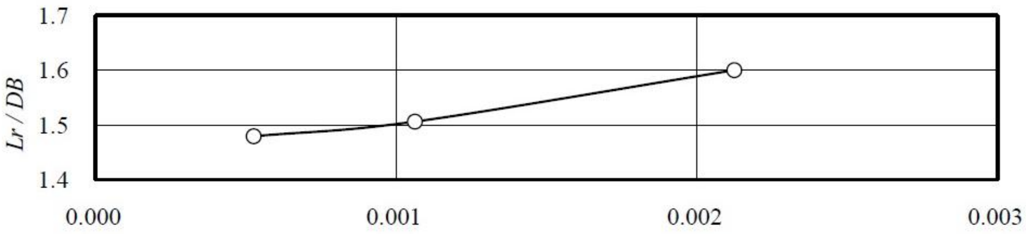

S_t

Figure 5.12 Reattachment length for different parameter S_t.

5.1.7 Conclusions

The lattice Boltzmann model has been applied to model the free surface flows in rectangular shallow basins and the following conclusions can be drawn:

The results obtained by the LABSWE^{TM} have been compared to those by finite volume and algebraic turbulence models and laboratory experiments. The results show that the lattice Boltzmann model can predict asymmetrical shallow flows and capture the typical features efficiently at the same accuracy as the conventional methods.

The effect of the Froude number and bed friction on flow stability and reattachment length has been studied. Research indicates that the asymmetry of flow becomes weaker but reattachment length becomes longer with the increase of the Froude number. Bed friction has a similar effect. However, these results may be valid only for the above range of inlet Froude numbers and bed friction values considered. Out of this range, the flow regimes may be different, which needs further research.

5.2 Shallow Water Flows over Discontinuous Beds

5.2.1 Introduction

In this chapter, numerical modelling of shallow water flows over discontinuous beds is presented. The flows are simulated by LABSWE^{MRT}. The weighted centred scheme for force term together with the bed height for a bed slope described in section 3.9.2 is used to improve simulation of flows over discontinuous bed. Furthermore, the resistance stress is added to include the flow head loss caused by a step. Three test cases: 1D tidal and dam-break flows, and 2D shallow water flow over a square block, are considered to verify the present method.

5.2.2 Background

Shallow water equations have been widely used to simulate flows in rivers, channels, coastal seas, estuaries and harbours [3]. Although the assumption of continuous change in bed elevation is used in the shallow water equations, the equations have been applied successfully to simulating flows over discontinuous beds. Zhou et al. [156] extended the surface gradient method [157] to shallow water flow over discontinuous bed topography and obtained satisfactory results. Erduran et al. [158] introduced a new algorithm based on the finite volume method for a solution to the equations with a step in beds. Črnjarić-Žic et al. [159] applied the finite volume WENO and central WENO schemes to solve the one-dimensional shallow water equations with discontinuous riverbed and some errors in water depth have been found. Bernetti et al. [160] presented the exact solution of the Riemann Problem for the shallow water equations with discontinuous bed topography. Rosatti and Begnudelli [161] investigated the Riemann Problem for one-dimensional shallow water equations involving a bed discontinuity. They further applied a finite-volume Godunov-type with predictor and corrector steps for an accurate solution. The method has been tested using a few flow cases and agreed well with the analytical solutions. Kesserwani and Liang [162] proposed a conservative high-order discontinuous Galerkin method for one-dimensional shallow water equations with arbitrary topography. Cozzolino et al. [163] discussed the shallow-water equations with discontinuous bed and proposed a first-order accurate numerical scheme to capture contact discontinuities at channel bed with steps. The tests demonstrate the feasibility of the scheme for simulating flows over continuous and discontinuous beds. However, most of the above schemes reported in literature are developed and tested only for one-dimensional flow problems.

5.2.3 Numerical Case Studies

5.2.3.1 Case1: A Tidal Flow over Steps

The first case is a tidal flow over a step which has been tested by Goutal and Maurel [164]. The layout is shown in Fig. 5.14 and the step is 8m high. The bed profile is defined by

$$z_b(x) = \begin{cases} 8 & if \left|x - \frac{1500}{2}\right| \le \frac{1500}{8} \\ 0 & otherwise \end{cases} \tag{5.1}$$

The total length is 1500m. The initial and boundary condition are as follows:

$$H(0) = 16\ m, \text{ L=1500 m.} \tag{5.2}$$

$$u(x,0) = 0 \tag{5.3}$$

$$h(x,0) = H(0) - z_b(x) \tag{5.4}$$

$$u(L,t) = 0 \tag{5.5}$$

$$h(0,t) = H(0) + 4 - 4\sin\left[\pi\left(\frac{4t}{86400} + \frac{1}{2}\right)\right] \tag{5.6}$$

The asymptotic analytical solution is presented by Bermudez and Vázquez [165]

$$h(x,t) = H(x) + 4 - 4\sin\left[\pi\left(\frac{4t}{86400} + \frac{1}{2}\right)\right] \tag{5.7}$$

$$u(x,t) = \frac{(x-L)\pi}{5400h(x,t)}\cos\left[\pi\left(\frac{4t}{86400} + \frac{1}{2}\right)\right] \tag{5.8}$$

In computation, 200 grids are used and space step Δx=7.5m, time step Δt=0.1s, C_b=0.0, and s_7=s_8=1/0.8. The relaxation parameters from s_0 to s_6 are equal to 1. The calculated water velocity and water depth has been compared with the analytical solution in Figures 5.13 and 5.14 at time T=10800s. It can be seen that the agreement is excellent and this shows that the proposed method can predict the flow over a vertical step accurately.

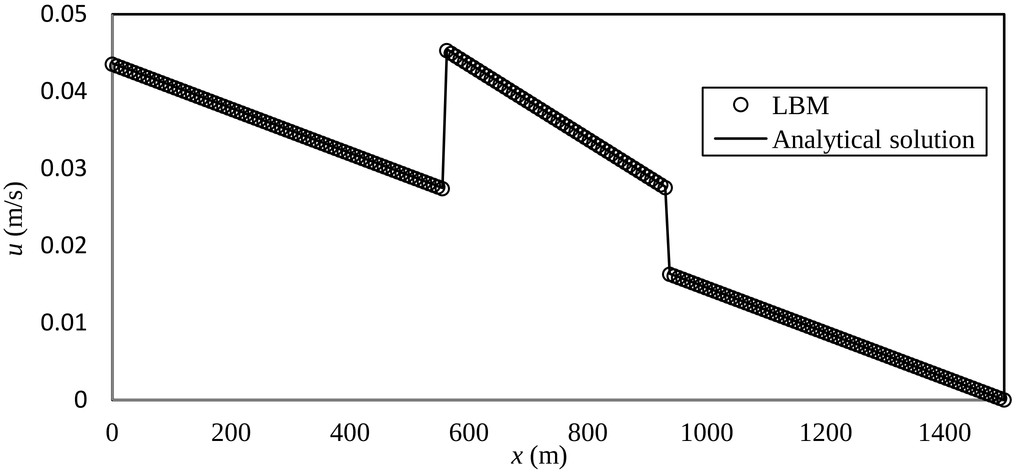

Figure 5.13 Velocity at T=10800s.

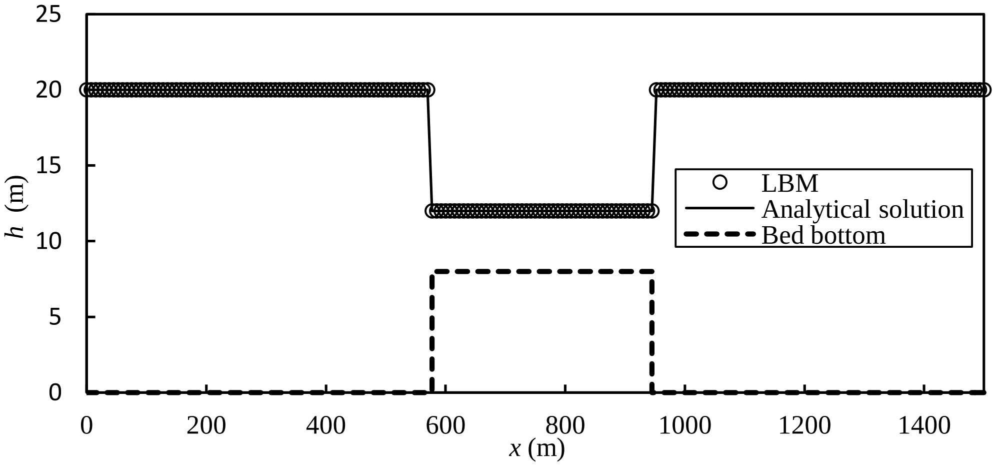

Figure 5.14 Water depth at T=10800s.

5.2.3.2 Case2: Dam-break Flow

The dam-break flow case tested by Rosatti and Begnudelli [161] is used to verify the proposed model. It flows on a wet bed with a step shown in Figure 5.16. The initial flow velocity is zero; the water depth on the left hand side of the step is 5m and on the right hand side is 0.9966m; and the step height is 1m. The flow is unsteady. 2000 grids are used in the computation with Δt = 0.01s, Δx = 1m, s_7=s_8=1/0.51, s_0 -s_6=1 and C_b=0. The simulated water velocity and water surface elevation are shown in Figs. 5.15 and 5.16, from which it can be seen that the LBM can capture the shock wave accurately although there is a little disagreement at the wave front.

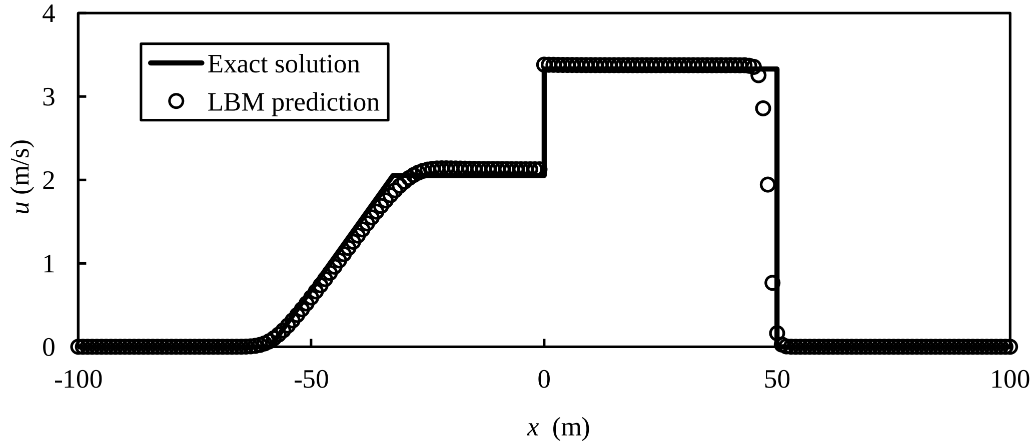

Figure 5.15 Water velocity at T=8s.

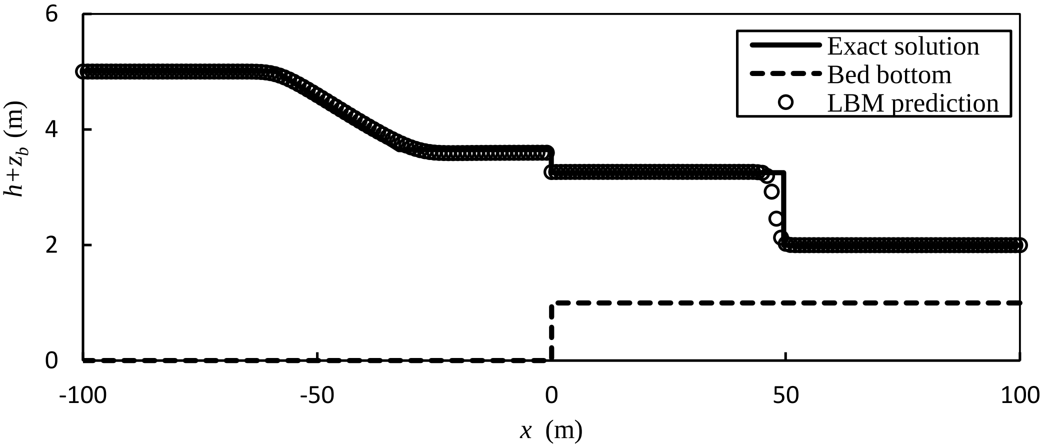

Figure 5.16 Water surface at T=8s.

5.2.3.3 Case3: Flow over a Square Block

A local head loss will happen when flow passes over a step and Zhou et al. [156] modified the shallow water equations by including the resistance stress. In the present study, this idea has been adopted for including the head loss caused by a step. The resistance stresses are defined by $\tau_{sx} = \rho c_x u\sqrt{u^2 + v^2}$, and $\tau_{sy} = \rho c_y v\sqrt{u^2 + v^2}$, in which, c_x and c_y are the empirical factor for the local head loss in x and y directions, respectively, and they are calculated from $c_x = 0.5\frac{[h(x,y)-h(x+1,y)]}{h(x,y)}$ and $c_y = 0.5\frac{[h(x,y+1)-h(x,y)]}{h(x,y)}$. In order to identify the effect of head loss, one-dimensional flow is calculated firstly. Figure 5.17 shows the difference between the results with and without the head loss. It is clear that it is more reasonable to include the effect of head loss.

Furthermore, the two-dimensional flow in a channel with a submerged square block is simulated. The block has height of 0.1m with horizontal dimensions of 0.7m × 0.7m and is located in the center of the channel. The channel is 2m wide and 5m long, which is shown in Figure 5.18. In the computation, 50 × 20 grids are used; Δt=0.01s and Δx=Δy=0.1m; and s_7=s_8=1/0.8, s_0-s_6=1. For the boundary conditions, the constant discharge is specified at inlet and water depth h_0 at outlet. First of all, a static flow is tested, and then a steady flow is simulated. Figures 5.19 and 5.20 show the calculated water profile and discharge at T=500s for static flow with outlet water depth of h_0=0.2m with improved force term (As described in section 3.9.2 and it is represented by with weights in Figs. 5.19 and 5.20) and without improved force term (It is represented by without weights in Figs. 5.19 and 5.20). The results indicate that the proposed method in section 3.9.2 can produce accurate solution, satisfying the $\mathscr{N}$-property numerically [3]. Furthermore, the effect of weights has been studied. From Figs. 5.19 and 5.20, it can be seen that significant errors occurred if weights is not included in the force term. Therefore, including weights in the force term is crucial to obtain accurate results in this case.

After the static test, the discharge Q_0=0.04m^3/s is specified at inlet and water depth h_0=0.2m at outlet. Figure 5.21 shows the numerical discharge after the flow reaches steady state, indicating that the MRT-LBM model can retain the correct constant discharge for the steady flow over a two dimensional submerged block. Figure 5.22 shows the water surface profiles simulated for the flow and the further comparison between 1D and 2D results have been plotted in Figure 5.23. It can be seen that the water depth difference between upstream and downstream in 2D is smaller than that in 1D due to the reason that the 2D flow will slightly be diverged by the submerged block from the channel centerline to sides. Overall, the proposed model produces good results for 1D and 2D cases.

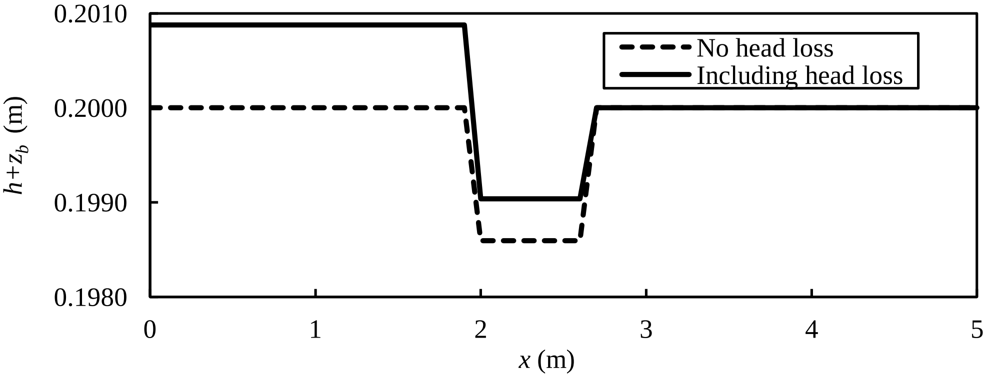

Figure 5.17 Comparison of water surface profiles with and without head loss for 1D case.

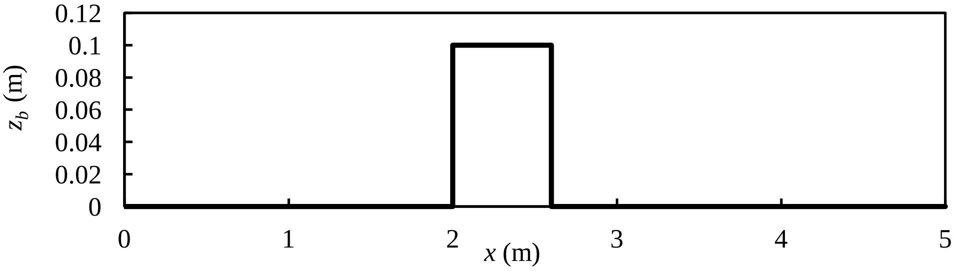

Figure 5.18 Bottom profile for 2D case (side view).

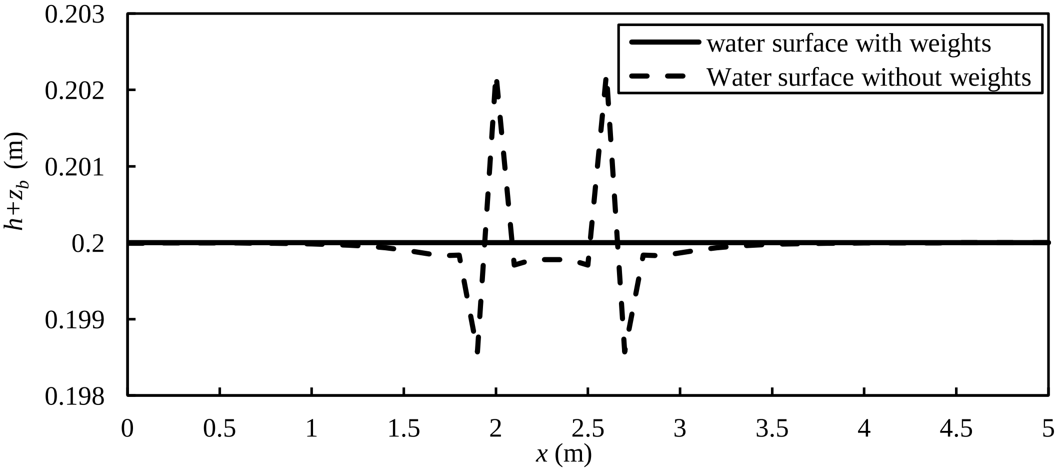

Figure 5.19 Water surface for static flow.

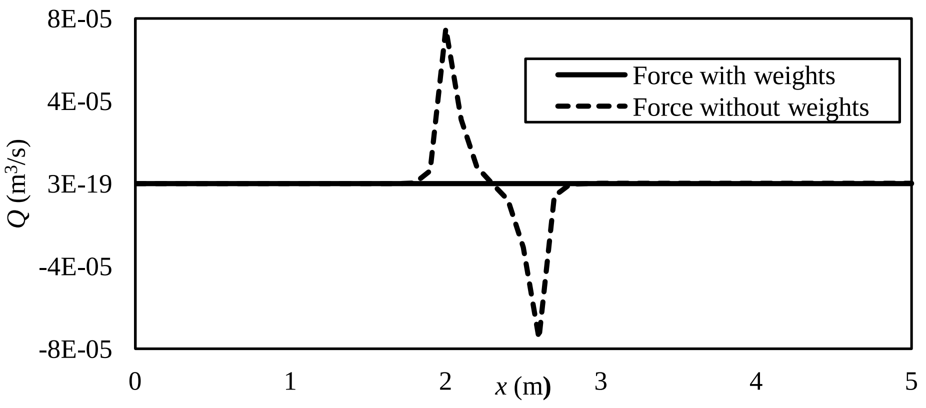

Figure 5.20 Discharge for static flow.

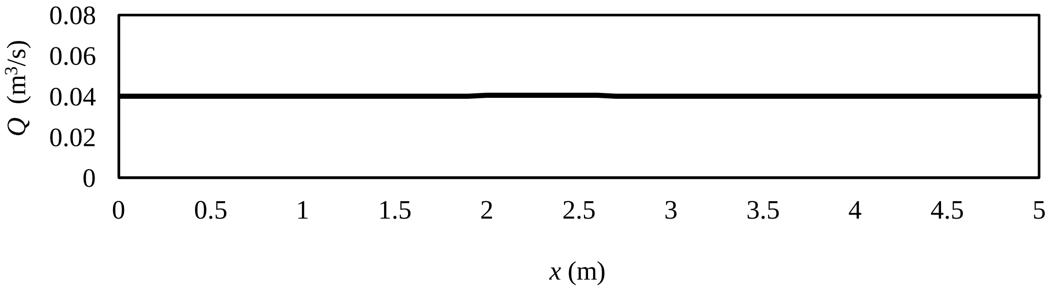

Figure 5.21 Discharge for 2D steady flow.

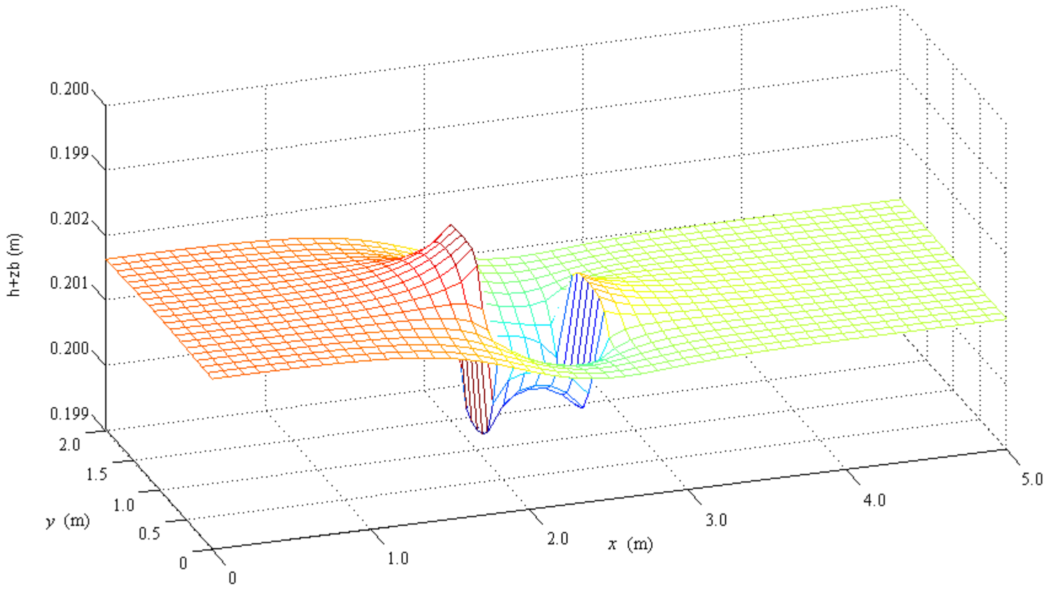

Figure 5.22 Predicted water surface by MRT-LBM.

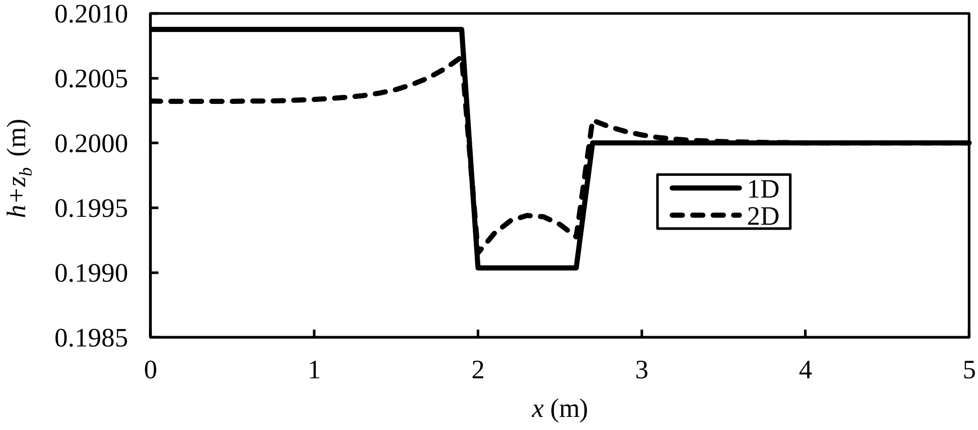

Figure 5.23 Comparison of centerline water surface profiles between 1D and 2D.

5.2.4 Conclusions

The lattice Boltzmann method has been applied to simulate the shallow water equations with discontinuous beds. The flow equations are solved using the multiple-relaxation-time lattice Boltzmann equation on D2Q9. Unlike other numerical method, no additional treatment is needed in the described method for flows over a bed with a vertical step. Three typical test cases including a two dimensional flow are predicted to verify the model. The results agree well with the analytical solutions. The conclusions can be drawn as follows:

(a) The force term in the lattice Boltzmann model is improved by inluding the weights and it is demonstated that it is crucial to produce the correct results.

(b) In order to include the head loss caused by a step, the resistance stress is added in the force term. The study shows that the calculated results with resistance stress are more practical.

(c) The proposed method is verified by three cases and the study shows that it is simple and accurate. Therefore it can be used for shallow flows over a discontineous beds in hydraulic engineering.

Chapter 6: Application of LABSWE^{MRT} for Simulating the Moving Body

---

6.1 Introduction

In this chapter, LABSWE^{MRT} is extended into simulating a moving body in shallow waters. Three different schemes for a curved boundary condition are used and compared in detail. In order to deal with the moving body boundary, certain momentum is added to reflect interaction between the fluid and the solid and a refill method for new wetted nodes moving out from solid nodes is proposed. The described method is applied to simulate static and moving cylinders in shallow water flows.

6.2 Background

Shallow water equations can be used to describe tidal flows, tsunami, and landslides into water, ship movement, and beach erosion. Some of these flows further involve a moving body and simulating such flows using a numerical method attracts researchers' attention [166-168].

In lattice Boltzmann method, the most popular treatment of boundary condition is the bounce-back scheme. Although it can be used for a curved boundary, it is only first-order accurate except that the boundary is located at the middle of two grid lines, which is awkward for a curved boundary. In order for treating curved boundaries at higher-order accuracy, Bouzidi at al. [107] developed a scheme using bounce-back and spatial interpolations; Filippova and Hanel [90] proposed another second-order accurate boundary condition in which its stability was improved by Mei et al. [169]; and Guo et al. [170] proposed a non-equilibrium extrapolation method for a curved boundary. Recently, Verschaeve and Muller [171] proposed a no-slip curved boundary condition that is based on a reconstruction of the populations from the density, velocity and the rate of strain. For shallow water, Liu et al. [56] proposed a second-order boundary for no-slip, semi-slip and slip boundaries. As discussed in section 1.5.7, the moving boundary for Navier-Stokes equations using the lattice Boltzmann method has been studied by Lallemand and Luo [105] and Kao and Yang [106].

To the writer’s knowledge, very little study on moving body in shallow waters has been reported in the literature except for one paper by Causon et al. [168]. They applied a Godunov-type finite volume method with the cut cell technique for the moving body. The main drawback is that the scheme is complex and inefficient for a large-scale problem. Our ultimate goal is to develop a simple and efficient LBM for simulating practical shallow water flows involving moving body produced by landslides as indicated in the references [172-175]. The present study is the first step, which focuses on development of the model and its verification using both static and moving cylinders. Despite a simple shape, flows around static and especially moving cylinders contain all possible complex curved boundaries encountered in practice; hence they are the suitable test cases for the study. In the next step, the developed LBM will be applied to simulate the real life problems. Consequently, in this study as the first step, LABSWE^{MRT} for a moving boundary in shallow water flow is developed. The model is used to predict static and moving cylinders in shallow waters and the results are compared with the corresponding experimental measurements.

6.3 Boundary Conditions

In the lattice Boltzmann method, the boundary conditions play an important role in the accuracy of the simulation. For steady flow, a constant discharge is defined at inflow boundaries, and a water depth is specified at outlet and slip boundaries are used for side walls [3].

At a curved boundary sketched in Figure 6.1, if fluid nodes and solid nodes are represented by respective hollow and solid dots, the following three different methods are considered in the study. According to Filippova and Hanel (FH’s scheme) [90]: the unknown distribution function streaming back from the solid can be presented as

$$\tilde{f}_{\bar{\alpha}}(x_f, t+\Delta t) = (1-\chi)\,\tilde{f}_{\alpha}(x_f, t) + \chi\, f_{\alpha}^{(*)}(x_b, t) + 2\omega_{\alpha} h \frac{3}{e^2} e_{\bar{\alpha}}.u_w \tag{6.1}$$

u_w is the velocity vector of a moving body; χ is a weighting factor given by Eqs. (6.3) and (6.4); and $f_\alpha^{(*)}(x_b,t)$ is the fictitious equilibrium distribution function at solid node x_b, which can be calculated by

$$f_\alpha^{(*)}(x_b,t)=\omega_\alpha\left[\frac{3gh(f,t)}{2e^2}+\frac{3}{e^2}e_{\alpha i}u_i(x_b,t)+\frac{9}{2e^4}e_{\alpha i}e_{\alpha j}u_i(x_f,t)u_j(x_f,t)-\frac{3}{2e^2}u_i(x_f,t)u_i(x_f,t)\right]$$
$$h(x_f,t),\ \alpha=1\sim 8 \tag{6.2}$$

in which, $\omega_\alpha=\begin{cases}4/9, & \alpha=0\\ 1/9, & \alpha=1,3,5,7\\ 1/36, & \alpha=2,4,6,8\end{cases}$; $u_i(x_b,t)=u_{bi}$ is the fictitious velocity component at solid node *b* in *i* direction shown in Figure 6.1 and calculated as

$$u_{bi}=u_{fi}\ \text{ and }\ \chi=(2\varDelta-1)/(\tau-1)\ \text{ when }\ \varDelta<\frac{1}{2} \tag{6.3}$$

$$u_{bi}=\frac{(\varDelta-1)u_{fi}}{\varDelta}+\frac{u_{wi}}{\varDelta}\ \text{ and }\ \chi=(2\varDelta-1)/\tau\ \text{ when }\ \varDelta\geq\frac{1}{2} \tag{6.4}$$

In the above equations, $u_{fi}=u_i(x_f,t)$; $\varDelta=\dfrac{|x_f-x_w|}{|x_f-x_b|}$ (see Figure 6.1); and u_{wi} is the velocity component of the moving body in *i* direction.

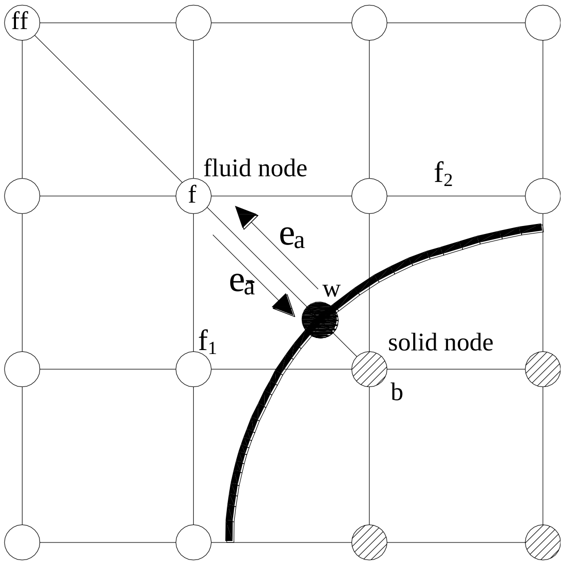

Figure 6.1 Layout of curved boundary and lattice nodes.

Bouzidi et al. [107] proposed another second order method for curved boundary which combines the bounce-back scheme and spatial interpolations (MMP's scheme).

$$f_{\bar{\alpha}}(x,t+1)=2\varDelta f_\alpha(x,t)+(1-2\varDelta)f_\alpha(x-e_\alpha,t)\quad \varDelta<\frac{1}{2} \tag{6.5}$$

$$f_{\bar{\alpha}}(x,t+1)=\frac{f_\alpha(x,t)}{2\varDelta}+\frac{(2\varDelta-1)f_\alpha(x,t)}{2\varDelta} \qquad \varDelta\geq\frac{1}{2} \tag{6.6}$$

Guo [170] proposed an extrapolation method for the curved boundary conditions (Guo's scheme). The distribution function at boundary node is decomposed into equilibrium and non-equilibrium parts. The equilibrium part is approximated by a fictitious one and the non-equilibrium part is calculated by extrapolation from the neighbouring fluid nodes.

$$f_\alpha(x,t)=f_\alpha^{eq}(x,t)+f_\alpha^{ne}(x,t) \tag{6.7}$$

$$f_\alpha^{eq}(x_b,t)=\omega_\alpha\left[\frac{3gh(x_f,t)}{2e^2}+\frac{3}{e^2}e_{\alpha i}u_i(x_b,t)+\frac{9}{2e^4}e_{\alpha i}e_{\alpha j}u_i(x_f,t)u_j(x_f,t)-\frac{3}{2e^2}u_i(x_f,t)u_i(x_f,t)\right]$$
$$h(x_f,t)\quad \alpha=1\sim 8 \tag{6.8}$$

$$f_\alpha^{ne}(x_b,t)=f_\alpha^{ne}(x_f,t)\quad \varDelta\geq 0.75 \tag{6.9}$$

$$f_\alpha^{ne}(x_b,t)=\varDelta f_\alpha^{ne}(x_f,t)+(1-\varDelta)f_\alpha^{ne}(x_{ff},t)\quad \varDelta<0.75 \tag{6.10}$$

For a moving curved boundary, one further problem has to be resolved: some solid nodes may move outside the solid region and enter the fluid region; their distribution functions have to be constructed with an appropriate scheme. According to Lallemand and Luo [105] and Kao and Yang [106], there are different methods to refill these unknown distribution functions. For example, one can compute the unknown equilibrium distribution functions for the new fluid nodes which are solid nodes at the last time step by using moving boundary velocity (u_{wx}, u_{wy}) and the average water depth, and use these equilibrium distribution functions for the unknown distribution functions. In addition, the extrapolation method can be used to determine the unknown distribution functions. As all these methods produce similar results [105], the extrapolation method is used in the study.

As seen from Figure 6.1, if assuming that the solid node *b* become a fluid node at the next time step, the velocity and water depth for node *b* at next time step will be calculated as follows:

$$u_b(t+1)=2u_f(t)-u_{ff}(t) \tag{6.11}$$

$$v_b(t+1)=2v_f(t)-v_{ff}(t) \tag{6.12}$$

$$h_b(t+1) = \frac{1}{3}\left[h_f(t) + h_{f_1}(t) + h_{f_2}(t) \right] \tag{6.13}$$

The distribution functions for new fluid node *b* can be determined using the new *u, v*, and *h* from above. The status of the nodes occupied by a moving cylinder may become solid or fluid with time.

In order to simulate the interaction between the fluid and solid, the certain momentum has to be added to a numerical method. Following the idea of Yu et al. [176] for the Navier-Stokes equations, the force term, $6\omega_n \frac{\rho}{e^2}(e_{-n}.u_w)$, can be used to represent such interaction, which is applied to the shallow water equations with the density replaced by the water depth, $6\omega_n \frac{h}{e^2}(e_{-n}.u_w)$, here *n* stands for the outward normal direction.

6.4 Simulation for Stationary Cylinder

The laboratory experiments were performed at the State Key Laboratory of Hydraulics and Mountain River Engineering in Sichuan University, P. R. China. The channel is 0.39m wide and 2m long, made of plexiglass. The roughness coefficient n_f is 0.008 and the bed slope *i* is 0.001. The layout of experiments is shown in Fig. 6.2. The cylinder with the diameter of 0.055m is placed in the centerline of the channel. The cylinder was fixed and the water depth at outlet is controlled by the tail gate. Three different discharges were tested in the experiments for this case. The hydraulic parameters in the experiments are listed in Table 6.1, in which *L* and *B* are the length and width of the channel, respectively. The water depth at the centerline of channel is measured by pulse sensors which have been calibrated before measurement and the measurement precision is 0.1%. In the experiments, the sensors are arranged along the longitudinal centre line of channel at a uniform interval space of 0.02m. To obtain the accurate results, the experiments are repeated several times and the results are plotted in Figures 6.4-6.6.

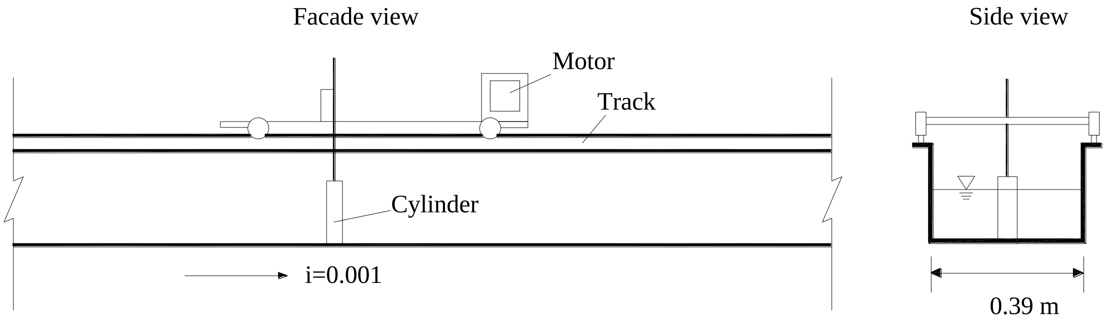

Figure 6.2 Layout of the channel and equipment in the experiments.

Table 6.1. Hydraulic parameters in the experiments.

Case No.	Discharge Q (m^3/s)	Outlet water depth h_0 (m)	Bed slope i	L/B (m/m)	Cylinder velocity U_w (m/s)	Average flow velocity	Froude number	Reynolds number
1	0.0099	0.0905	0.001	2.0/0.39	0	0.28	0.30	134
2	0.0094	0.0625	0.001	2.0/0.39	0	0.39	0.50	186
3	0.0061	0.0965	0.001	2.0/0.39	0	0.16	0.16	76
4	0.00955	0.068	0.001	2.0/0.39	0.062	0.36	0.44	172
5	0.00955	0.1	0.001	2.0/0.39	0.5	0.24	0.24	115

Firstly, the order of convergence of the three schemes is studied. Different grid sizes are used to simulate Case 3 and the results are compared with the corresponding experimental data. The parameter $E1 = \frac{h_{pr}(x_0, y_0) - h_{ex}(x_0, y_0)}{h_{ex}(x_0, y_0)}$ is adopted to evaluate the convergence of model, in which the $h_{pr}(x_0, y_0)$ is calculated water depth by LBM at point (x_0, y_0) which is the first point behind cylinder as indicated in Figure 6.6, and $h_{ex}(x_0, y_0)$ is the experimental water depth at the same point. The results are shown in Figure 6.3 and it indicates that all three schemes are between first- and second-order accurate, among which the convergence rate of FH’s scheme is fastest.

Table 6.2 The relative error E_r for three schemes.

Case No	FH's scheme	Guo's scheme	MMP's scheme
1	0.000469	0.000461	0.000485
2	0.000440	0.000452	0.000423
3	0.000282	0.000277	0.000312
4	0.000242	0.000317	0.000237
5	0.000402	0.001207	0.000393

In order to verify the proposed models, Cases 1-3 were further carried out. In computations, time step Δt=0.002s, Manning coefficient n_b=0.008, spatial size Δx=Δy=0.007m, the relaxation parameters s_7=s_8=1/0.6, s_0-s_6=1, and 250×56 grids are used for Cases 1-3. Normally, the Reynolds number is known before numerical simulation, hence the kinematic viscosity can be calculated, and then the time step, space size, and relaxation parameter can be determined by Equation (1.11).

The predicted water depths for these cases are compared with the experimental data in Figures 6.4-6.6 showing that all schemes produce similar results that agree with experimental results. In order to compare the three schemes quantitatively, the relative error $E_r = \frac{1}{N}\sqrt{\sum_1^N [(h_{pr} - h_{ex})/h_{ex}]^2}$ is used to evaluate accuracy of schemes, in which h_{pr} is water depth predicted by LBM model and h_{ex} is the experimental data, N is the number of experimental data. The relative errors E_r are presented in Table 6.2. From it, for Cases1 and 3, the errors of MMP's scheme are biggest, and for Case 2, it is smallest. Overall, these three schemes produce similar results for static cases although the water depths are underestimated slightly. As there are also errors in the experiments, such results are acceptable.

Furthermore, the velocity vector for Case1 is displayed in Figure 6.7. It shows that the flow velocity around the cylinder is very small and this is due to the no-slip curved boundary conditions for cylinder. In the downstream of cylinder, a small low velocity region is formed, which is consistent with the experiments. In general, the proposed models can provide accurate results for flows around static cylinders.

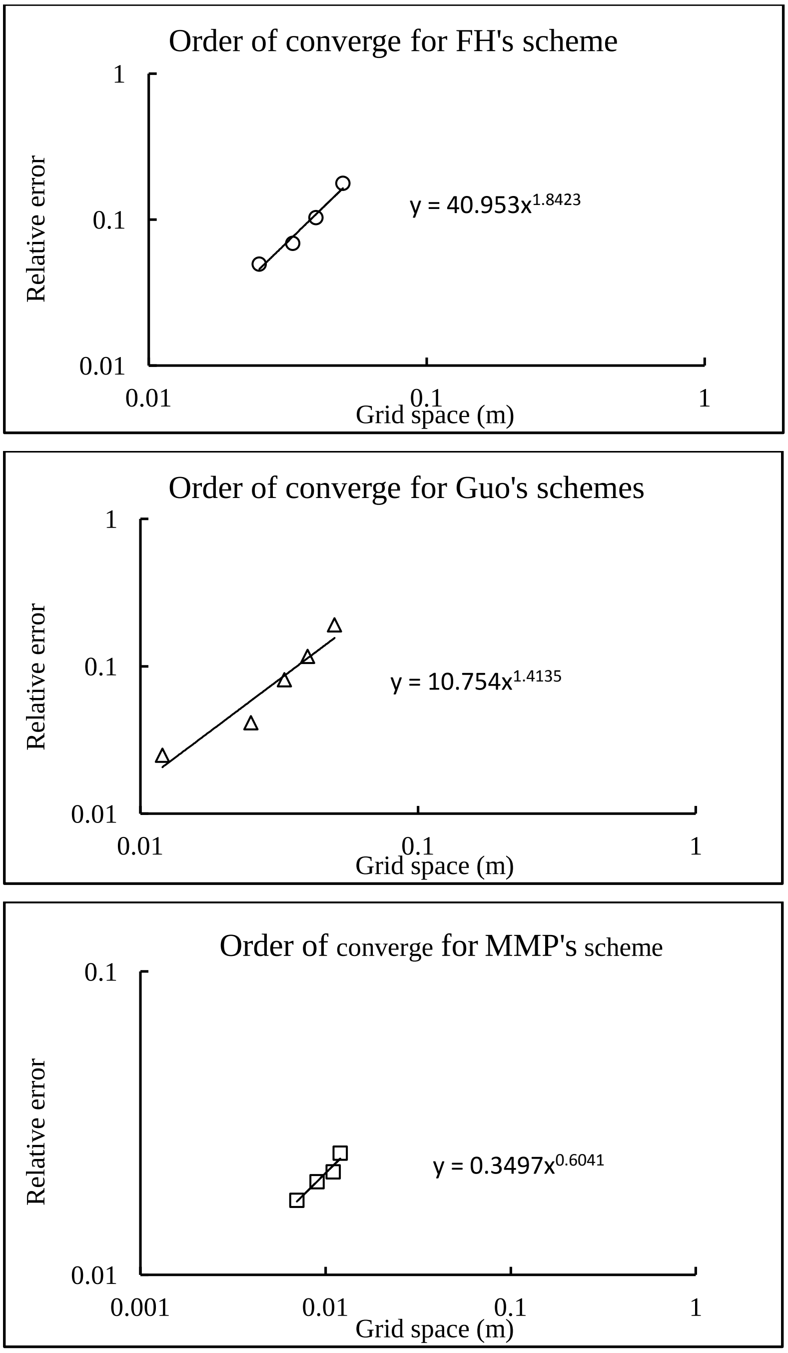

Figure 6.3 Convergence of the three schemes.

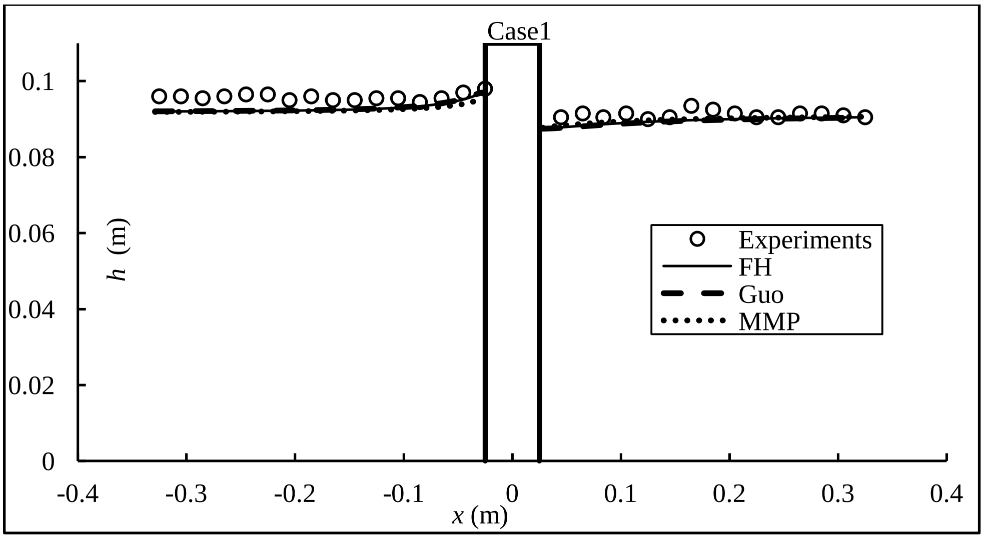

Figure 6.4 Water depth along the centerline for Case 1.

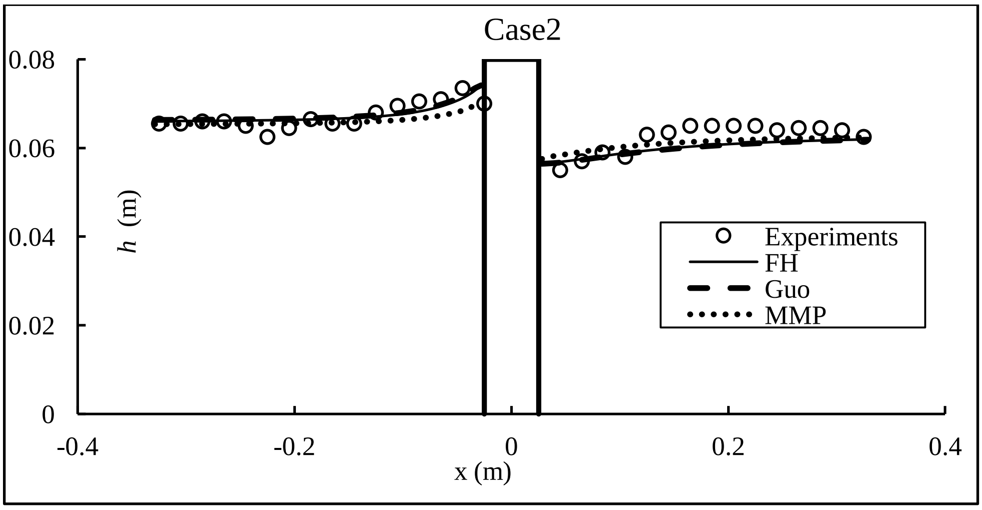

Figure 6.5 Water depth along the centerline for Case 2.

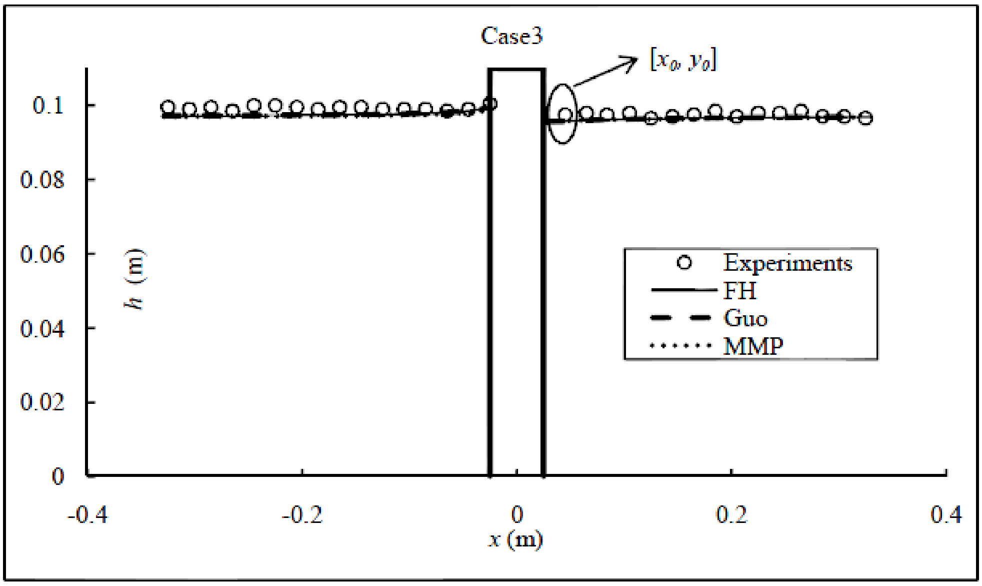

Figure 6.6 Water depth along the centerline for Case 3.

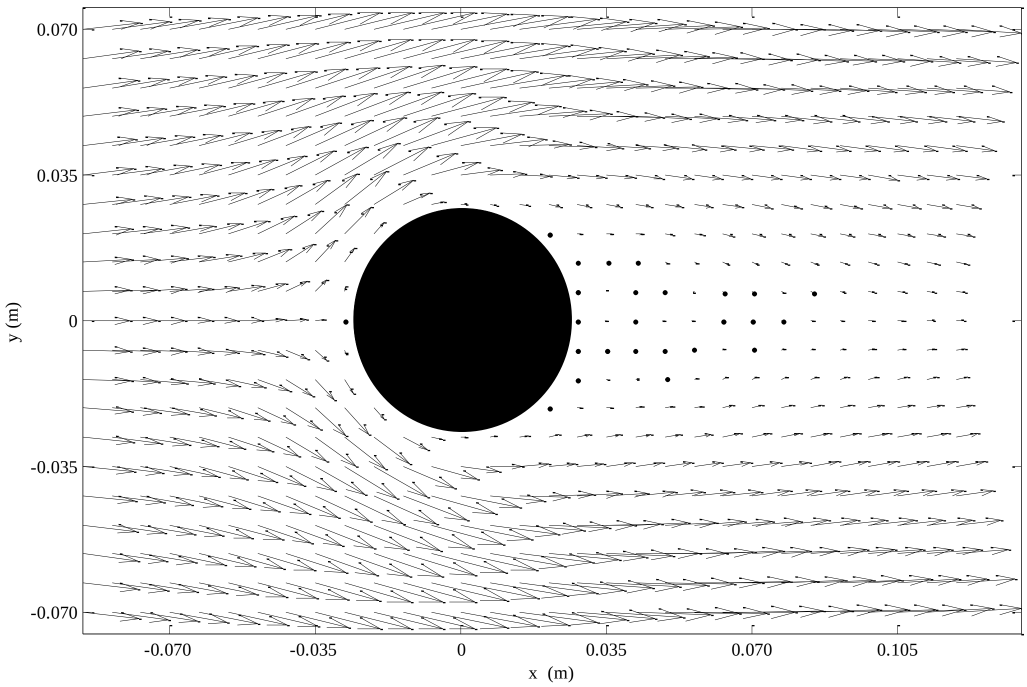

Figure 6.7 Velocity vector for case 1 with FH's scheme.

6.5 Numerical Simulation for a Moving Cylinder

The experiments for a moving cylinder were also carried out in the same laboratory flume (See Figure 6.2). In the experiments, when the flow becomes steady for the static cylinder, it is dragged by the motor and begins to move forward along the centerline of the channel uniformly. After its moving, the measurement is carried out. Two different velocities u_w (For all cases, cylinder moves only along x direction, so $u_w=u_{wx}$) for the cylinder movement were considered. The first one was 0.062 m/s that was smaller than the average flow velocity in the channel, and the second was 0.5 m/s that was larger than the average flow velocity. It should be noted that the cylinder moves only along the x direction. The experiments were repeated several times for more accurate results.

On the other hand, the numerical simulation has been carried out by LBM and the mesh layout is the same as the cases for the static cylinder. In addition, the other computation parameters are the same as the cases for the static cylinder except the velocity of moving cylinder. The performances of FH's, MMP's and Guo's schemes are compared for the centerline water depths in Figures 6.8 and 6.9. All schemes provide reasonable results for Case 4. But for Case 5 it is clear that Guo's scheme produces an obviously bigger drop between upstream and downstream of the cylinder than other two schemes as shown in Figure 6.9, which is inconsistent with the experiments. In order to analyze quantitatively, the relative error E_r is used to assess the schemes. Table 6.2 indicates that the errors of MMP's scheme for Cases 4 and 5 are smallest, indicating that MMP's scheme is the best for simulating the moving boundary among the three schemes. Still, the difference between MMP's and FH's schemes is relatively small. However, the relative error E_r for Guo' scheme is bigger than other two schemes especially for Case 5 in which its errors is about three times of either MMP's or FH's errors. As a result, both of FH's and MMP's schemes are better than Guo's schemes for moving boundary problems in shallow water flows.

Figure 6.10 shows water depths at different times using FH's scheme. As the cylinder moves at a smaller velocity of 0.062 m/s than the average flow velocity, the flow pattern is similar to that for a static cylinder and that is again consistent with the experiments. In order to study the effect of the moving cylinder, one more case is considered in which the flow parameters are the same as Case 5 except that the cylinder velocity moves at u_w= 0.1 m/s. Fig. 6.11 shows the predicted water depths along the centerline for the moving cylinder at different velocities. It can be seen that the difference in water depths between the upstream and downstream of the cylinder reduces with u_w=0.1m/s comparing with that at u_w=0; inversely, it increases with u_w= 0.5m/s. This is again consistent with the experiments and also demonstrates that the interaction between the fluid and solid is correctly determined in the model. In addition, to the writer's knowledge, few experimental data for shallow water flows involving a moving body are available in the literatures, and hence the present experimental measurements provide valuable data that may be used to verify other numerical methods.

In all the simulation, it takes about 20000 iterations to obtain a steady flow for a typical case. The computational times for MMP's, FH's and Guo's schemes are 1.27, 1.8, and 2 hours, respectively on an ordinary desktop PC that is composed of Intel Core2 Duo CPU E8400 with 3.00GHz and 3.50GB RAM. This suggests that MMP's scheme is most efficient.

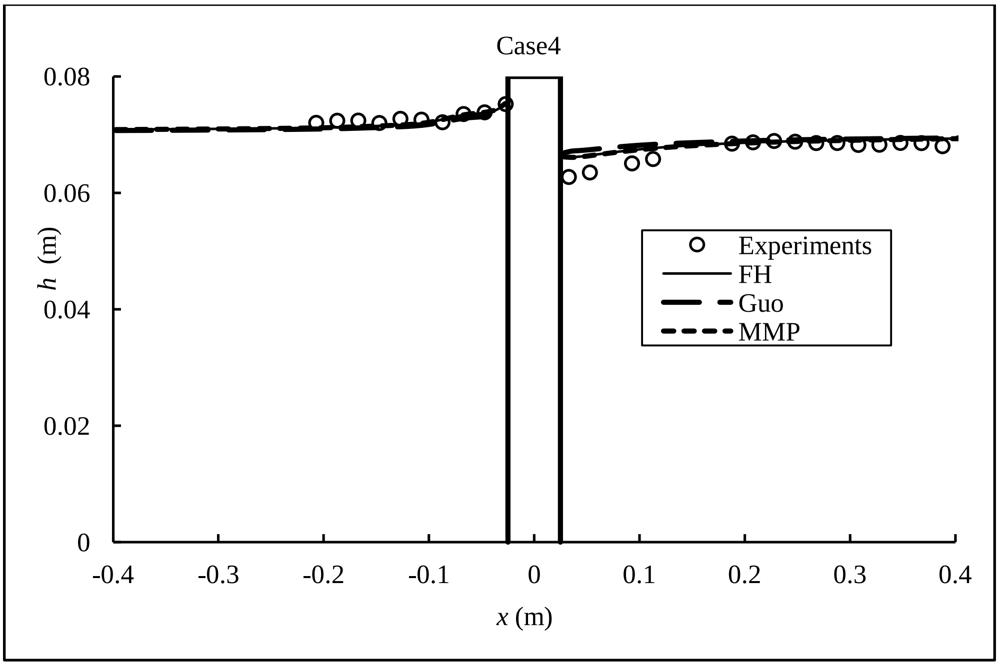

Figure 6.8 Water depths at *t*=12s for moving cylinder for case 4.

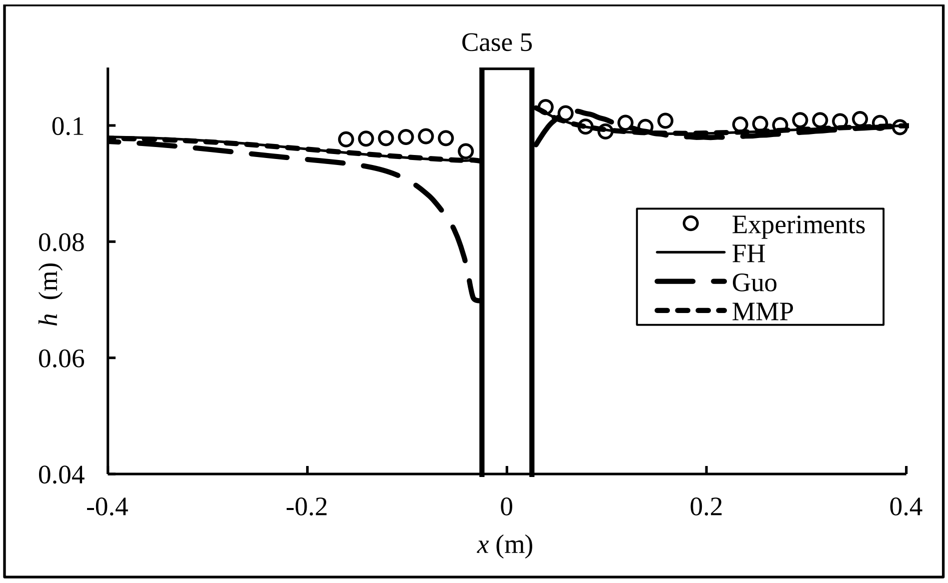

Figure 6.9 Water depths at *t*=2s for moving cylinder for case 5.

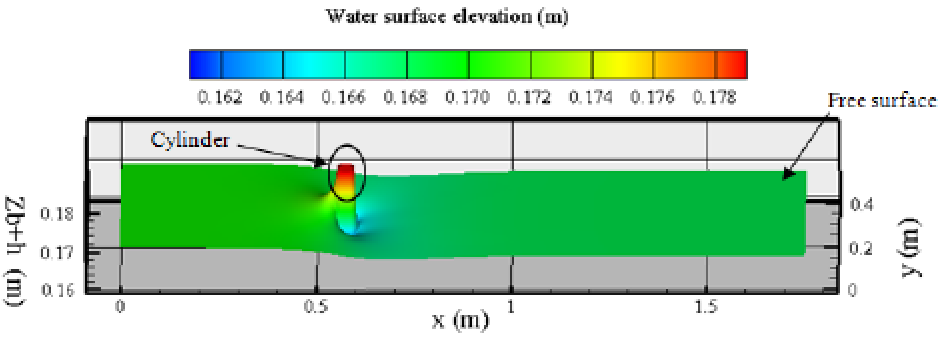

(a) t=4s

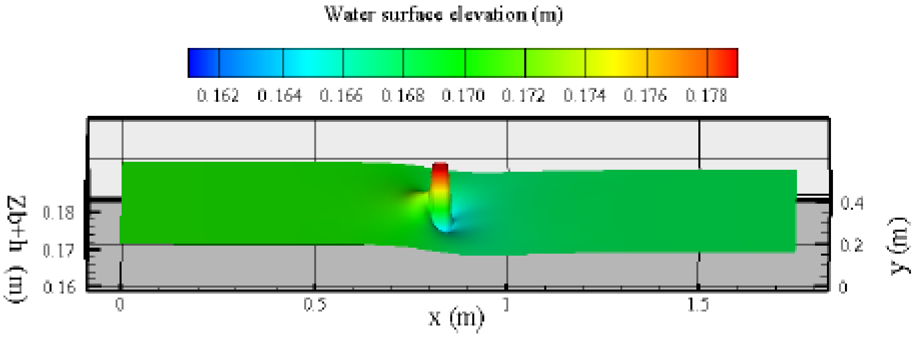

(b) t=8s

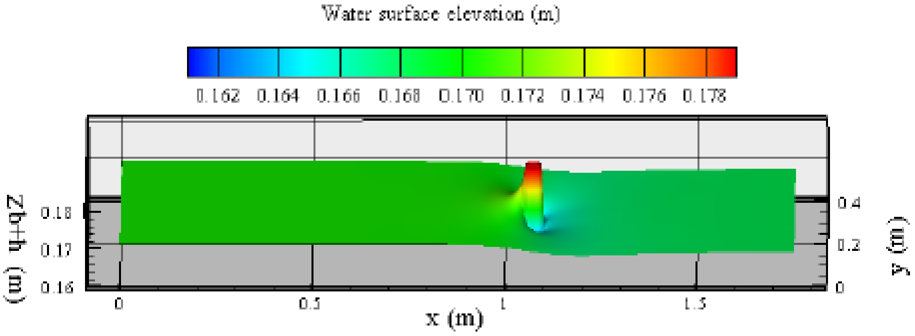

(c) t=12s

Figure 6.10 Water depths at different time for case 4 with FH's scheme (*t*=4s (a), 8s (b), and 12s (c)).

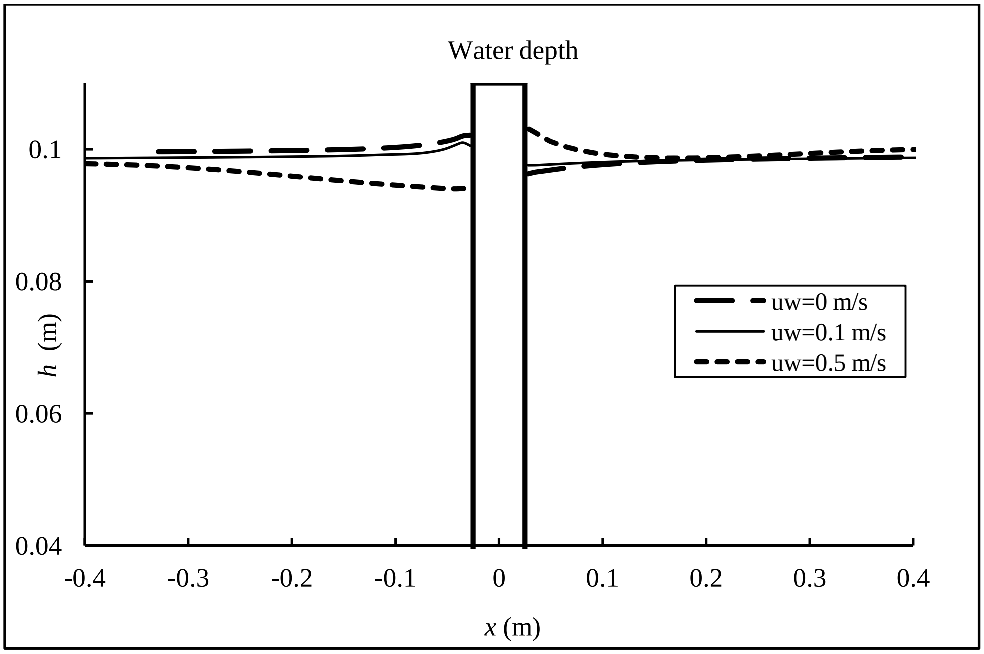

Figure 6.11 Water depths at centerline with u_w= 0, 0.1 and 0.5 m/s with MMP's scheme at same position.

6.6 Conclusions

In this chapter, a lattice Boltzmann method for moving boundary conditions is developed for shallow water flows and is verified by the corresponding experiments. The multiple-relaxation-time is adopted for better stability. The additional momentum for correct interaction between the fluid and solid has been added to the model and a refill method for new fluid nodes moving out from solid nodes has been proposed. Moreover, FH's, MMP's, and Guo's schemes for curved boundary conditions at second-order accuracy have been compared in detail. The proposed model is applied to simulate the flow fields around static and moving cylinders. All three schemes produced similar results tha agree with the experimental data for the static cylinder. However, Guo's scheme produced unreasonable results when it is used to simulate the cylinder moving faster than the average flow velocity in the channel. Satisfactory results are obtained using FH's and MMP's schemes for flows with both static and moving cylinders, in which, MMP's scheme performs better than FH's scheme. The proposed modelling approach is simple and efficient, and can be applied to simulate both static and moving bodies in shallow water flows.

Chapter 7 Application of LABSWE and LABSWE^{MRT} to Environmental Flows

---

7.1 Introduction

In this chapter, the lattice Boltzmann method is used to investigate the solute transport in shallow water flows. Shallow water equations are solved using LABSWE and LABSWE^{MRT}, and the advection-diffusion equation is also solved with a BGK-LBM on a D2Q5 lattice. Three cases: open channel flow with side discharge, shallow recirculation flow and flow in a harbour are simulated to verify the described methods. Furthermore, the performance of LABSWE and LABSWE^{MRT} for these three cases has been investigated.

7.2 Background

Prediction of solute transport in the shallow waters such as distribution of pollution concentration and transport of suspended sediments is important in environmental engineering and attract much attention as indicated in chapter 1[6, 7, 9, 10, 177, 178].

7.3 Boundary Conditions

In the following cases, constant discharge and specified water depth is used at inlet and outlet boundaries. Slip and semi-slip boundaries are used for side walls [3]. For solute transport, the bounce-back boundary in section 4.2.1 is adopted at the wall and zero-gradient boundary conditions in section 4.3 are imposed at the outlet. Constant concentration is specified at the inlet.

7.4 Numerical Case Studies

Case 1: Side Discharge

Side discharge has attracted great interest from environmental engineers as it is a common form of wastewater discharge into a river, and has been investigated by many researchers through numerical and experimental studies. Mikhail et al. [179] measured the width and length of the recirculation eddy for different ratios of jet velocity to main channel velocity from 1 to 22 and of jet width to main channel width from 0.01 to 0.1. Using these experimental conditions, McGuirk and Rodi [114] applied a finite volume shallow water model with $k-\varepsilon$ turbulence closure to simulate the flow and temperature of the side discharges into the open-channel flow. Wang and Cheng [180] simulated the three-dimensional side discharge into a cross channel flow using FLUENT 4.4 and proposed correlation formulas for recirculation length and width. FLOW-3D was also used to study the buoyant flow and mixing characteristics of hot water discharge from the surface and submerged side outfalls in shallow and deep water with a cross flow by Kim and Cho in [181].

From the present study, Figures 7.1 and 7.2 show part of the computed velocity fields and streamlines by LABSWE^{MRT} for Case 1 specified in Table 7.1. It is seen that downstream of the side discharge, a recirculation is formed because of the velocity in the main channel. The recirculation parameters (length L and height H in Figure 7.1) are governed mainly by the ratio of discharge momentum to main channel momentum, where momentum flux ratio M_1 is defined by $M_1 = (V/U)^2\, b/B$ [114].

In order to compare with the experiments of Mikhail et al. [179], the following hydraulic parameters are adopted (see Table 7.1), in which b is side discharge width, B is the main channel width, h_0 is the water depth at outlet, L is the main channel length, U is the velocity in the main channel, V is the side discharge velocity. In computation for velocity fields, Δt=0.01s, C_b=0.01, Δx=Δy=0.016m, s_7=s_8=1.992032 and 842×43 grids are used for Cases 1-5, while Δt=0.02s, C_b=0.001, s_7=s_8=1.953125, Δx=Δy=0.02m and 119×291 grids for Case 6. The relaxation parameters from s_0 to s_6 are equal to 1 and the relaxation time τ_1 in Eq. (3.169) is also equal to 1 for all cases in Table 7.1. The slip boundary condition is applied to the wall boundary. Temperature fields are calculated for Case 6 and the same grid settings are employed for velocity fields. In addition, λ_x=λ_y=0.008, D_x=D_y=0.00008 m^2/s, Δt=0.02s. The temperature of the discharged hot water $DT_0=1$ is specified at the side discharge inlet and the ambient temperature in the main channel flow is zero.

Table 7.1 Channel and Flow Parameters for Side Discharge Flow.

Case	U (m/s)	V (m/s)	b (m)	B (m)	L (m)	h_0 (m)	M_1
1	0.01	0.010	0.064	0.608	13.472	0.051	0.105
2	0.01	0.037	0.064	0.608	13.472	0.051	1.441
3	0.01	0.058	0.064	0.608	13.472	0.051	3.517
4	0.01	0.078	0.064	0.608	13.472	0.051	6.404
5	0.01	0.100	0.064	0.608	13.472	0.051	10.526
6	0.01	0.0201	0.06	5.72	2.38	0.051	0.042

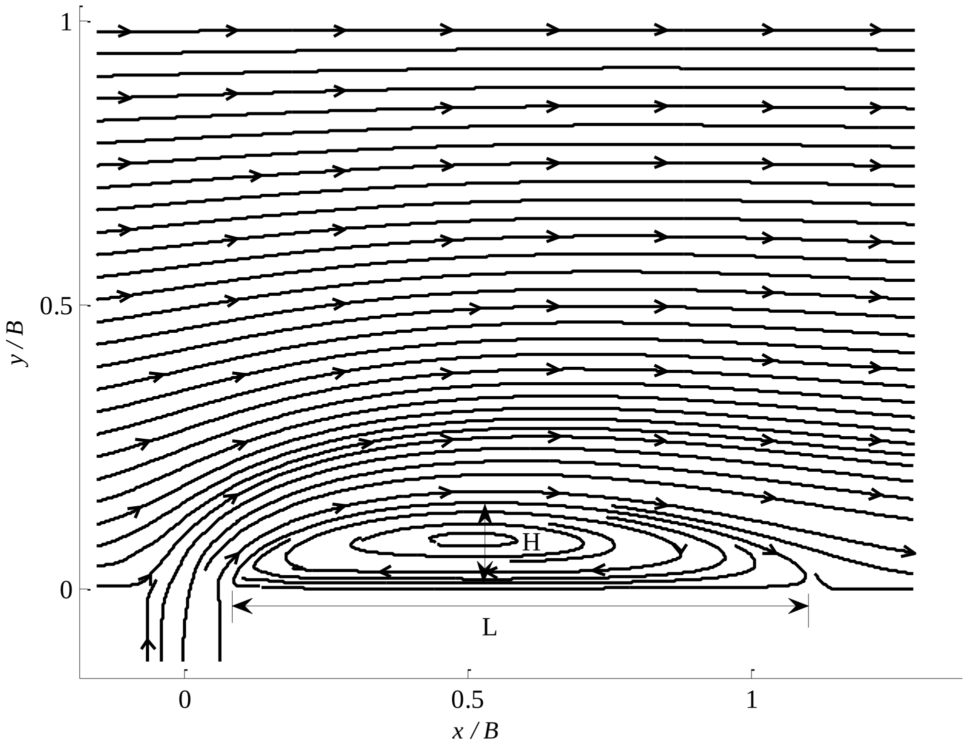

Figure 7.1 Predicted streamlines for M_1=0.105 by LABSWE^{MRT}.

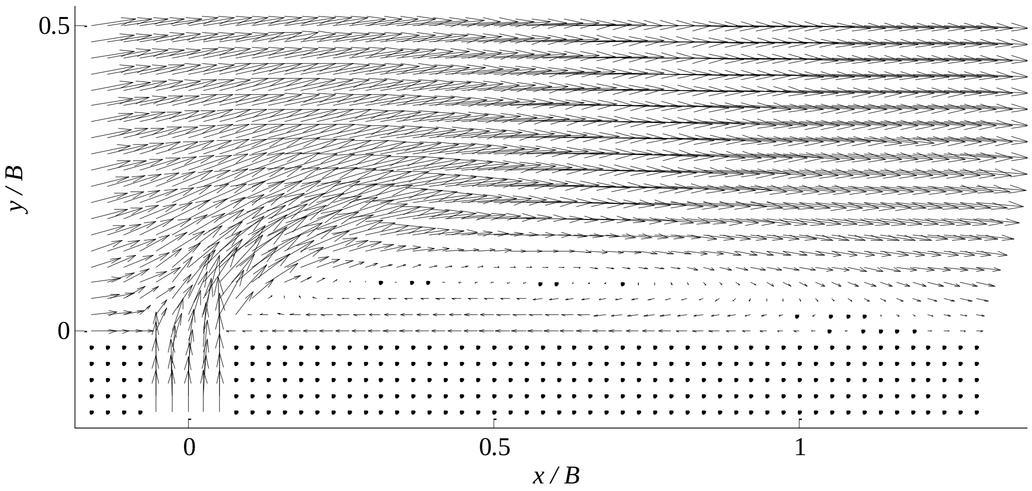

Figure 7.2 Predicted velocity vectors for M_1=0.105 by LABSWE$^{\mathrm{MRT}}$.

Figures 7.3-7.5 show that the calculated length (L) and height (H) of the recirculation zone. Both the height and length of recirculation increase with the momentum flux ratio M_1. However, the ratio of height to length (*H/L*) is almost independent of the momentum flux ratio M_1. Although predictions by LABSWE and LABSWE$^{\mathrm{MRT}}$ overestimate the width of eddy slightly, the predicted recirculation length agrees well with the experiments. Recognising some uncertainties in the experiments, such agreement seems satisfactory. The results from the conventional numerical method with $k-\varepsilon$ closure by McGuirk and Rodi [114] are plotted in the figures, showing that the BGK-LBM and MRT-LBM offer some improvement.

The performances of LABSWE and LABSWE$^{\mathrm{MRT}}$ have been compared for this case. The relative error $\Delta E = \frac{R_{com}-R_{exp}}{R_{exp}}$, in which, R_{com} is the result from the computations and R_{exp} by experiments, is used to evaluate the errors between the LABSWE and LABSWE$^{\mathrm{MRT}}$. The average relative errors of L/B, H/B, and L/H for MRT-LBM are 0.14, 0.13 and 0.15 respectively. As for LABSWE, these values are 0.17, 0.12 and 0.21 from the Figures 7.3-7.5. Overall, LABSWE$^{\mathrm{MRT}}$ model seems marginally more accurate than LABSWE model.

Furthermore, as M_1 increases, the difference becomes more pronounced. For example: stable simulated results are obtained by LABSWE$^{\mathrm{MRT}}$ with s_7=s_8=1/τ and τ=0.502 for M_1=10.526. Based on it, the calculated length of recirculation *L/B* is 6.952 which agrees well with experimental length 7.096. However, the computation becomes unstable with τ=0.502 for LABSWE, and a stable result can only be obtained with larger τ =0.503, which gives L/B=5.933 that is noticeably different from the experimental data. As a result, LABSWE^{MRT} is more stable and generates more accurate results for flows with higher Reynolds number than the LABSWE.

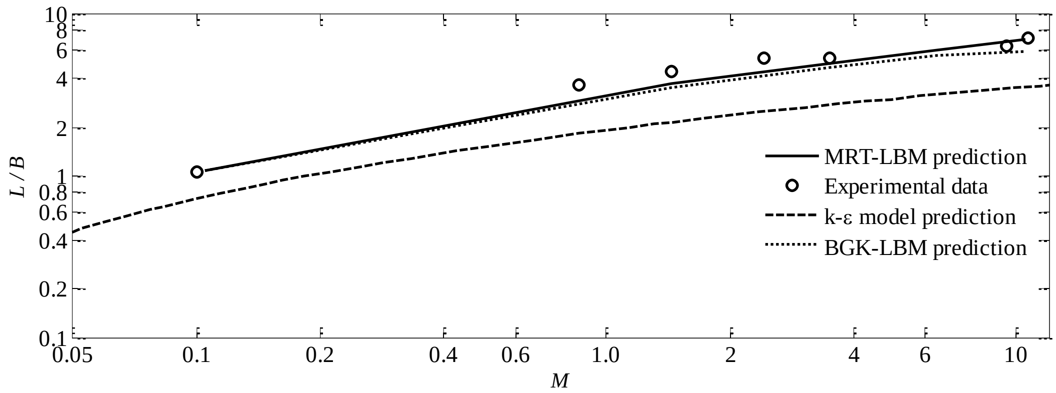

Figure 7.3 Recirculation eddy length.

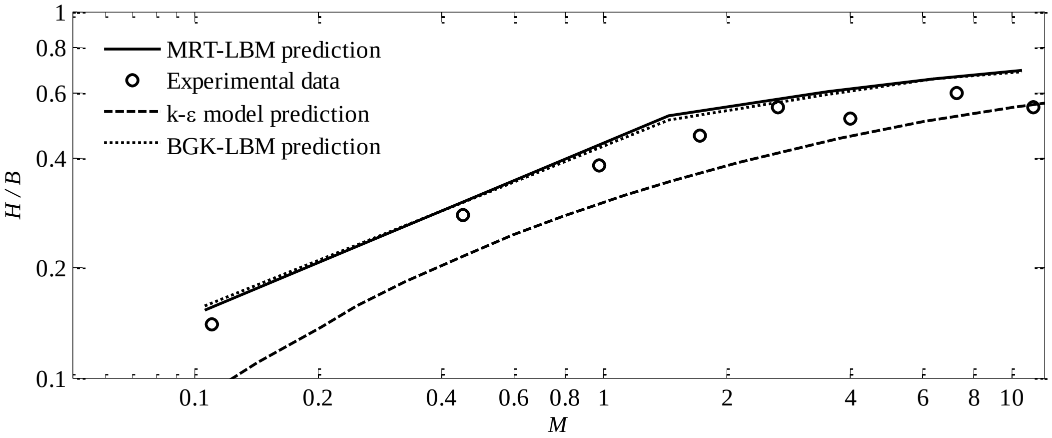

Figure 7.4 Recirculation eddy height.

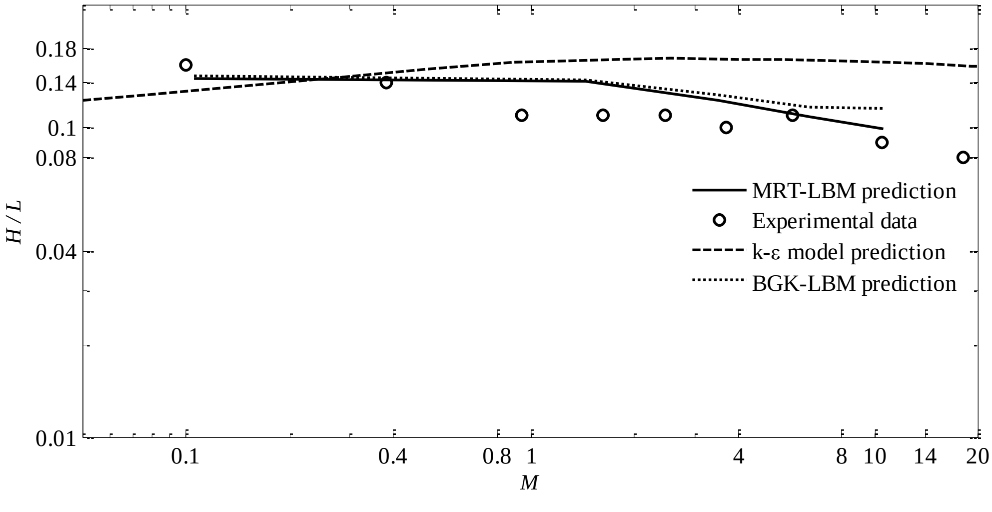

Figure 7.5 Recirculation shape factor.

Figure 7.6 shows the comparisons between predicted centerline trajectories of a warm jet from Carter's experimental data [114]. The jet trajectory is the locus of maximum temperature at different cross-sections. It is clear that MRT-LBM produce a better prediction than the $k-\varepsilon$ model by McGuirk and Rodi [114]. Although the figure shows that there are some differences between the experiments and the LABSWE$^{\mathrm{MRT}}$ prediction, this may be caused by buoyancy in the experiment which leads to stratification. Consequently the measured temperature is not truly depth-averaged temperature and the agreement is considered reasonable.

Figure 7.7 indicates the distribution of dimensionless excess temperature along the jet trajectory. DT is the maximum excess temperature over river temperature, and DT_0 is discharge excess temperature over the initial ambient river temperature. Both LABSWE$^{\mathrm{MRT}}$ and $k-\varepsilon$ models show similar levels of prediction accuracy and the simulated results agree well with the experimental data.

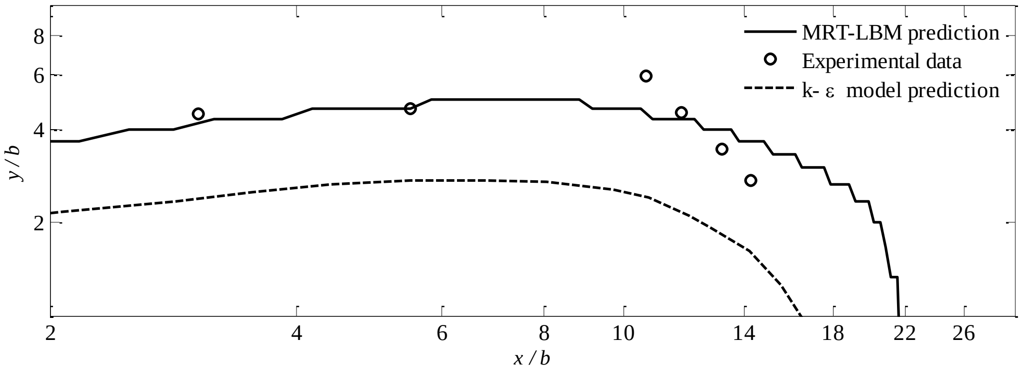

Figure 7.6 Jet centerline trajectory.

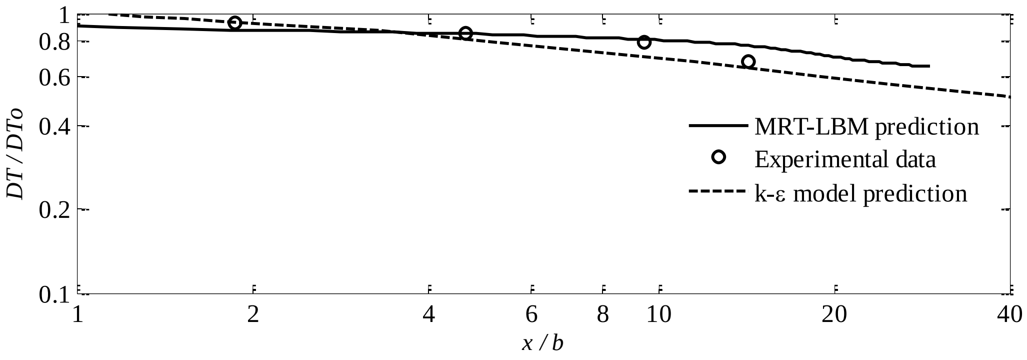

Figure 7.7 Temperature dilution along the jet centreline.

Case 2: Flow in a Harbour

The flow pattern in a simple idealised harbour is simulated and compared with the experiments by Yin et al. [182]. Figure 7.8 displays the layout of the channel including the harbour. The channel is 2.3m long and 3.8m wide. The water depth at outlet is 0.1725m, flow rate is 0.06593 m^3/s, time step Δt is 0.01s, grid space $\Delta x = \Delta y$ = 0.02m, s_7=s_8=1.960784, C_b=0.001. The relaxation parameters (from s_0 to s_6) in LABSWE^{MRT} and the relaxation time τ_1 in equation (3.169) are set to 1.

The computational grids for concentration are the same as that for velocity fields. The other parameters is Δt=0.01s, λ_x=λ_y=0.026, D_x=D_y=0.00052 m^2/s. According to the experiments, an initial uniform solute concentration of C_0=1 was created inside the harbour, and the concentration is zero outside it.

Streamlines and velocity vectors in the harbour are plotted in Figures 7.9 and 7.10, in which a near central clockwise vortex formed immediately. Consequently, outside the harbour, the velocity in the flow direction increases. This is consistent with the experimental results. Moreover, the time history of the relative average concentration in the harbour is shown in Figure 7.11 and the relative average concentration against time at the centre of the harbour is displayed in Figure 7.12. The two figures illustrate that similar predictions can be obtained by LBM and $k-\varepsilon$ models [182]. From Figure 7.12, the average relative errors of concentration for LABSWE^{MRT} and LABSWE are 0.18 and 0.31; for Figure 7.11, the corresponding errors are 0.17 and 0.36. Thus, the LABSWE^{MRT} again produces more accuracy results than the BGK-LBM. All models show some discrepancy during the initial period, because the water flow is unstable at the beginning of the experiments [182]. In view of this and the inevitable experimental errors, the agreements between predictions and experiments appear satisfactory. It should be noted that the concentration is only calculated directly by the BGK-LBM model (Eq.3.169) in this thesis and MRT-LBM prediction in Figures 7.11 and 7.12 means that concentration is calculated based on velocity fields by LABSWE^{MRT}.

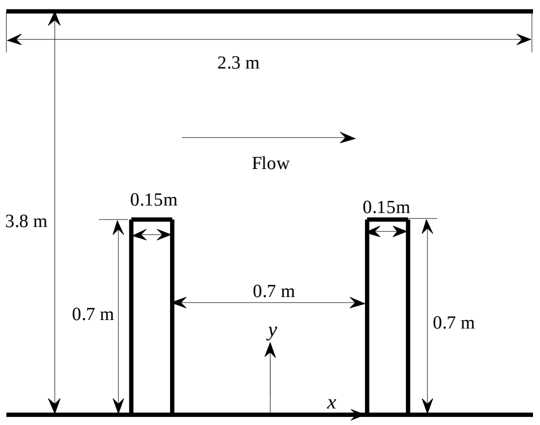

Figure 7.8 Plan view of harbour layout.

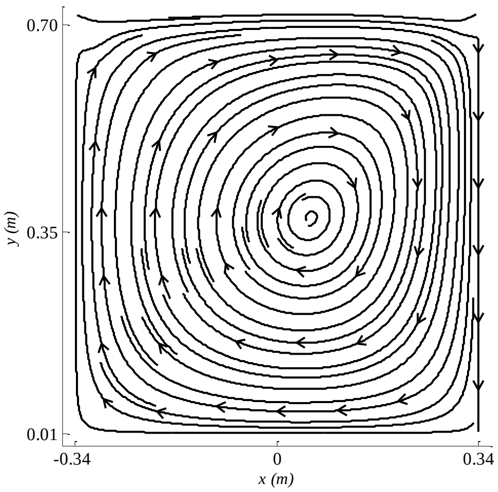

Figure 7.9 Streamlines in harbour by MRT-LBM.

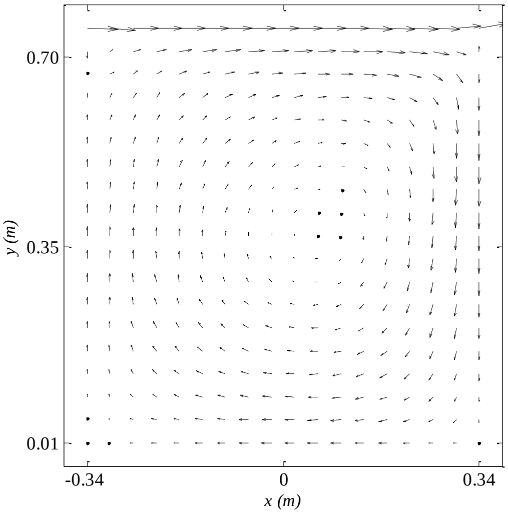

Figure 7.10 Velocity vectors in harbour by MRT-LBM.

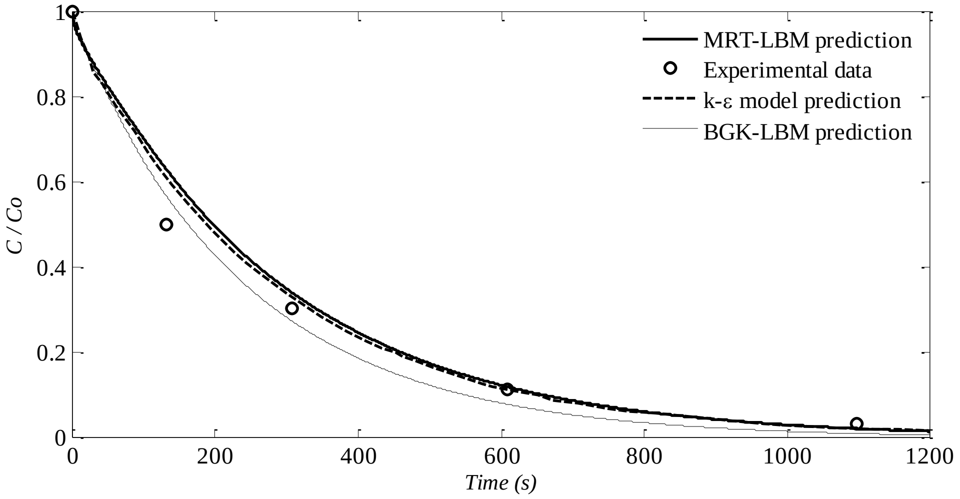

Figure 7.11 Dimensionless average concentration C/C_0 against time in harbour.

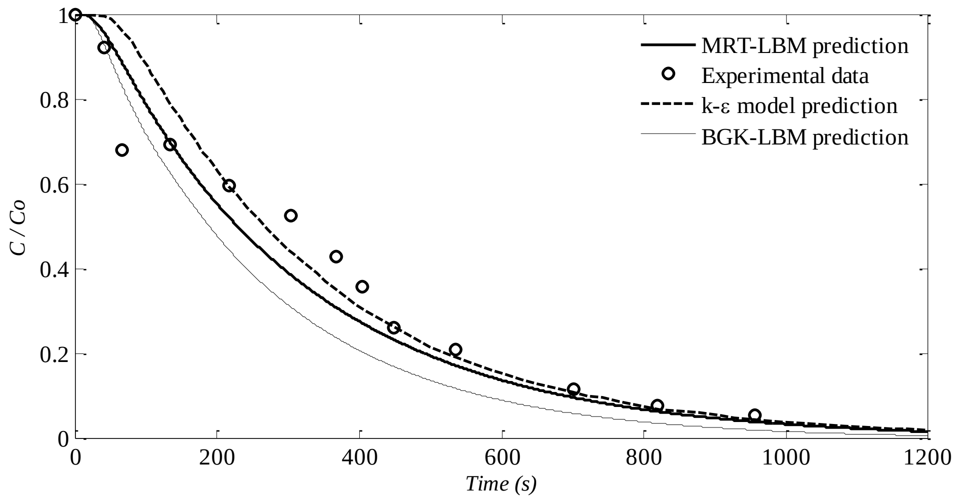

Figure 7.12 Dimensionless average concentration C/C_0 against time at x=0, y=0.35m (Centre point of harbour).

Case 3: Shallow Recirculation Flow

Shallow recirculation flows are common occurrences in nature. Babarutsi [149] studied the influence of bed-friction on the recirculation zone and dye-concentration distribution in a shallow open channel by experiments. Nassiri simulated the dye-concentration distribution by the Lagrangian second-moment method (SMM) [183]. A two-length-scale $k-\varepsilon$ turbulence model and two-dimensional Large Eddy Simulation was used to compute the dye-concentration distribution by Masoud [184].

Figure 7.13 shows the flow pattern and predicted streamlines by LABSWE^{MRT} in the shallow recirculation flow investigated here. A large recirculation is formed after the expansion in the channel. In the computation, a 360×60 lattice is used, inlet width d=0.3m, flow rate Q_0=0.0009918m^3/s, Δt=0.005s, Δx=Δy=0.01m, water depth at outlet h_0=0.0135m; relaxation parameters s_7=s_8=1.923077. For wall boundary, a semi-slip condition is adopted [3]. Different friction coefficients are used for wall and bed. In this case, the bed friction coefficient C_b is 0.012015 and wall friction coefficient is 0.180225. The relaxation parameters from s_0 to s_6 and the relaxation time τ_1 are equal to 1. For the calculation of concentration, time step Δt=0.005s, Δx=Δy=0.01m, λ_x=λ_y=0.01, D_x=D_y=0.0001m^2/s.

The predicted reattachment length is 0.8284m and agrees well with the experimental length of 0.82m [185]. The location of the tracer injection is important in establishing the solute concentration distribution. In the simulation, the tracer is injected into the corner of the step (see Figure 7.13) with $C_0=0.93$ to match that in the experiments. At steady state, the dye covered the entire recirculation area and formed a wake downstream as shown in Figure 7.14, and the normalized concentration distribution C/C_0 at cross-sections in the spanwise direction at $x = 0.5L$, L, $1.5L$ and $2L$ is displayed in Figure 7.15. It is apparent that better prediction is obtained by MRT-LBM than with the Lagrangian second-moment method (SMM). Except for the cross section at $x = L$ ($\Delta E = 0.38$ for LABSWE$^{\text{MRT}}$ and 0.25 for LABSWE), the average relative errors of concentration for LABSWE$^{\text{MRT}}$ are smaller than those for LABSWE indicating that the LABSWE$^{\text{MRT}}$ has a better prediction than LABSWE. Although there are some departures between experiment and LABSWE$^{\text{MRT}}$ predictions, especially for third and fourth cross-sections, however, the agreement appears acceptable if the errors in the experiments are taken into account.

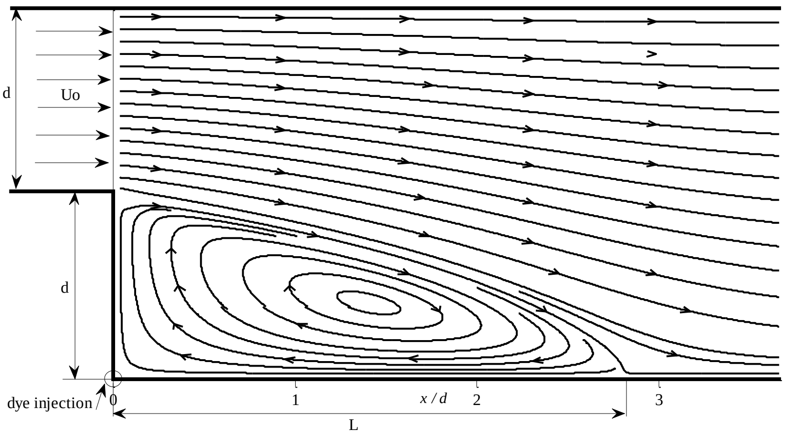

Figure 7.13 Plot of flow pattern and predicted streamlines for shallow recirculating flow (plan view).

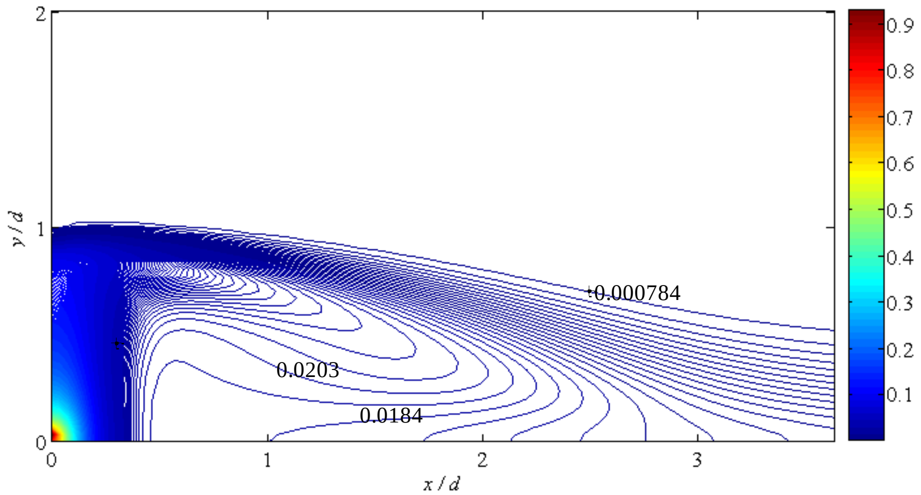

Figure 7.14 Concentration contours.

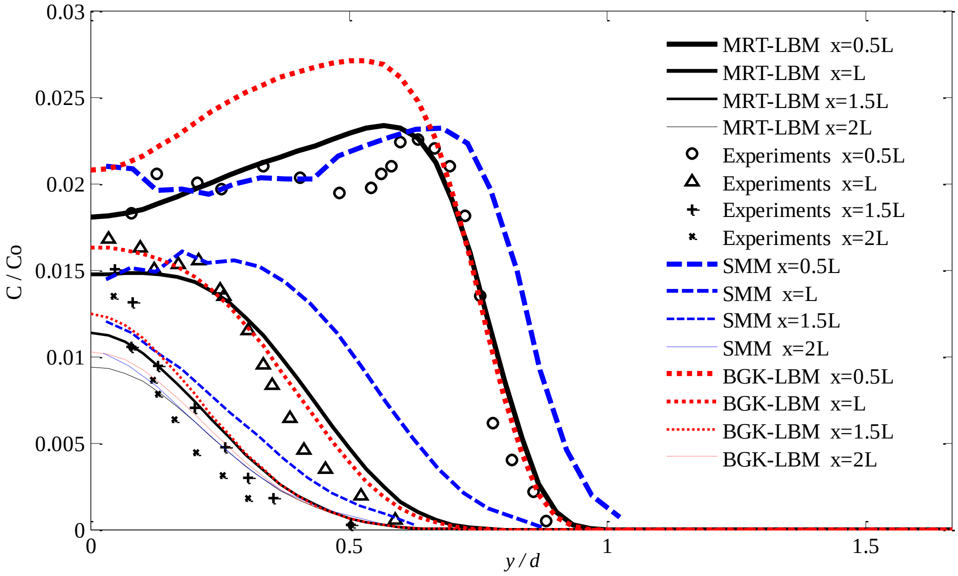

Figure 7.15 Comparisons of normalized concentration profiles
at different cross sections ($x = 0.5L, L, 1.5L, 2L$).

7.5 Conclusions

Both of LABSWE and LABSWE^{MRT} have been used to solve shallow water equations. The advection-diffusion equation is further solved by lattice Boltzmann equation. Three typical solute transport cases in shallow water are investigated to verify the models. The following conclusions are made as follows:

(a) For side discharge flow, in accordance with the experiments, both the height and length of the recirculation zone increase with the momentum flux ratio M_1. However, the ratio of recirculation height to length shows little dependence on the momentum flux ratio M_1. In addition to good agreement between simulated velocity fields and those in experiments, the prediction of temperature dilution along the jet centreline and the jet centerline trajectory are acceptable.

(b) In an idealised harbour, a clockwise vortex formed and the vortex centre is located close to the habour centre. Outside the harbour, the water flow velocity increases as a result. This is consistent with the experimental results. Again, the agreement between prediction and experiments for concentrations distributions in the harbour appears satisfactory.

(c) The location of dye injection plays an important role in simulation of concentration distribution for shallow recirculation flows. The farther the location of dye injection is away from the inlet, the greater the concentration is. This is correctly predicted by the model.

(d) Compared to LABSWE, the LABSWE$^{\mathrm{MRT}}$ formulation is found to have better stability and is capable of simulating flows with higher Reynolds number. Although it costs more computational time, it is beneficial to some flow problems.

(e) For the first case study, both LABSWE$^{\mathrm{MRT}}$ and LABSWE generate better predictions than the $k - \varepsilon$ model; for the third case, better simulated results can be obtained by MRT-LBM than the Lagrangian second-moment method (SMM).

Chapter 8: Coupling LABSWE^{MRT} and Euler-WENO Scheme for Morphological Evolution

8.1 Introduction

Morphological evolution in shallow water flows is investigated in this chapter. The shallow water equations are solved by LABSWE^{MRT} with the improved scheme for the force term. The fifth order Euler-WENO scheme is coupled with the lattice Boltzmann method to solve the morphological equation for the bed evolution caused by bed-load sediment transport. Three typical test cases have been simulated by the coupled model and the numerical results have been compared with either the corresponding experimental data or the analytical solutions.

8.2 Background

Sediment transport plays a key role in the morphological evolution occurring in coastal areas, rivers, and estuaries, where the water flow is dominated by horizontal characteristics and can be described by the shallow water equations [12-15]. Studies on morphological changes have attracted increasing interest in the fields of water resource exploitation and environment protection [16]. In the literature, several numerical methods like the finite volume and finite difference methods have been adopted to simulate the morphological evolution due to sediment transport [17, 18]. There are relatively fewer studies on using the lattice Boltzmann method. The morphological evolution relates to change to the bed due to sediment transport, and it can be accounted for by direct inclusion of the empirical estimation of the bed load transport in the equation. In this chapter, we will use the lattice Boltzmann model with the MRT for solving the shallow water equations. As bed load sediment transport is proportional to the velocity cubed and the LBM is generally second order accurate, a higher order accuracy scheme for the morphological evolution becomes necessary and hence the fifth order Euler-WENO finite difference scheme has been adopted to reduce the errors. Such a mixed model can offer the superior advantages of the LBM for the flow solver to the conventional numerical methods and remains the similar feature for solution of the morphological equation conventionally. The model has been validated by simulating three typical shallow water flows involving bed load transport, in which the results are compared with the experimental data or analytical solutions.

8.3 Governing Equations

The flows fields are solved by the LABSWE$^{\mathrm{MRT}}$ and the equation for morphological evolution can be expressed as:

$$(1-po)\frac{\partial z_b}{\partial t}=\frac{\partial q_{bj}}{\partial x_j} \tag{8.1}$$

where the subscripts *i* and *j* are the space direction indices and the Einstein summation convention is used; t is time, x_i stands for either *x* or *y* in directions *i* or *j*; po is the bed porosity and z_b is bed elevation; and q_{bj} is bed-load transport rate in *j* directions, which will be determined using an empirical or semi-empirical expression according to a specific scenario.

8.4 Solution of the Morphological Evolution Equation

There are different methods to solve the morphological evolution equation such as Lax-Wendroff schemes [186], non-oscillating centred scheme (NOCS) [187] and Euler-WENO scheme [188]. Long et al. [188] compared the classical lower order Lax–Wendroff, modified Lax–Wendroff schemes and Euler-WENO scheme. They concluded that the fifth order Euler-WENO scheme has obvious advantages over the other schemes with artificial viscosity and filtering process. In general, the lattice Boltzmann method is second-order accurate and the morphological evolution is very sensitive to flow velocity and proportional to the velocity cubed. Consequently, the fifth order Euler-WENO scheme is preferred to be used for solution of the morphological equation for bed evolution by bed load transport.

The WENO is evolved from on the Essentially Non-Oscillatory (ENO) scheme whose key idea is to use the smoothed stencil among several candidates to approximate the fluxes at the cell interfaces ($i\pm1/2$, j) and (i, $j\pm1/2$), respectively, to high order accuracy without spurious oscillations in the physical variable near shocks at the same time. The WENO is further improved by taking a weighted average of the candidate stencils. The weights are adjusted to obtain local smooth change in flow parameters. The sediment transport rates $q_{bx}$and q_{by} can be split into two parts associated with bedform propagation in the positive and negative directions, namely, q_{bx}^{+}, q_{bx}^{-}, q_{by}^{+}, and q_{by}^{-} and hence $q_{bx} = q_{bx}^{+} + q_{bx}^{-}$ and $q_{by} = \mathrm{q}_{\mathrm{by}}^{+} + \mathrm{q}_{\mathrm{by}}^{-}$. More details can be found in Long et al. [188], Jiang and Shu [189], and Jiang et al. [190]. The terms, $\frac{\partial q_b}{\partial x}$ and $\frac{\partial q_b}{\partial y}$, can be calculated as

$$\frac{\partial q_b(i,j)}{\partial x} = \frac{\hat{q}_{bx}(i+\frac{1}{2},j) - \hat{q}_{bx}(i-\frac{1}{2},j)}{\Delta x} \tag{8.2}$$

$$\frac{\partial q_b(i,j)}{\partial y} = \frac{\hat{q}_{by}(i,\ j+\frac{1}{2}) - \hat{q}_{by}(i,\ j-\frac{1}{2})}{\Delta y} \tag{8.3}$$

where

$$\hat{q}_{bx}\left(i+\frac{1}{2},j\right) = \hat{q}_{bx}^{-}\left(i+\frac{1}{2},j\right) + \hat{q}_{bx}^{+}\left(i+\frac{1}{2},j\right) \tag{8.4}$$

$$\hat{q}_{by}\left(i,j+\frac{1}{2}\right) = \hat{q}_{by}^{-}\left(i,j+\frac{1}{2}\right) + \hat{q}_{by}^{+}\left(i,j+\frac{1}{2}\right) \tag{8.5}$$

The left-biased-fluxes $\hat{q}_{bx}^{-}\left(i+\frac{1}{2},j\right)$ and right-biased-fluxes $\hat{q}_{bx}^{+}\left(i+\frac{1}{2},j\right)$ are calculated, respectively, by the following equations:

$$\hat{q}_{bx}^{-}\left(i+\frac{1}{2},j\right) = \begin{cases} \omega_{x1}q_{bx}^{(1)}\left(i+\frac{1}{2},j\right) + \omega_{x2}q_{bx}^{(2)}\left(i+\frac{1}{2},j\right) + \omega_{x3}q_{bx}^{(3)}\left(i+\frac{1}{2},j\right), & if\ C_x(i+\frac{1}{2},j) \geq 0 \\ 0, & if\ C_x(i+\frac{1}{2},j) < 0 \end{cases} \tag{8.6}$$

$$\hat{q}_{bx}^{+}\left(i+\frac{1}{2},j\right) = \begin{cases} \tilde{\omega}_{x1}\tilde{q}_{bx}^{(1)}\left(i+\frac{1}{2},j\right) + \tilde{\omega}_{x2}\tilde{q}_{bx}^{(2)}\left(i+\frac{1}{2},j\right) + \tilde{\omega}_{x3}\tilde{q}_{bx}^{(3)}\left(i+\frac{1}{2},j\right), & if\ C_x(i+\frac{1}{2},j) < 0 \\ 0, & if\ C_x(i+\frac{1}{2},j) \geq 0 \end{cases} \tag{8.7}$$

in which, $C_x\left(i+\frac{1}{2},j\right) = \frac{-\frac{\partial q_{bx}}{\partial x}}{(1-po)\frac{\partial z_b}{\partial x}}$ is the bed-form propagation phase speeds in the *x* direction and can be estimated numerically. $q_{bx}^{(1)}\left(i+\frac{1}{2},j\right)$, $q_{bx}^{(2)}\left(i+\frac{1}{2},j\right)$ and $q_{bx}^{(3)}\left(i+\frac{1}{2},j\right)$ are candidate stencils for estimating $\hat{q}_{bx}^{-}\left(i+\frac{1}{2},j\right)$ with a third order accuracy and $\tilde{q}_{bx}^{(1)}\left(i+\frac{1}{2},j\right)$, $\tilde{q}_{bx}^{(2)}\left(i+\frac{1}{2},j\right)$ and $\widetilde{q}_{bx}^{(3)}\left(i+\frac{1}{2},j\right)$ are used to calculate $\hat{q}_{bx}^{+}\left(i+\frac{1}{2},j\right)$. These six candidate stencils can be calculated by

$$q_{bx}^{(1)}\left(i+\frac{1}{2},j\right)=\frac{1}{3}q_{bx}(i-2,j)-\frac{7}{6}q_{bx}(i-1,j)+\frac{11}{6}q_{bx}(i,j) \tag{8.8}$$

$$q_{bx}^{(2)}\left(i+\frac{1}{2},j\right)=-\frac{1}{6}q_{bx}(i-1,j)-\frac{5}{6}q_{bx}(i,j)+\frac{1}{3}q_{bx}(i+1,j) \tag{8.9}$$

$$q_{bx}^{(3)}\left(i+\frac{1}{2},j\right)=\frac{1}{3}q_{bx}(i,j)+\frac{5}{6}q_{bx}(i+1,j)-\frac{1}{6}q_{bx}(i+2,j) \tag{8.10}$$

$$\tilde{q}_{bx}^{(1)}\left(i+\frac{1}{2},j\right)=-\frac{1}{6}q_{bx}(i-1,j)+\frac{5}{6}q_{bx}(i,j)+\frac{1}{3}q_{bx}(i+1,j) \tag{8.11}$$

$$\tilde{q}_{bx}^{(2)}\left(i+\frac{1}{2},j\right)=\frac{1}{3}q_{bx}(i,j)+\frac{5}{6}q_{bx}(i+1,j)-\frac{1}{6}q_{bx}(i+2,j) \tag{8.12}$$

$$\widetilde{q}_{bx}^{(3)}\left(i+\frac{1}{2},j\right)=\frac{11}{6}q_{bx}(i+1,j)-\frac{7}{6}q_{bx}(i+2,j)+\frac{1}{3}q_{bx}(i+3,j) \tag{8.13}$$

where, $\omega_{x1},\omega_{x2},\omega_{x3},\widetilde{\omega}_{x1},\widetilde{\omega}_{x2},\widetilde{\omega}_{x3}$ are the weights which need to be carefully chosen such that $\hat{q}_{bx}^{-}\left(i+\frac{1}{2},j\right)$ and $\hat{q}_{bx}^{+}\left(i+\frac{1}{2},j\right)$ given by equations (8.6) and (8.7) are the fifth order accurate approximations for $q_{bx}\left(i+\frac{1}{2},j\right)$. The weights are determined as follows:

$$\omega_{x1}=\frac{\alpha_{x1}}{\alpha_{x1}+\alpha_{x2}+\alpha_{x3}}\ \ (8.14)\qquad \omega_{x2}=\frac{\alpha_{x2}}{\alpha_{x1}+\alpha_{x2}+\alpha_{x3}}\ \ (8.15)\qquad \omega_{x3}=\frac{\alpha_{x3}}{\alpha_{x1}+\alpha_{x2}+\alpha_{x3}}\ (8.16)$$

$$\widetilde{\omega}_{x1}=\frac{\tilde{\alpha}_{x1}}{\tilde{\alpha}_{x1}+\tilde{\alpha}_{x2}+\tilde{\alpha}_{x3}}\ \ (8.17)\qquad \widetilde{\omega}_{x2}=\frac{\tilde{\alpha}_{x2}}{\tilde{\alpha}_{x1}+\tilde{\alpha}_{x2}+\tilde{\alpha}_{x3}}\ \ (8.18)\qquad \widetilde{\omega}_{x3}=\frac{\tilde{\alpha}_{x3}}{\tilde{\alpha}_{x1}+\tilde{\alpha}_{x2}+\tilde{\alpha}_{x3}}\ (8.19)$$

where

$$\alpha_{x1}=\frac{0.1}{(S_{x1}+\in)^2}\ \ (8.20)\qquad \alpha_{x2}=\frac{0.6}{(S_{x2}+\in)^2}\ \ (8.21)\qquad \alpha_{x3}=\frac{0.3}{(S_{x3}+\in)^2}\ \ (8.22)$$

$$\tilde{\alpha}_{x1}=\frac{0.3}{(\tilde{S}_{x1}+\in)^2}\ \ (8.23)\qquad \tilde{\alpha}_{x2}=\frac{0.6}{(\tilde{S}_{x2}+\in)^2}\ \ (8.24)\qquad \tilde{\alpha}_{x3}=\frac{0.1}{(\tilde{S}_{x3}+\in)^2}\ \ (8.25)$$

with $\in\approx 10^{-20}$ as a small number to avoid division by zero and the smoothness measurements S_{x1}, S_{x2},and S_{x3} are given by

$$S_{x1}=\frac{13}{12}(v_{x1}-2v_{x2}+v_{x3})^2+\frac{1}{4}(v_{x1}-4v_{x2}+3v_{x3})^2 \tag{8.26}$$

$$S_{x2}=\frac{13}{12}(v_{x2}-2v_{x3}+v_{x4})^2+\frac{1}{4}(v_{x2}-v_{x4})^2 \tag{8.27}$$

$$S_{x3}=\frac{13}{12}(v_{x3}-2v_{x4}+v_{x5})^2+\frac{1}{4}(3v_{x3}-4v_{x4}+v_{x5})^2 \tag{8.28}$$

$$\tilde{S}_{x1}=\frac{13}{12}(v_{x2}-2v_{x3}+v_{x4})^2+\frac{1}{4}(v_{x2}-4v_{x3}+3v_{x4})^2 \tag{8.29}$$

$$\tilde{S}_{x2}=\frac{13}{12}(v_{x3}-2v_{x4}+v_{5})^2+\frac{1}{4}(v_{x3}-v_{x5})^2 \tag{8.30}$$

$$\tilde{S}_{x3}=\frac{13}{12}(v_{x4}-2v_{x5}+v_{x6})^2+\frac{1}{4}(3v_{x4}-4v_{x5}+v_{x6})^2 \tag{8.31}$$

in which

$v_{x1} = q_{bx}(i-2,j)$(8.32) $v_{x2} = q_{bx}(i-1,j)$(8.33) $v_{x3} = q_{bx}(i,j)$ (8.34)

$v_{x4} = q_{bx}(i+1,j)$(8.35) $v_{x5} = q_{bx}(i+2,j)$(8.36) $v_{x6} = q_{bx}(i+3,j)$ (8.37)

Similarly, $\hat{q}_{by}^{-}\left(i,j+\frac{1}{2}\right)$ and $\hat{q}_{by}^{+}\left(i,j+\frac{1}{2}\right)$ can be calculated.

The computation procedure is summarised as follows:

1. Solve the equations (3.131) (3.54), and (3.59) to obtain the steady velocity field *u* and *v*, and water depth *h*.
2. Calculate the sediment transport rates q_{bx} and q_{by} using the *u*, *v*, *h* from step 1.
3. Compute the new bed height z_b by solving the morphological evaluation equation (8.1).
4. Repeat steps 1-3 with the new z_b until a solution is obtained.

In the first step above, the relative error

$$\Delta E = \sqrt{\sum_{i=1}^{i=N} \frac{(u_i^t - u_i^{t-1})^2}{(u_i^{t-1})^2} / N} \tag{8.38}$$

is used to determine whether the flow reaches a steady state. For example, if the ΔE is smaller than ΔE_r, it can be said that the flow is steady, and vice versa, where ΔE_r is a predefined tolerance. It should be noted that the time step for both flow and bed-load computations are the same although different time steps can be used in the simulations [188, 191, 192].

8.5 Boundary Conditions

For steady flow computations, a constant discharge and a water depth are specified at inlet and outlet boundaries, respectively, and slip boundaries are used for side walls [3]. For determination of bed-load transport, zero gradients for the sediment transport rates at inlet and outlet are adopted, which means that there is no change for bed profile at inlet and outlet.

8.6 Numerical Results

Three typical test cases are presented in this section to demonstrate the accuracy and applicability of the mixed model with simulations of the bed evolution of (a) 1D Gaussian dune, (b) 1D trapezoidal dune, and (c) 2D sand dune.

Test 1: Change of 1D Gaussian Dune

In the first test, a Gaussian sand dune on a fixed channel bed is simulated, which was also used in [188, 191, 192] for validation of their numerical schemes. It is a one-dimensional test, in which the discharge is constant with a rigid lid. An analytical solution is available for comparison. The parameters used in the test are $q_b = 0.001u^3$, $u = 10/h$, $h = -z_b$, $po = 0.4$. The initial shape of the Gaussian sand dune is defined by

$$z_b(x,0) = -6 + 2e^{[-0.01(x-150)^2]}, 0 \leq x \leq 300 \qquad (8.39)$$

In the computation, $\Delta x = 1m$, $\Delta t = 0.1s$, s_7=s_8=1 and s_0-s_6=1 are used. After the solution is obtained, the bed profiles at *t* = 600s, 2000s and 6000s are compared with the analytical solutions in Figure 8.1, revealing good agreements.

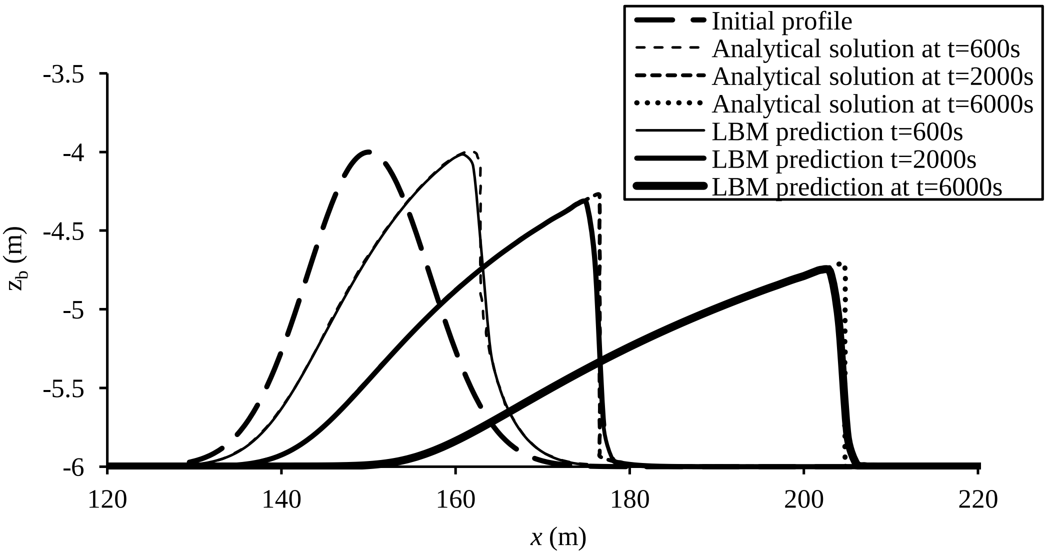

Figure 8.1 Comparisons of profiles of the dune evolution between analytical solutions and predictions.

Test 2: Bed Change of a 1D Trapezoidal Dune

As the experiment for morphological evolution of a 1D trapezoid of dune was conducted in a rectangular flume in Hydraulic Engineering Laboratory at the National University of Singapore [193], it is a suitable test to verify the coupled model. The sketch of the experiment is shown in Figure 8.2.

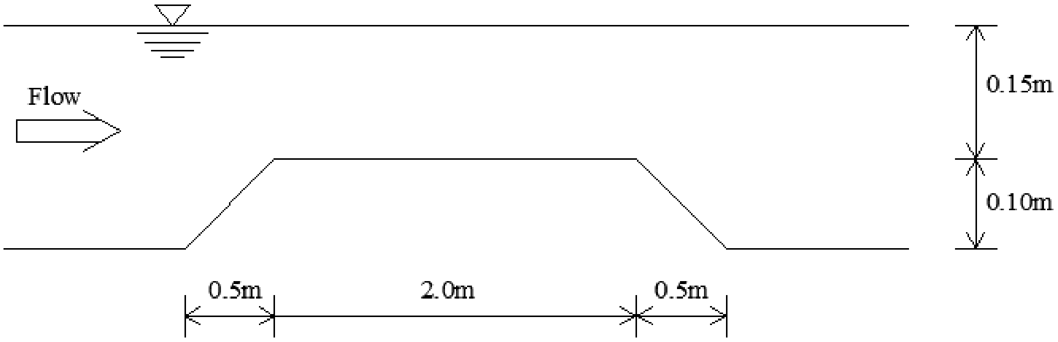

Figure 8.2 Layout of the experiments and the sand dune (Side view) on channel floor.

The flume is 15m long, 0.6m wide and 0.6m deep. In the experiment, the mean flow velocity and the water depth were kept constant as 0.32 m/s and 0.25 m, respectively. According to the experiments, the dune evolved downstream in the form of the bed-load transported with the flow. The whole process of the experiment lasted two hours and the flow was slowed down with the bed evolution. The velocity and the bed elevation were measured every half an hour.

The section in the numerical simulation is 6m long with 1m upstream and 2m downstream of the dune, respectively. The initial configuration of the dune is shown in Figure 8.2. The unit-width flow rate of 0.08 m^2/s and the water depth of 0.25m are specified at the upstream and downstream boundaries, respectively. The Manning's coefficient is 0.0145 [193]. The space step is $\Delta x=\Delta y=0.1$m; both the time steps for the flow and bed evolution are same and equal to 0.001s; $s_7=s_8=1.6667$; the relaxation parameters from s_0 to s_6 are equal to 1. For the sediment transport, the bed load transport rate q_b is calculated from the Meyer-Peter and Müller formula [194],

$$q_b = 8(\theta - \theta_{cr})^{\frac{3}{2}}\sqrt{(s-1)g}d_{50}^{1.5} \tag{8.40}$$

in which, θ is the Shields parameter and calculated with $\theta = \frac{\tau_b}{(\rho_s-\rho)gd_{50}}$ and θ_{cr} is critical Shields parameter that is calculated from the Shields curve according to Yalin [195]; d_{50} is the median diameter of the sediment particles; $s = (\rho_s - \rho)/\rho$ is the specific gravity of the particle; ρ_s is the sediment density; τ_b is bed shear stress; ρ is the density of water.

The profiles of the bed evolution from the simulated results at times t = 0.5, 1, 1.5 and 2.0 hours are shown in Figure 8.3.

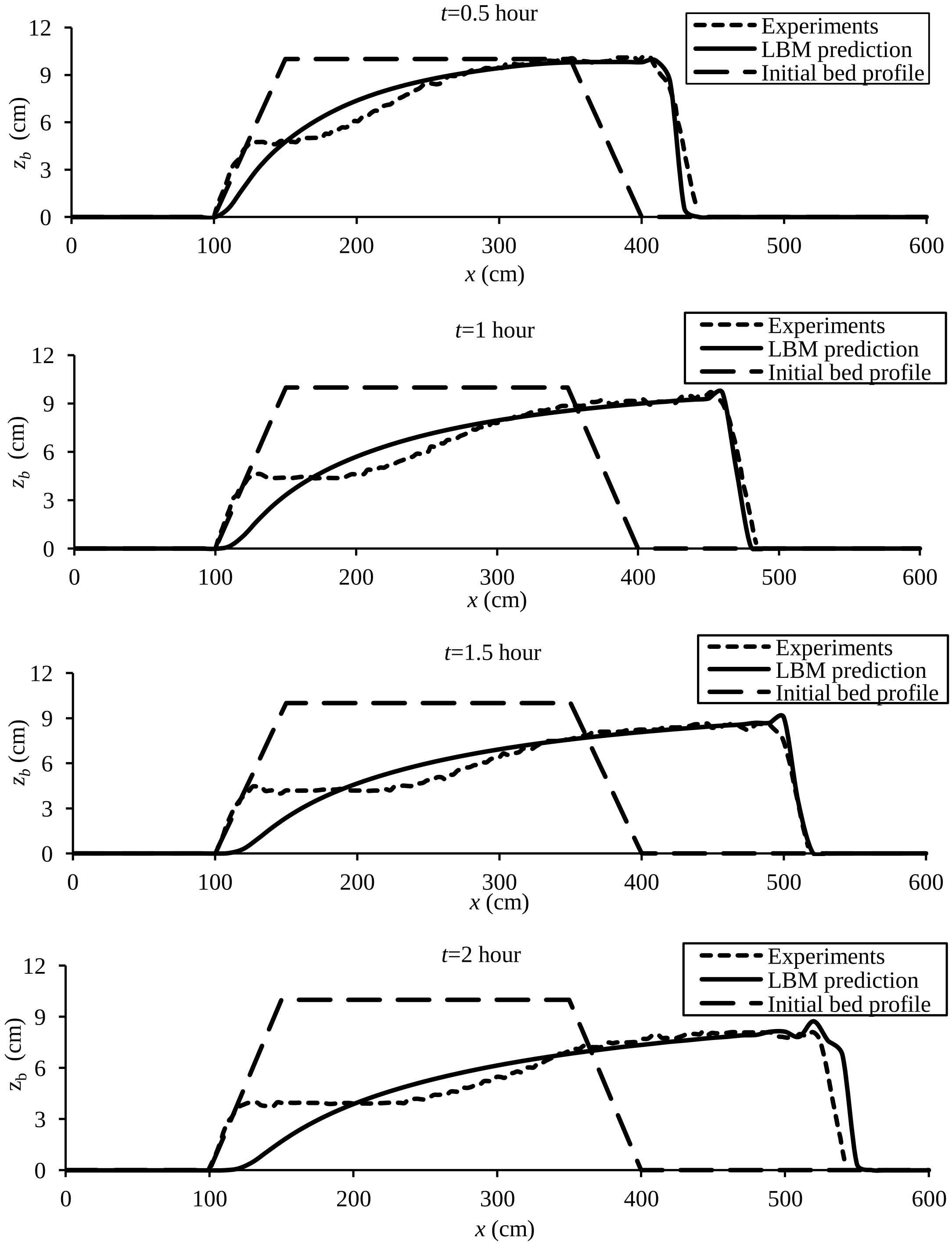

Figure 8.3 Comparisons of profiles of the dune evolution between experiments and predictions (*t*=0.5, 1.0, 1.5, 2.0 hours from top to bottom).

From Figure 8.3, it is clear that at the upstream of the dune, as the water depth reduced and velocity increased along the channel, the bed is eroded and bed-load sands move downstream. On the other hand, at the downstream of the dune, as the water recovered and velocity reduced, the bed-load sands began to deposit. Such process moved the sand dune downstream slowly with the flow and makes the dune become flatter and flatter. These findings have been confirmed by the experimental investigations. Some difference between the results obtained by LBM model and experiments can be found in the Figure 8.3, especially for the upstream of the dune. This may be due to the ignorance of the effect of slope in Equation (8.40) and this has been confirmed by Lin [193] using the finite difference method. Overall, the results by LBM model can be accepted with the consideration of errors existing in experiments.

Test 3: Morphological Evolution of 2D Sand Dune

In order to verify the proposed model further, a 2D sand dune is considered. This case has been tested numerically in [16, 191, 192, 196]. The channel is 1000m long and 1000m wide with the initial bed topography given by

$$z_b(x,y,0) = \begin{cases} \sin^2\left(\frac{(x-300)\pi}{200}\right)\sin^2\left(\frac{(y-400)\pi}{200}\right), & if\ 300 \le x \le 500\ and\ 300 \le x \le 500 \\ 0, & \text{eslewhere} \end{cases} \tag{8.41}$$

$$h(x,y,0) = 10 - z_b(x,y,0) \tag{8.42}$$

$$u(x,y,0) = \frac{10}{h(x,y,0)} \tag{8.43}$$

The following equations are used for the bed-load sediment transport rates,

$$q_{bx} = Au(x,y,t)[u^2(x,y,t) + v^2(x,y,t)] \tag{8.44}$$

$$q_{by} = Av(x,y,t)[u^2(x,y,t) + v^2(x,y,t)] \tag{8.45}$$

in which A=0.001. For this case, $\Delta x = 10m$, $\Delta t = 0.5s$, s_7=s_8=1/0.51, po = 0.4 and s_0-s_6=1 are used. The steady flow has been obtained in the simulation with initial condition (8.41)-(8.43) for the fixed bed before the module for morphological change is activated with the critical relative error ΔE_r of 6×10^{-8}. Figure 8.4 shows the numerical results for the steady flow used as an initial flow condition for the calculation using the coupled method for simulation of the flow and the bed evolution: (a) is the initial bed topography, (b) and (c) are the velocity components u and v, respectively, and (d) is the water surface of the steady flow over the fixed bed. This steady flow provides good initial flow conditions to model the interaction between the flow and the morphological change.

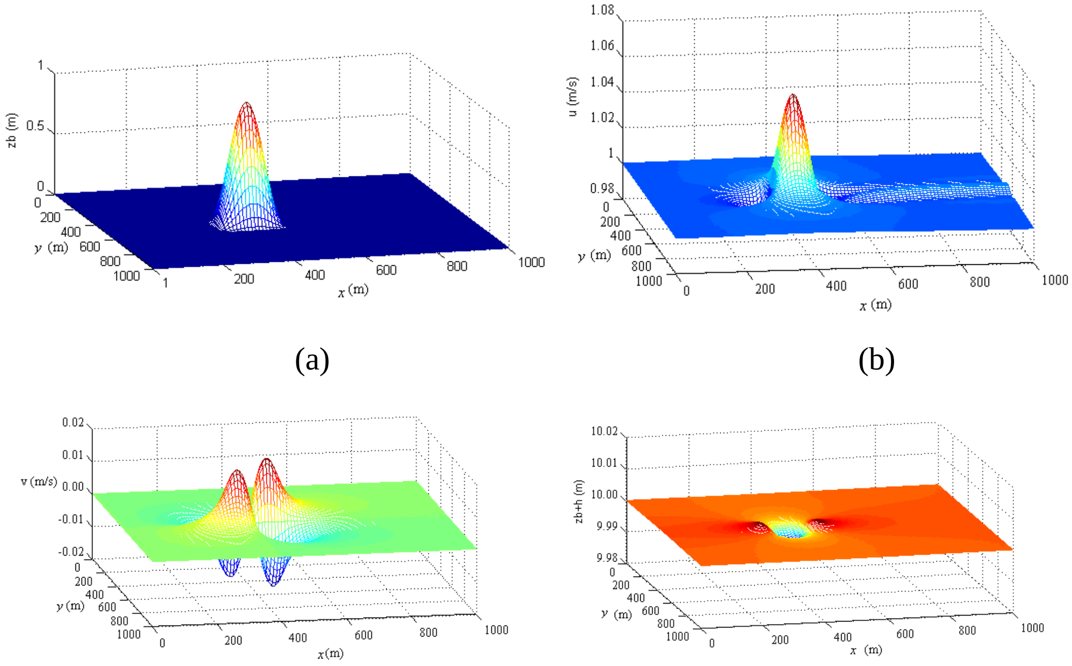

(a) (b)

(c) (d)

Figure 8.4 The initial bed configuration (a), steady velocity components *u* (b) and *v* (c), and water surface for flow over the fixed bed (d).

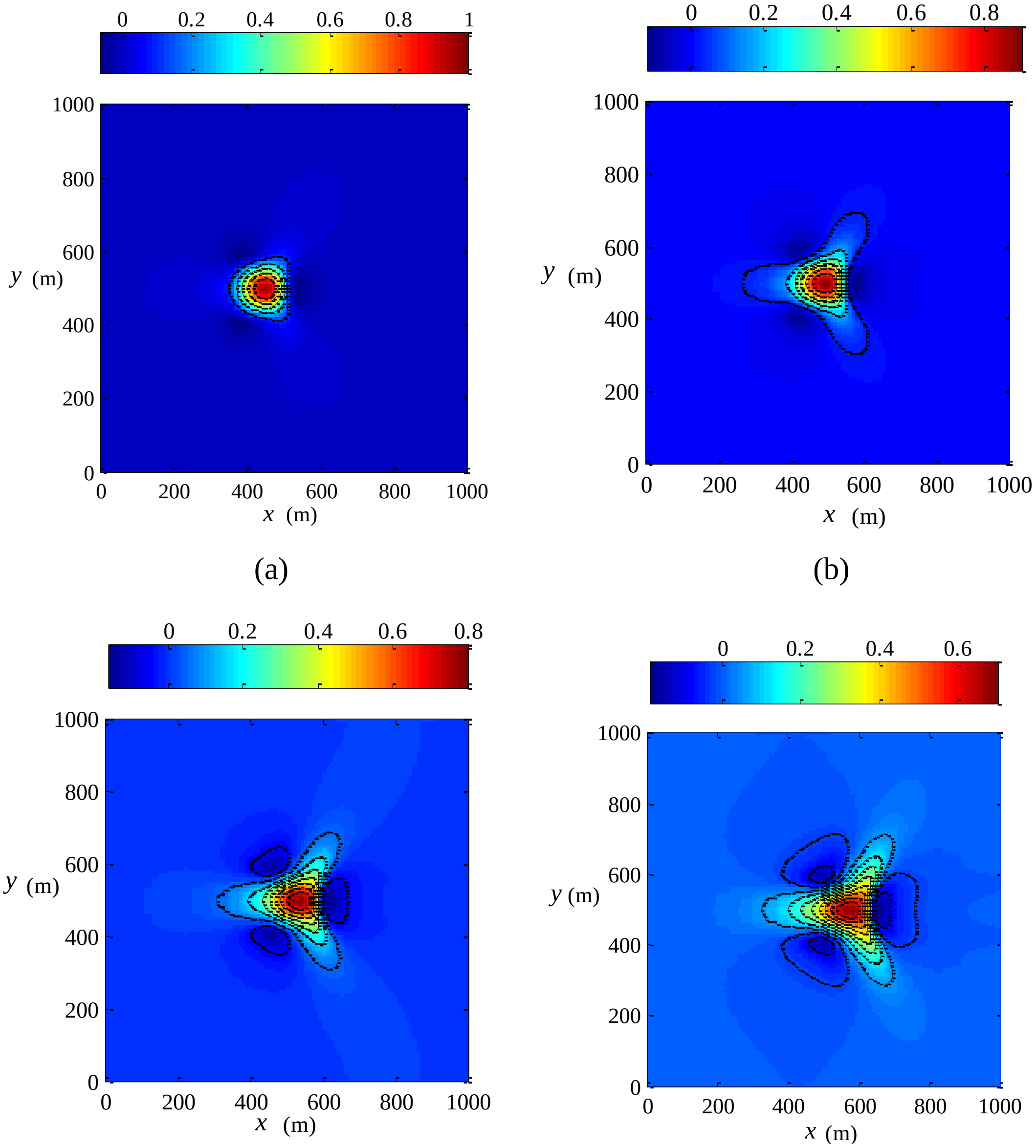

(a)

(b)

(c)

(d)

Figure 8.5 Snapshots of the bed evolution of 2D sand dune at t = 25 hours (a), 50 hours (b), 75 hours (c), and 100 hours (d). (The unit of bed elevation is meter.)

After the simulation is completed, the predicted contours for the bed configuration at different times t = 25hours, 50hours, 75hours, 100 hours are depicted in Figure 8.5. According to the equations (8.44) and (8.45), the bed-load transport rate is proportional to the velocity cubed and the velocity component u is much bigger than v in this case, hence leading to sediment transport largely in the x direction. From t = 0 to 100 hours, the apex of the sand dune has moved from x = 400m to about 570m. At the same time, the sand dune spread along y direction gradually and a star-shaped structure is well formed. Figure 8.5(a) to (d) clearly shows this process. These findings are consistent with those reported in [16, 191] and the morphological change agrees well with that by [16, 191] qualitatively. This suggests that the described mixed model is stable for calculation of bed evolution over long time and is able to provide similar accurate results with much simpler programming in more efficient way compared to conventional numerical methods.

8.7 Conclusions

Coupling the $\mathrm{LABSWE}^{\mathrm{MRT}}$ for flows with the fifth order Euler-WENO finite difference scheme for morphological equation has been developed to investigate the bed evolution in shallow water flows. The following conclusions can be drawn:

(a) The proposed mixed model is able to predict morphological evolution of 1D sand dune and hump, and 2D sand dune in shallow water flows. The predicted results agree well with the corresponding analytical solutions or experimental data.

(b) The Euler-WENO finite difference scheme is found to be stable and accurate for solution to the morphological evolution due to bed-load sediment transport.

(c) The coupled model has great potential to investigate the bed change caused by sediment transport in shallow water flows. To apply the proposed method to more practical flow problems, the advection-diffusion equation need to be incorporated into the present model to consider the suspended load transport.

Chapter 9: Conclusions and Recommendations

9.1 Preamble

As a relative new method for simulating the flows, the lattice Boltzmann has been applied widely and improved greatly over the past twenty years. Like other conventional CFD methods, LBM has its shortcomings and advantages. For example, LBM is only second-order accurate in space and time; and unstructured grid is difficult to incorporate into the standard LBM. However, the LBM becomes more and more popular for simulating flows because its algorithm is simple and efficient, and easy for parallel computation. Furthermore, it is easy to implement different boundary condition for complex geometries.

In this thesis, three kinds of the lattice Boltzmann method for shallow water, namely LABSWE, LABSWE^{TM}, and LABSWE^{MRT} respectively, are derived and discussed in detail. They have been applied to simulating different complex flows such as free surface flows in rectangular open channels, shallow water flows over discontinuous beds, and then they have also been extended to simulating a moving body in shallow water flows, and finally the environmental flows including solute transport and sediment transport under shallow waters. The main findings and contributions of this thesis are summarised in this chapter and future work is recommended.

9.2 Conclusions

9.2.1 Multiple-Relaxation-Time Lattice Boltzmann Method with Improved Force

The lattice Boltzmann method with multiple-relaxation-time is derived and discussed in detail. The shallow water equations are recovered correctly from LABSWE^{MRT} by using the Chapman-Enskog expansion for the first time. Compared to the LABSWE, the LABSWE^{MRT} formulation has better stability and is capable of simulating flows with higher Reynolds number. Although it costs more computational time (about 15%), it is benefical for some flows.

9.2.2 Modelling the Flow over Discontinuous Beds Using LABSWE^{MRT}

The flow over discontinus beds has not been solved well by conventional methods. It has been studied by LABSWE^{MRT} in this thesis. Unlike other numerical methods, no additional treatment is needed in the described method for flows over a bed with a vertical step. In order to solve this problem, a new force term is proposed and it is demonstated that it is crucial to produce the correct results. In order to include the head loss caused by the step, the resistance stress is added in the force term. The study shows that the calculated results with resistance stress are more practical. It has been found that the LABSWE is able to capture the shock waves without any special treatment as indicated in [93] and now it shows another attractive feature.

9.2.3 Moving Boundary in Shallow Water Flows

A lattice Boltzmann method based on the LABSWE^{MRT} for moving boundary conditions is developed for shallow water flows and is verified by the corresponding experiments. The additional momentum for correct interaction between the fluid and solid has been added to the model and a refill method for new fluid nodes moving out from solid nodes has been proposed. Moreover, FH’s, MMP’s, and Guo’s schemes for curved boundary conditons at second-order accuracy have been compared in detail. The proposed model is applied to simulate the flows around static and moving cylinders in shallow waters.

9.2.4 Solute Transport in Shallow Water Flows

Both of the LABSWE and the LABSWE^{MRT} is used and couplied with the advection-diffusion equation to study the solute transport. The equation is also solved by the lattice Boltzmann equation. Three typical solute transport cases in shallow waters are investigated to verify the models. The predicted results by LABSWE and LABSWE^{MRT} agree well with other corresponding results.

9.2.5 Mixed Numerical Method for Bed Evolution

Coupled the LABSWE^{MRT} with the fifth order Euler-WENO finite difference scheme, a mixed model for the morphological equation, has been developed to investigate the bed evolution in shallow water flows. The proposed mixed model is able to predict morphological evolution of 1D sand dune and hump, and 2D sand dune in shallow water flows. The predicted results agree well with the corresponding analytical solutions or experimental data. The Euler-WENO finite difference scheme is found to be stable and accurate for solution to the morphological evolution equation caused by bed-load sediment transport over long time.

9.2.6 Numerical simulation for free surface flows in rectangular shallow basins

The LABSWE^{TM} is applied to model the free surface flows in rectangular shallow basins. The results obtained by the LABSWE^{TM} have been compared to those by the finite volume and algebraic turbulence models and laboratory experiments. The results show that the lattice Boltzmann model can predict asymmetrical shallow flows and capture the typical features efficiently at the same accuracy as the conventional methods. The study demonstrates that LABSWE^{TM} is accurate to simulate the free surface flows and can be extended for wider range of application.

9.3 Recommendations

9.3.1 Simulating the Moving Body with Variable Velocity

In chapter 7, a moving body at constant velocity has been simulated by the lattice Boltzmann method. However, the moving velocity of a cylinder may not be constant in practice, such as landslides, the uprooted trees and damaged houses in flooding. As a result, the presented method needs to be extended into this case for more practical engineering.

9.3.2 Incorporation of the Suspended Sediment Transport

In chapter 8, the sediment transport is studied by the LABSWE^{MRT}. However, only the bed-load component of sediment is included. In some cases, suspended sediment also plays an important role in the morphological evolution in rivers, and such movement can be simulated by the advection-diffusion equation, which has been used for predicting solute transport in chapter 7. This study is currently in progress and will be reported in the later publications.

9.3.3 Supercritical Flow Simulation

Up to now, none of the LABSWE, LABSWE^{TM} and LABSWE-MRT has the ability of simulating the supercritical flow because of the stability limitation. Thang et al. [197] studied the stability of a D1Q3 LBM for shallow water flows and pointed out the limits of the LBM are the Courant condition and Fr<1. Besides, they claimed that they have modified the D1Q3 model which is stable for subcritical and supercritical flows although their results on supercritical flows have not been published. As the development of LBM, we believe this problem will be solved in the near future to make the LBM more powerful and practical for more real life problems.

9.3.4 Parallel Computation for LBM

In order to simulate the real life flows like flooding, a large number of grids are needed. Therefore, parallel computing is desirable for numerical simulation. Fortunately, one of most attractive advantages is the inherent feature of the parallel computation in the LBM. It is recommended that parallel computation of above three models can be implemented in the future studies.

References

1. Meselhe, F. Sotiropoulos, and Jr, *Numerical Simulation of Transcritical Flow in Open Channels.* Journal of Hydraulic Engineering, 1997. **123**(9): p. 774-783.
2. Cao, Z., et al., *Computational Dam-Break Hydraulics over Erodible Sediment Bed.* Journal of Hydraulic Engineering, 2004. **130**(7): p. 689-703.
3. Zhou, J.G., *Lattice Boltzmann Methods for Shallow Water Flows.* 2004: Springer.
4. Teeter, A.M., et al., *Hydrodynamic and sediment transport modeling with emphasis on shallow-water, vegetated areas (lakes, reservoirs, estuaries and lagoons).* Hydrobiologia, 2001. **444**(1): p. 1-23.
5. Huang, W. and Spaulding, M., *3D Model of Estuarine Circulation and Water Quality Induced by Surface Discharges.* Journal of Hydraulic Engineering, 1995. **121**(4): p. 300-311.
6. Wang, Jia-song, and He, You-sheng, *High-resolution numerical model for shallow water flows and pollutant diffusions.* Applied Mathematics and Mechanics, 2002. **23**(7): p. 741-747.
7. Liu, Z.w., et al., *Sigma-coordinate numerical model for side-discharge into natural rivers.* Journal of Hydrodynamics, Ser. B, 2009. **21**(3): p. 333-340.
8. Benkhaldoun, F., I. Elmahi, and M. Seaı¨d, *Well-balanced finite volume schemes for pollutant transport by shallow water equations on unstructured meshes.* Journal of Computational Physics, 2007. **226**(1): p. 180-203.
9. Murillo, J., et al., *Coupling between shallow water and solute flow equations: analysis and management of source terms in 2D.* International Journal for Numerical Methods in Fluids, 2005. **49**(3): p. 267-299.
10. Simpson, G. and Castelltort, S., *Coupled model of surface water flow, sediment transport and morphological evolution.* Computers & Geosciences, 2006. **32**(10): p. 1600-1614.
11. Cai, L., et al., *Computations of transport of pollutant in shallow water.* Applied Mathematical Modelling, 2007. **31**(3): p. 490-498.
12. Guo, Q. and Jin, Y., *Modeling Sediment Transport Using Depth-Averaged and Moment Equations.* Journal of Hydraulic Engineering, 1999. **125**(12): p. 1262-1269.

13. Wu, W., *Depth-Averaged Two-Dimensional Numerical Modeling of Unsteady Flow and Nonuniform Sediment Transport in Open Channels.* Journal of Hydraulic Engineering, 2004. **130**(10): p. 1013-1024.
14. Wu, W.M. and Wang, S.S.Y., *One-dimensional explicit finite-volume model for sediment transport with transient flows over movable beds.* Journal of Hydraulic Research, 2008. **46**(1): p. 87-98.
15. Zhang, S. and Duan, J.G., *1D finite volume model of unsteady flow over mobile bed.* Journal of Hydrology, 2011. **405**(1–2): p. 57-68.
16. Benkhaldoun, F., Sahmim, S., and Sea ïd, M., *A two-dimensional finite volume morphodynamic model on unstructured triangular grids.* International Journal for Numerical Methods in Fluids, 2010. **63**(11): p. 1296-1327.
17. Fang, H., Liu, B., and Huang, B., *Diagonal Cartesian Method for the Numerical Simulation of Flow and Suspended Sediment Transport over Complex Boundaries.* Journal of Hydraulic Engineering, 2006. **132**(11): p. 1195-1205.
18. Castro Dı´az, M.J., et al., *Two-dimensional sediment transport models in shallow water equations. A second order finite volume approach on unstructured meshes.* Computer Methods in Applied Mechanics and Engineering, 2009. **198**(33–36): p. 2520-2538.
19. Chen, X., *A three-dimensional hydrodynamic model for shallow waters using unstructured Cartesian grids.* International Journal for Numerical Methods in Fluids, 2011. **66**(7): p. 885-905.
20. Rueda, F. and Schladow, S., *Quantitative Comparison of Models for Barotropic Response of Homogeneous Basins.* Journal of Hydraulic Engineering, 2002. **128**(2): p. 201-213.
21. Casulli, V. and Cheng, R.T., *Semi-implicit finite difference methods for three-dimensional shallow water flow.* International Journal for Numerical Methods in Fluids, 1992. **15**(6): p. 629-648.
22. Casulli, V. and Cattani, E., *Stability, accuracy and efficiency of a semi-implicit method for three-dimensional shallow water flow.* Computers & Mathematics with Applications, 1994. **27**(4): p. 99-112.
23. Lu, C.N. and Li, G., *Simulations of Shallow Water Equations by Finite Difference WENO Schemes with Multilevel Time Discretization.* Numerical Mathematics-Theory Methods and Applications, 2011. **4**(4): p. 505-524.

24. Stelling, G. and Zijlema, M., *An accurate and efficient finite-difference algorithm for non-hydrostatic free-surface flow with application to wave propagation.* International Journal for Numerical Methods in Fluids, 2003. **43**(1): p. 1-23.
25. Sheu, T.W.H. and Fang, C.C., *High resolution finite-element analysis of shallow water equations in two dimensions.* Computer Methods in Applied Mechanics and Engineering, 2001. **190**(20-21): p. 2581-2601.
26. Dawson, C. and Proft, J., *Coupled discontinuous and continuous Galerkin finite element methods for the depth-integrated shallow water equations.* Computer Methods in Applied Mechanics and Engineering, 2004. **193**(3–5): p. 289-318.
27. Eric Jones, J. and Davies, A.M., *Application of a finite element model (TELEMAC) to computing the wind induced response of the Irish Sea.* Continental Shelf Research, 2006. **26**(12–13): p. 1519-1541.
28. Comblen, R., et al., *A finite element method for solving the shallow water equations on the sphere.* Ocean Modelling, 2009. **28**(1–3): p. 12-23.
29. Liang, S.J., Tang, J.H., and Wu, M.S., *Solution of shallow-water equations using least-squares finite-element method.* Acta Mechanica Sinica, 2008. **24**(5): p. 523-532.
30. Daoud, A.H., Rakha, K.A., and Abul-azm, A.G., *A two-dimensional finite volume hydrodynamic model for coastal areas: Model development and validation.* Ocean Engineering, 2008. **35**(1): p. 150-164.
31. Alcrudo, F. and Garcia-Navarro, P., *A high-resolution Godunov-type scheme in finite volumes for the 2D shallow-water equations.* International Journal for Numerical Methods in Fluids, 1993. **16**(6): p. 489-505.
32. Zhao, D., et al., *Finite-Volume Two-Dimensional Unsteady-Flow Model for River Basins.* Journal of Hydraulic Engineering, 1994. **120**(7): p. 863-883.
33. Anastasiou, K. and Chan, C.T., *Solution of the 2D shallow water equations using the finite volume method on unstructured triangular meshes.* International Journal for Numerical Methods in Fluids, 1997. **24**(11): p. 1225-1245.

34. Hu, K., Mingham, C.G., and Causon, D.M., *A bore-capturing finite volume method for open-channel flows.* International Journal for Numerical Methods in Fluids, 1998. **28**(8): p. 1241-1261.
35. Mingham, C.G. and Causon, D.M., *High-Resolution Finite-Volume Method for Shallow Water Flows.* Journal of Hydraulic Engineering, 1998. **124**(6): p. 605-614.
36. Brocchini, M., et al., *An efficient solver for nearshore flows based on the WAF method.* Coastal Engineering, 2001. **43**(2): p. 105-129.
37. Hubbard, M.E. and Dodd, N., *A 2D numerical model of wave run-up and overtopping.* Coastal Engineering, 2002. **47**(1): p. 1-26.
38. Wei, Y., Mao, X., and Cheung, K., *Well-Balanced Finite-Volume Model for Long-Wave Runup.* Journal of Waterway, Port, Coastal, and Ocean Engineering, 2006. **132**(2): p. 114-124.
39. Demirdžić, I. and Perić, M., *Finite volume method for prediction of fluid flow in arbitrarily shaped domains with moving boundaries.* International Journal for Numerical Methods in Fluids, 1990. **10**(7): p. 771-790.
40. Olsen, N.R.B. and Stokseth, S., *Three-dimensional numerical modelling of water flow in a river with large bed roughness.* Journal of Hydraulic Research, 1995. **33**(4): p. 571-581.
41. Stansby, P.K., *Semi-implicit finite volume shallow-water flow and solute transport solver with k–ε turbulence model.* International Journal for Numerical Methods in Fluids, 1997. **25**(3): p. 285-313.
42. Chippada, S., et al., *A Godunov-type finite volume method for the system of Shallow water equations.* Computer Methods in Applied Mechanics and Engineering, 1998. **151**(1–2): p. 105-129.
43. Cobbin, A.M., et al., *An adaptive-grid solver with improved free-surface boundary conditions*. Hydroinformatics '98, Vols 1 and 2, ed. V. Babovic and L.C. Larsen1998, Leiden: A a Balkema Publishers. 55-60.
44. Chen, S. and Doolen, G.D., *Lattice Boltzmann method for fluid flows.* Annual Review of Fluid Mechanics, 1998. **30**: p. 329-364.
45. Aidun, C.K. and Clausen, J.R., *Lattice-Boltzmann Method for Complex Flows*, in *Annual Review of Fluid Mechanics*2010, Annual Reviews: Palo Alto. p. 439-472.

46. Zhang, X., et al., *A lattice BGK model for advection and anisotropic dispersion equation.* Advances in Water Resources, 2002. **25**(1): p. 1-8.

47. Zhang, Y., Qin, R., and Emerson, D.R., *Lattice Boltzmann simulation of rarefied gas flows in microchannels.* Physical Review E, 2005. **71**(4): p. 047702.

48. Zhang, Y.H., et al., *Modelling thermal flow in the transition regime using a lattice Boltzmann approach.* Epl, 2007. **77**(3).

49. Meng, J. and Zhang, Y., *Gauss-Hermite quadratures and accuracy of lattice Boltzmann models for nonequilibrium gas flows.* Physical Review E, 2011. **83**(3): p. 036704.

50. Meng, J., Zhang, Y., and Shan, X., *Multiscale lattice Boltzmann approach to modeling gas flows.* Physical Review E, 2011. **83**(4): p. 046701.

51. Succi, S., *The lattice Boltzmann equation for fluid dynamics and beyond* Numerical Mathematics and Scientific Computation2001, Oxford University Press

52. Wolf-Gladrow, D., *Lattice Gas Cellular Automata and Lattice Boltzmann Models, Lectures Notes in Mathematics*. 1st Edition ed2000, Berlin Heidelberg, New York: Springer Verlag.

53. Salmon, R., *The lattice Boltzmann method as a basis for ocean circulation modeling.* Journal of Marine Research, 1999. **57**(3): p. 503-535.

54. Dellar, P.J., *Nonhydrodynamic modes and a priori construction of shallow water lattice Boltzmann equations.* Physical Review E, 2002. **65**(3): p. 036309.

55. Li, Y. and Huang, P., *A coupled lattice Boltzmann model for advection and anisotropic dispersion problem in shallow water.* Advances in Water Resources, 2008. **31**(12): p. 1719-1730.

56. Liu, H., Zhou, G.J., and Burrows, R., *Lattice Boltzmann model for shallow water flows in curved and meandering channels.* International Journal of Computational Fluid Dynamics, 2009. **23**(3): p. 209-220.

57. Liu, H., Zhou, J.G., and Burrows, R., *Numerical modeling of turbulent compound channel flow using the lattice Boltzmann method.* International Journal for Numerical Methods in Fluids, 2009. **59**(7): p. 753-765.

58. Liu, H., Zhou J.G., and Burrows, R., *Lattice Boltzmann simulations of the transient shallow water flows.* Advances in Water Resources, 2010. **33**(4): p. 387-396.

59. Peng, Y., Zhou, J., and Burrows, R., *Modeling Free-Surface Flow in Rectangular Shallow Basins by Using Lattice Boltzmann Method.* Journal of Hydraulic Engineering, 2011. **137**(12): p. 1680-1685.
60. Peng, Y., Zhou, J.G., and Burrows, R., *Modelling solute transport in shallow water with the lattice Boltzmann method.* Computers & Fluids, 2011. **50**(1): p. 181-188.
61. Liu, H., Zhou, J.G., and Burrows, R., *Multi-block lattice Boltzmann simulations of subcritical flow in open channel junctions.* Computers & Fluids, 2009. **38**(6): p. 1108-1117.
62. Tubbs, K.R. and Tsai, F.T.C., *Multilayer shallow water flow using lattice Boltzmann method with high performance computing.* Advances in Water Resources, 2009. **32**(12): p. 1767-1776.
63. Hardy, J., Pazzis, O. de, and Pomeau, Y., *Molecular dynamics of a classical lattice gas: Transport properties and time correlation functions.* Physical Review A, 1976. **13**(5): p. 1949-1961.
64. Wolf-Gladrow, D.A., *Lattice-Gas Cellular Automata and Lattice Boltzmann Models: An Introduction*2000: Springer.
65. Frisch, U., Hasslacher, B., and Pomeau, Y., *Lattice-Gas Automata for the Navier-Stokes Equation.* Physical Review Letters, 1986. **56**(14): p. 1505-1508.
66. Frisch, U., et al., *Lattice gas hydrodynamics in two and three dimensions.* Complex Syst., 1987. **1**: p. 649-707.
67. McNamara, G.R. and Zanetti, G., *Use of the Boltzmann Equation to Simulate Lattice-Gas Automata.* Physical Review Letters, 1988. **61**(20): p. 2332-2335.
68. Higuera, F.J. and Jimenez, J., *Boltzmann approach to lattice gas simulations.* Europhysics Letters, 1989. **9**(7): p. 663-668.
69. Bhatnagar, P.L., Gross, E.P., and Krook, M., *A Model for Collision Processes in Gases. I. Small Amplitude Processes in Charged and Neutral One-Component Systems.* Physical Review, 1954. **94**(3): p. 511-525.
70. Qian, Y.H., *Lattice Gas and Lattice Kinetic Theory Applied to the Navier-Stokes Equation*, 1990, Ecole Normale Superieure and University of Paris 6.
71. Chen, S., et al., *Lattice Boltzmann model for simulation of magnetohydrodynamics.* Physical Review Letters, 1991. **67**(27): p. 3776-3779.

72. Ansumali, S. and Karlin, I.V., *Stabilization of the lattice Boltzmann method by the H theorem: A numerical test.* Physical Review E, 2000. **62**(6): p. 7999-8003.

73. Ansumali, S. and Karlin, I. V., *Kinetic boundary conditions in the lattice Boltzmann method.* Physical Review E, 2002. **66**(2): p. 026311.

74. Ansumali, S., I.V. Karlin, and H.C. Ottinger, *Minimal entropic kinetic models for hydrodynamics.* Europhysics Letters, 2003. **63**(6): p. 798-804.

75. Tsallis, C., *Possible generalization of Boltzmann-Gibbs statistics.* Journal of Statistical Physics, 1988. **52**(1-2): p. 479-487.

76. Gell-Mann M, T.C., eds. , *Nonextensive Entropy*2004, Oxford: Oxford Univ. Press.

77. Keating, B., et al., *Entropic lattice Boltzmann representations required to recover Navier-Stokes flows.* Physical Review E, 2007. **75**(3): p. 036712.

78. Karlin, I.V., Ferrante, A., and Ottinger, H.C., *Perfect entropy functions of the Lattice Boltzmann method.* Europhysics Letters, 1999. **47**(2): p. 182-188.

79. Ansumali, S., et al., *Entropic lattice Boltzmann method for microflows.* Physica a-Statistical Mechanics and Its Applications, 2006. **359**: p. 289-305.

80. Chikatamarla, S.S. and Karlin, I.V., *Entropy and Galilean Invariance of Lattice Boltzmann Theories.* Physical Review Letters, 2006. **97**(19): p. 190601.

81. Luo, L.-S., et al., *Numerics of the lattice Boltzmann method: Effects of collision models on the lattice Boltzmann simulations.* Physical Review E, 2011. **83**(5): p. 056710.

82. Ginzburg, I., *Equilibrium-type and link-type lattice Boltzmann models for generic advection and anisotropic-dispersion equation.* Advances in Water Resources, 2005. **28**(11): p. 1171-1195.

83. d’Humieres, D., *Generalized lattice Boltzmann equations. In Rarefied gas dynamics: theory and simulations (ed. B. D. Shizgal & D. P.Weaver),* in *Prog. Aeronaut. Astronaut.* 1992 p. 450-458.

84. d'Humieres, D., et al., *Multiple-relaxation-time lattice Boltzmann models in three dimensions.* Philosophical Transactions of the Royal Society of London Series a-Mathematical Physical and Engineering Sciences, 2002. **360**(1792): p. 437-451.

85. Lallemand, P. and Luo, L.-S., *Theory of the lattice Boltzmann method: Dispersion, dissipation, isotropy, Galilean invariance, and stability.* Physical Review E, 2000. **61**(6): p. 6546-6562.
86. Yu, D., Mei, R., and Shyy, W., *A multi-block lattice Boltzmann method for viscous fluid flows.* International Journal for Numerical Methods in Fluids, 2002. **39**(2): p. 99-120.
87. Zhou, J.G., *Rectangular lattice Boltzmann method.* Physical Review E, 2010. **81**(2): p. 026705.
88. Zhou, J.G., *MRT RECTANGULAR LATTICE BOLTZMANN METHOD.* International Journal of Modern Physics C, 2012. **23**(05): p. 1250040.
89. Bouzidi, M., et al., *Lattice Boltzmann equation on a two-dimensional rectangular grid.* Journal of Computational Physics, 2001. **172**(2): p. 704-717.
90. Filippova, O. and Hänel, D., *Grid Refinement for Lattice-BGK Models.* Journal of Computational Physics, 1998. **147**(1): p. 219-228.
91. Lin, C.-L. and Lai, Y.G., *Lattice Boltzmann method on composite grids.* Physical Review E, 2000. **62**(2): p. 2219-2225.
92. Kandhai, D., et al., *Finite-Difference Lattice-BGK methods on nested grids.* Computer Physics Communications, 2000. **129**(1–3): p. 100-109.
93. Liu, H., *Lattice Boltzmann simulations for complex shallow water flows*, 2009, University of Liverpool, PhD thesis.
94. Dupuis, A. and Chopard, B., *Theory and applications of an alternative lattice Boltzmann grid refinement algorithm.* Physical Review E, 2003. **67**(6): p. 066707.
95. Succi, S., *The Lattice Boltzmann Equation For Fluid Dynamics and Beyond*2001, Oxford: Oxford University Press.
96. Wilke, J., Pohl, T., Kowarschik, M. and Rude, U., *Cache Performance Optimizations for Parallel Lattice Boltzmann Codes*. in *Euro-Par 2003 Parallel Processing*. 2003.
97. Wellein, G., et al., *On the single processor performance of simple lattice Boltzmann kernels.* Computers & Fluids, 2006. **35**(8–9): p. 910-919.
98. Desplat, J.-C., Pagonabarraga, I., and Bladon, P., *LUDWIG: A parallel Lattice-Boltzmann code for complex fluids.* Computer Physics Communications, 2001. **134**(3): p. 273-290.

99. Li, W., Fan, Z., Wei, X. and Kaufman, A., *Flow Simulation with Complex Boundaries*, in *GPU Gems II: Programming Techiniques for High-Performance Graphics and General-Purpose Computaiton*2005, Addison-Wesley: M. Pharr. p. 747-764.

100. Zhao, Y., *Lattice Boltzmann based PDE solver on the GPU.* The Visual Computer, 2008. **24**(5): p. 323-333.

101. Tubbs, K.R. and Tsai, F.T.C., *GPU accelerated lattice Boltzmann model for shallow water flow and mass transport.* International Journal for Numerical Methods in Engineering, 2011. **86**(3): p. 316-334.

102. Zhe, F., et al. *GPU Cluster for High Performance Computing*. in *Supercomputing, 2004. Proceedings of the ACM/IEEE SC2004 Conference*. 2004.

103. Tubbs, K.R., *Lattice Boltzmann modelling for shallow water equations using high performance computing*, 2010, Louisiana state university.

104. Jin, K. and Auburn, U., *On the Lattice Boltzmann Method: Implementation and Applications*2008: Auburn University.

105. Lallemand, P. and Luo, L.S., *Lattice Boltzmann method for moving boundaries.* Journal of Computational Physics, 2003. **184**(2): p. 406-421.

106. Kao, P.H. and Yang, R.J., *An investigation into curved and moving boundary treatments in the lattice Boltzmann method.* Journal of Computational Physics, 2008. **227**(11): p. 5671-5690.

107. Bouzidi, M., Firdaouss, M., and Lallemand, P., *Momentum transfer of a Boltzmann-lattice fluid with boundaries.* Physics of Fluids, 2001. **13**(11): p. 3452-3459.

108. Stansby, P.K. and Zhou, J.G., *Shallow-water flow solver with non-hydrostatic pressure: 2D vertical plane problems.* International Journal for Numerical Methods in Fluids, 1998. **28**(3): p. 541-563.

109. A., F.R., *An introduction to nearly horizontal flows, In: Abbott, M.B., Price, W.A. (Eds.), Coastal, Estuarial and Harbour Engineers'Reference Book*1993, London: E & FN Spon Ltd. .

110. Sokolnikoff, I.S. and Redheffer, R.M., *Mathematics of physics and modern engineering*1966: McGraw-Hill.

111. Spivak, M., *Calculus*1967, New York, USA: W. A. Benjamin Inc. .

112. A., F.R., *An Introduction to Nearly-Horizontal Flows*, in *Coastal, Estuarial and Harbour Engineer's Reference Book*, E.M.B.A.a.W.A. Price, Editor 1993: Chapman & Hall, London, England. p. 27-36.
113. Kuipers, J., and Vreugdenhil, C. B. , *Calculation of Two-Dimensional Horizontal Flow*, in *Report S163, Part I*1973: Delft Hydraulic Laboratory, Delft, The Netherlands. p. 1-44.
114. McGuirk, J.J. and Rodi, W., *A depth-averaged mathematical model for the near field of side discharges into open-channel flow.* Journal of Fluid Mechanics, 1978. **86**(04): p. 761-781.
115. Wijbenga, V.a.J.H., *Computation of flow patterns in rivers.* J. Hydr. Eng. Div., ASCE, 1982. **108**(11): p. 1296-1310.
116. Borthwick and Akponasa, *Reservoir Flow Prediction by Contravariant Shallow Water Equations.* Journal of Hydraulic Engineering, 1997. **123**(5): p. 432-439.
117. Nalluri, C. and Marriott, M., *Civil Engineering Hydraulics*2009: John Wiley & Sons.
118. McDonough, J.M., *Introductory Lectures on Turbulence, Departments of Mechanical Engineering and Mathematics*2004: University of Kentucky.
119. Smagorinsky, J., *General circulation experiments with the primitive equations.* Monthly Weather Review, 1963. **91**(3): p. 99-164.
120. He, X. and Luo, L.S., *A priori derivation of the lattice Boltzmann equation.* Physical Review E, 1997. **55**(6): p. R6333-R6336.
121. Abe, T., *Derivation of the Lattice Boltzmann Method by Means of the Discrete Ordinate Method for the Boltzmann Equation.* Journal of Computational Physics, 1997. **131**(1): p. 241-246.
122. Koelman, J.M.V.A., *A Simple Lattice Boltzmann Scheme for Navier-Stokes Fluid Flow* Europhys. Lett., 1991. **15**.
123. Noble, D.R., et al., *A consistent hydrodynamic boundary-condition for the lattice Boltznmann method.* Physics of Fluids, 1995. **7**(1): p. 203-209.
124. Skordos, P.A., *Initial and boundary conditions for the lattice Boltzmann method.* Physical Review E, 1993. **48**(6): p. 4823-4842.
125. Zhou, J.G., *An elastic-collision scheme for lattice Boltzmann methods.* International Journal of Modern Physics C (IJMPC), 2001. **12**(03): p. 387-401.

126. Rothman, D.H.a.S.Z., *Lattice Gas Cellular Automata*1997, London Cambridge University Press.

127. Chen, H., Chen, S., and Matthaeus, W.H., *Recovery of the Navier-Stokes equations using a lattice-gas Boltzmann method.* Physical Review A, 1992. **45**(8): p. R5339-R5342.

128. Guangwu, Y., *A Lattice Boltzmann Equation for Waves.* Journal of Computational Physics, 2000. **161**(1): p. 61-69.

129. Zhou, J.G., *A lattice Boltzmann model for the shallow water equations.* Computer Methods in Applied Mechanics and Engineering, 2002. **191**(32): p. 3527-3539.

130. Sterling, J.D. and Chen, S., *Stability Analysis of Lattice Boltzmann Methods.* Journal of Computational Physics, 1996. **123**(1): p. 196-206.

131. Martys, N.S., Shan, X., and Chen, H., *Evaluation of the external force term in the discrete Boltzmann equation.* Physical Review E, 1998. **58**(5): p. 6855-6857.

132. Buick, J.M. and Greated, C.A., *Gravity in a lattice Boltzmann model.* Physical Review E, 2000. **61**(5): p. 5307-5320.

133. Guo, Z., Zheng, C., and Shi, B., *Discrete lattice effects on the forcing term in the lattice Boltzmann method.* Physical Review E, 2002. **65**(4): p. 046308.

134. Zhou, J.G., *Enhancement of the LABSWE for shallow water flows.* Journal of Computational Physics, 2011. **230**(2): p. 394-401.

135. Hou, S. , Sterling, J., Chen, S., and Doolen, G. D., *A lattice Boltzmann subgrid model for high Reynolds number flows.* Fields Inst. Commun, 1996. **6**.

136. Zhou, J.G., *A lattice Boltzmann method for solute transport.* International Journal for Numerical Methods in Fluids, 2009. **61**(8): p. 848-863.

137. Klar, A., Seaid, M., and Thommes, G., *Lattice Boltzmann simulation of depth-averaged models in flow hydraulics.* International Journal of Computational Fluid Dynamics, 2008. **22**(7): p. 507-522.

138. Zhang, X., et al., *On boundary conditions in the lattice Boltzmann model for advection and anisotropic dispersion equation.* Advances in Water Resources, 2002. **25**(6): p. 601-609.

139. Zou, Q.S. and He, X.Y., *On pressure and velocity boundary conditions for the lattice Boltzmann BGK model.* Physics of Fluids, 1997. **9**(6): p. 1591-1598.

140. Guo, Z.L., Zheng, C.G., and Shi, B.C., *Non-equilibrium extrapolation method for velocity and pressure boundary conditions in the lattice Boltzmann method.* Chinese Physics, 2002. **11**(4): p. 366-374.

141. Chen, S.Y., Martinez, D., and Mei, R.W., *On boundary conditions in lattice Boltzmann methods.* Physics of Fluids, 1996. **8**(9): p. 2527-2536.

142. Ginzburg, I. and d'Humières, D., *Multireflection boundary conditions for lattice Boltzmann models.* Physical Review E, 2003. **68**(6): p. 066614.

143. Junk, M. and Yang, Z., *One-point boundary condition for the lattice Boltzmann method.* Physical Review E, 2005. **72**(6): p. 066701.

144. Inamuro, T., Yoshino, M., and Ogino, F., *A non-slip boundary condition for lattice Boltzmann simulations.* Physics of Fluids, 1995. **7**(12): p. 2928-2930.

145. Gallivan, M.A., et al., *An evaluation of the bounce-back boundary condition for lattice Boltzmann simulations.* International Journal for Numerical Methods in Fluids, 1997. **25**(3): p. 249-263.

146. Graber, S.D., *Asymmetric flow in symmetric expansions.* Journal of the Hydraulics Division-Asce, 1982. **108**(10): p. 1082-1101.

147. Mullin, T., Shipton, S., and Tavener, S.J., *Flow in a symmetric channel with an expanded section.* Fluid Dynamics Research, 2003. **33**(5-6): p. 433-452.

148. Dewals, B.J., et al., *Experimental and numerical analysis of flow instabilities in rectangular shallow basins.* Environmental Fluid Mechanics, 2008. **8**(1): p. 31-54.

149. Babarutsi, S., Ganoulis, J., and Chu, V.H., *Experimental investigation of shallow recirculating-flows.* Journal of Hydraulic Engineering-Asce, 1989. **115**(7): p. 906-924.

150. Babarutsi, S., Nassiri, M., and Chu, V.H., *Computation of shallow recirculating flow dominated by friction.* Journal of Hydraulic Engineering-Asce, 1996. **122**(7): p. 367-372.

151. Oca, J., Masalo, I., and Reig, L., *Comparative analysis of flow patterns in aquaculture rectangular tanks with different water inlet characteristics.* Aquacultural Engineering, 2004. **31**(3-4): p. 221-236.

152. Dufresne, M., et al., *Classification of flow patterns in rectangular shallow reservoirs.* Journal of Hydraulic Research, 2010. **48**(2): p. 197-204.

153. Dufresne, M., et al., *Experimental investigation of flow pattern and sediment deposition in rectangular shallow reservoirs.* International Journal of Sediment Research, 2010. **25**(3): p. 258-270.

154. Dufresne, M., et al., *Numerical investigation of flow patterns in rectangular shallow reserviors.* Engineering Applications of Computational Fluid Mechanics, 2011. **5**(2): p. 247-258.

155. Chen, D.Y. and Jirka, G.H., *Absolute and convective instabilities of plane turbulent wakes in a shallow water layer.* Journal of Fluid Mechanics, 1997. **338**: p. 157-172.

156. Zhou, J.G., et al., *Numerical solutions of the shallow water equations with discontinuous bed topography.* International Journal for Numerical Methods in Fluids, 2002. **38**(8): p. 769-788.

157. Zhou, J.G., et al., *The surface gradient method for the treatment of source terms in the shallow-water equations.* Journal of Computational Physics, 2001. **168**(1): p. 1-25.

158. Erduran K.S., Kutija, V., and Hewett, C.J.M., *Finite volume solution for flow in a channel with a step on its bottom*, in *Fifth International Conference on Hydroinformatics*2002: Cardiff, UK.

159. Crnjaric-Zic, N., Vukovic, S., and Sopta, L., *Balanced finite volume WENO and central WENO schemes for the shallow water and the open-channel flow equations.* Journal of Computational Physics, 2004. **200**(2): p. 512-548.

160. Bernetti, R., Titarev, V.A., and Toro, E.F., *Exact solution of the Riemann problem for the shallow water equations with discontinuous bottom geometry.* Journal of Computational Physics, 2008. **227**(6): p. 3212-3243.

161. Rosatti, G. and Begnudelli, L., *The Riemann Problem for the one-dimensional, free-surface Shallow Water Equations with a bed step: Theoretical analysis and numerical simulations.* Journal of Computational Physics, 2010. **229**(3): p. 760-787.

162. Kesserwani, G. and Liang, Q.H., *A conservative high-order discontinuous Galerkin method for the shallow water equations with arbitrary topography.* International Journal for Numerical Methods in Engineering, 2011. **86**(1): p. 47-69.

163. Cozzolino, L., et al., *Numerical solution of the discontinuous-bottom Shallow-water Equations with hydrostatic pressure distribution at the step.* Advances in Water Resources, 2011. **34**(11): p. 1413-1426.

164. Goutal N., a.M.F.e., *Proceedings of the 2nd Workshop on Dam-break Wave Simulation. HE-43/97/016/B.*, 1997: Département Laboratoire National d'Hydraulique, Groupe Hydraulique Fluviable, Electricité de France, France.

165. Bermudez, A. and E. Vazquez, *Upwind methods for hyperbolic conservation-laws with source terms.* Computers & Fluids, 1994. **23**(8): p. 1049-1071.

166. Shokin, Y.I., et al., *Modelling surface waves generated by a moving landslide with allowance for vertical flow structure.* Russian Journal of Numerical Analysis and Mathematical Modelling, 2007. **22**(1): p. 63-85.

167. Tinti, S., Bortolucci, E., and Chiavettieri, C., *Tsunami excitation by submarine slides in shallow-water approximation.* Pure and Applied Geophysics, 2001. **158**(4): p. 759-797.

168. Causon, D.M., Ingram, D.M., and Mingham, C.G., *A Cartesian cut cell method for shallow water flows with moving boundaries.* Advances in Water Resources, 2001. **24**(8): p. 899-911.

169. Mei, R.W., Luo, L.S., and Shyy, W., *An accurate curved boundary treatment in the lattice Boltzmann method.* Journal of Computational Physics, 1999. **155**(2): p. 307-330.

170. Guo, Z.L., Zheng, C.G., and Shi, B.C., *An extrapolation method for boundary conditions in lattice Boltzmann method.* Physics of Fluids, 2002. **14**(6): p. 2007-2010.

171. Verschaeve, J.C.G. and Muller, B., *A curved no-slip boundary condition for the lattice Boltzmann method.* Journal of Computational Physics, 2010. **229**(19): p. 6781-6803.

172. Harbitz, C.B., Pedersen, G., and Gjevik, B., *Numerical simulations of large water-waves due to landslides.* Journal of Hydraulic Engineering-Asce, 1993. **119**(12): p. 1325-1342.

173. Tinti, S., Bortolucci, E., and Armigliato, A., *Numerical simulation of the landslide-induced tsunami of 1988 on Vulcano Island, Italy.* Bulletin of Volcanology, 1999. **61**(1-2): p. 121-137.

174. Delis, A.I. and Kazolea, M., *Finite volume simulation of waves formed by sliding masses.* International Journal for Numerical Methods in Biomedical Engineering, 2011. **27**(5): p. 732-757.

175. Kuo, C.Y., et al., *The landslide stage of the Hsiaolin catastrophe: Simulation and validation.* Journal of Geophysical Research-Earth Surface, 2011. **116**.

176. Yu, D.Z., et al., *Viscous flow computations with the method of lattice Boltzmann equation.* Progress in Aerospace Sciences, 2003. **39**(5): p. 329-367.

177. Benkhaldoun, F., Elmahi, I., and Seaïd, M., *Well-balanced finite volume schemes for pollutant transport by shallow water equations on unstructured meshes.* Journal of computational physics., 2007. **226**(1): p. 180-203.

178. Cai, L., et al., *Computations of transport of pollutant in shallow water.* Applied Mathematical Modelling, 2007. **31**(3): p. 490-498.

179. Mikhail, R., Chu, V.H., Savage, S.B. *The reattachment of a two-dimensional turbulent jet in a confined cross flow*. in *Proceedings of the 16th IAHR Congress.* . 1975. Sao Paulo, Brazil.

180. Wang, X. and Cheng, L., *Three-dimensional simulation of a side discharge into a cross channel flow*. Computers & Fluids, 2000. **29**(4): p. 415-433.

181. Kim, D.G. and Cho, H.Y., *Modeling the buoyant flow of heated water discharged from surface and submerged side outfalls in shallow and deep water with a cross flow.* Environmental Fluid Mechanics, 2006. **6**(6): p. 501-518.

182. Yin, J.F., Falconer, R.A., and Chen, Y.P., *Velocity and solute concentration distributions in model harbours.* Proceedings of the Institution of Civil Engineers-Maritime Engineering, 2004. **157**(1): p. 47-56.

183. Nassiri, M. and Babarutsi, S., *Computation of dye concentration in shallow recirculating flow.* Journal of Hydraulic Engineering-Asce, 1997. **123**(9): p. 793-805.

184. Nassiri, M., *Two-dimensional Simulation Models of Shallow Recirculating Flows*, 1999, McGill University.

185. Babarutsi, S. and Chu, V.H., *Dye-concentration distribution in shallow recirculating-flows.* Journal of Hydraulic Engineering-Asce, 1991. **117**(5): p. 643-659.

186. Johnson, H.K. and J.A. Zyserman, *Controlling spatial oscillations in bed level update schemes.* Coastal Engineering, 2002. **46**(2): p. 109-126.

187. Callaghan, D.P., et al., *Numerical solutions of the sediment conservation law; a review and improved formulation for coastal morphological modelling.* Coastal Engineering, 2006. **53**(7): p. 557-571.

188. Long, W., Kirby, J.T., and Shao, Z.Y., *A numerical scheme for morphological bed level calculations.* Coastal Engineering, 2008. **55**(2): p. 167-180.

189. Jiang, G.S. and Shu, C.W., *Efficient implementation of weighted ENO schemes.* Journal of Computational Physics, 1996. **126**(1): p. 202-228.

190. Jiang, G.S. and Wu, C.C., *A high-order WENO finite difference scheme for the equations of ideal magnetohydrodynamics.* Journal of Computational Physics, 1999. **150**(2): p. 561-594.

191. Hudson, J., *Numerical techniques for morphodynamic modelling*, 2001 University of Reading.

192. Huang, J., Borthwich, A. G. L., and Soulsby, R. l., *Adaptive Quadtree simulation of sediment transport* Proceedings of Institution of Civil Engineers: Journal of Engineering and Computational Mechanics, 2010. **163 (EM2)**.

193. Lin, Q.H., *Numerical simulation of sediment transport and morphological evolution*, 2009, National university of Singapore.

194. Meyer-Peter, E.a.M., R. *Formulas for bed-load transport*. in *2nd Congress of the Int. Association for Hydraulic Structures Research*. 1948. Stockholm, Sweden.

195. Yalin, M.S., *Mechanics of Sediment Transport*1972, Pergamon, New York.

196. Hudson, J. and Sweby, P.K., *A high-resolution scheme for the equations governing 2D bed-load sediment transport.* International Journal for Numerical Methods in Fluids, 2005. **47**(10-11): p. 1085-1091.

197. van Thang, P., et al., *Study of the 1D lattice Boltzmann shallow water equation and its coupling to build a canal network.* Journal of Computational Physics, 2010. **229**(19): p. 7373-7400.